

# **Solar variability: A new proxy and models of solar irradiance variations**

Von der Fakultät für Elektrotechnik, Informationstechnik, Physik  
der Technischen Universität Carolo-Wilhelmina

zu Braunschweig

zur Erlangung des Grades einer

Doktorin der Naturwissenschaften

(Dr.rer.nat.)

genehmigte

Dissertation

von Maria Dasi Espuig

aus Valencia, Spanien

## **Bibliografische Information der Deutschen Nationalbibliothek**

Die Deutsche Nationalbibliothek verzeichnet diese Publikation in der Deutschen Nationalbibliografie; detaillierte bibliografische Daten sind im Internet über <http://dnb.d-nb.de> abrufbar.

1. Referentin oder Referent: Prof. Dr. Karl-Heinz Glassmeier

2. Referentin oder Referent: Prof. Dr. Sami K. Solanki

eingereicht am: 15. Juli 2011

mündliche Prüfung (Disputation) am: 26. September 2011

ISBN 978-3-942171-62-5

uni-edition GmbH

<http://www.uni-edition.de>

© Maria Dasi Espuig



This work is distributed under a  
Creative Commons Attribution 3.0 License

Printed in Germany

# Contents

<b>Summary</b>	<b>5</b>
<b>1 Introduction</b>	<b>7</b>
1.1 Solar variability and its impact on Earth	7
1.2 The Sun's magnetic cycle	11
1.2.1 Photospheric magnetic features	11
1.2.2 Large-scale structure	13
1.2.3 Prediction methods	15
1.2.3.1 Statistical methods	16
1.2.3.2 Dynamo model based predictors	17
1.3 Total solar irradiance	20
1.3.1 Measurements	20
1.3.2 Variations and their origin	22
1.3.3 SATIRE models	24
1.3.4 Secular trend	27
1.4 Outline of the thesis	29
<b>2 Sunspot group tilt angles and the strength of the solar cycle</b>	<b>31</b>
2.1 Abstract	31
2.2 Introduction	32
2.3 Data and tests	33
2.3.1 Data	33
2.3.2 Data evaluation	33
2.3.3 Joy's law	37
2.4 Results	38
2.4.1 Average value of tilt angles	38
2.4.2 Cycle parameter definitions	39
2.4.3 Relationships within the same cycle	40
2.4.4 Relationships with the following cycle	42
2.5 Discussion	46
2.6 Conclusions	50
<b>3 Solar irradiance reconstructions from a Surface Flux Transport Model</b>	<b>51</b>
3.1 Abstract	51
3.2 Introduction	51
3.3 The Surface Flux Transport Model	53

3.3.1	The induction equation . . . . .	53
3.3.2	The source function: including the tilt angle of sunspot groups . . .	54
3.4	SATIRE: method . . . . .	56
3.5	Results . . . . .	59
3.6	Conclusions and discussion . . . . .	64
<b>4</b>	<b>Solar irradiance reconstructions: including ephemeral regions</b>	<b>67</b>
4.1	Abstract . . . . .	67
4.2	Introduction . . . . .	67
4.3	Modeling the ephemeral region flux . . . . .	68
4.4	Results and discussion . . . . .	72
4.4.1	Fixing the free parameters: $X$ and $t_x$ . . . . .	72
4.4.2	Fixing the free parameters: $B_f$ and $B_{er}$ . . . . .	73
4.4.3	TSI reconstruction since 1878 . . . . .	77
4.4.4	Relations with total and open flux . . . . .	84
4.5	Conclusions . . . . .	86
<b>5</b>	<b>Conclusions and outlook</b>	<b>91</b>
<b>A</b>	<b>Determining the cycle-to-cycle variations in the presence of a large intrinsic scatter</b>	<b>99</b>
	<b>Bibliography</b>	<b>101</b>
	<b>Publications</b>	<b>115</b>
	<b>Acknowledgements</b>	<b>117</b>
	<b>Lebenslauf</b>	<b>119</b>

# Summary

Solar activity has been observed to vary at all measured time scales, of which the most prominent feature is the 11-year solar cycle. The latter was first noticed in the sunspot number, but is actually shown by almost all solar variables. Variations of the solar activity are of high importance for the Earth's climate and thus the prediction of past and future solar activity is key for climate studies. In this dissertation both aspects are studied, where a new proxy for the prediction of future solar activity and a method to reconstruct irradiance in the past are presented.

A record of sunspot group areas, positions, and tilt angles covering almost 7 solar cycles has permitted us to analyse cycle-to-cycle variations of the sunspot group tilt angles and to compare these with global parameters of the solar cycle, namely the length, strength, and amplitude. The cycle averaged sunspot group tilt angles are found to vary from one cycle to the next. More important are the correlations found between the weighted cycle averaged tilt angles and the strength of the same and the next cycle. The positive correlation between a tilt angle expression based on the Babcock-Leighton idea for the solar dynamo and the strength of the next cycle makes possible a prediction of the amplitude of the upcoming sunspot cycle around 10 years in advance. This analysis has shown the potential of the sunspot group tilt angles to forecast the amplitude of upcoming solar cycles.

Another important measure of solar activity is the total solar irradiance. Solar irradiance is the total energy in the Sun's radiation received per unit area and time at the top of the Earth's atmosphere and is thus directly related to the Earth's climate. It has only been measured for the last 33 years. Models of the total solar irradiance assuming that its variations are due to changes in the solar surface magnetic fields have been remarkably successful in reproducing the observed changes. For comparisons with climate records, longer term reconstructions are, however, needed. Therefore we have reconstructed total solar irradiance back to 1878. Our total solar irradiance reconstructions thus cover cycles 12–23 (years 1878 to 2010), i.e. the period for which a high-quality sunspot area and position record is available. To describe the evolution of the solar surface magnetic fields we use a surface flux transport model which calculates daily synthetic full-disc magnetograms at the solar surface starting from sunspot positions and areas. These synthetic data are then used as input data in the SATIRE-S (Spectral And Total Irradiance RE-constructions for the Satellite era) model to reconstruct the total solar irradiance. The irradiance model is further improved by including the magnetic flux from ephemeral regions. Ephemeral regions are small bipolar regions found all over the solar surface. They have been observed to follow a cyclic pattern similar to that seen in the sunspot number and area, but they appear 2 to 3 years before sunspot minimum, which leads to an overlap between subsequent ephemeral region cycles. This has been proposed to be the cause of

the secular change observed in the total photospheric magnetic flux. Since a continuous and homogeneous record of ephemeral regions is not available, we modelled their evolution assuming that their emergence rate is related to that of active regions but that their cycles are stretched compared to the corresponding sunspot cycles.

We compared the amplitude of the cycles and the long term behaviour of our total solar irradiance reconstructions with that of two previous works. The other two reconstructions were done following a similar method as is presented here. However, some of the differences between the models are reflected in the different irradiance reconstructions. Finally, we tested the global relationships between the total solar irradiance and the total surface magnetic flux and between the total solar irradiance and the open flux.

# 1 Introduction

## 1.1 Solar variability and its impact on Earth

Of all the stars in the Universe, the Sun occupies a vital position for us, as it is the closest star to our planet Earth. It has been long observed and studied. Already by the year 800 B.C. the Chinese had their eyes on the Sun, and have the first written record of an observed sunspot. However, it was not until the time of Galileo Galilei and Christoph Scheiner at the beginning of the 17th century when the first telescopic observations of sunspots began. With these observations also came the notion that the sunspots are actually features on the solar surface and a continuous record of the sunspot number exists since then. Later on in 1843, Schwabe published the first work arguing that the sunspots on the solar surface varied in number with a period of approximately 11 years. Nowadays, the modern space instrumentation has proved the Sun to vary on even shorter time scales down to minutes through phenomena such as flares, coronal mass ejections and other transient events, the 5 minute oscillations (p-modes), or the changing granulation patterns. On the other hand, other proxies like cosmogenic isotope concentrations have implied variations of solar activity on even longer time scales up to centuries and millennia.

Studying solar variability implies not only investigating its causes but also studying its effects on the Earth. *Space weather* deals with some of the events related to short term variations and their causes. The deepest visible layer of the Sun is called the photosphere. The chromosphere and the corona compose the higher layers of the solar atmosphere and extend outwards from the photosphere. The chromosphere and the corona appear in the observations as very dynamic and rapidly evolving environments and here the signatures of flares and coronal mass ejections are found. These events lash out energetic particles that can reach the Earth's magnetosphere and inner atmosphere and are the cause of beautiful phenomena such as auroras, but are also responsible for the damage of satellites and communication systems.

Variations on longer time scales are important for the Earth's climate. To study past long term variations, different proxies of solar activity are available spanning different time ranges. There are continuous and homogeneous space-based data for about the last half a century, yet the longest time series of direct measurements is found in ground-based data. In particular we have sunspot number records since 1610 (Eddy 1976, Hoyt and Schatten 1998) and sunspot areas since 1874 (Balmaceda et al. 2009). Other proxies of solar activity are the geomagnetic aa-index measured since 1868, 10.7 cm solar flux (disc integrated emission at the 10.7 cm wavelength) from 1946 onwards, Mg II core-to-

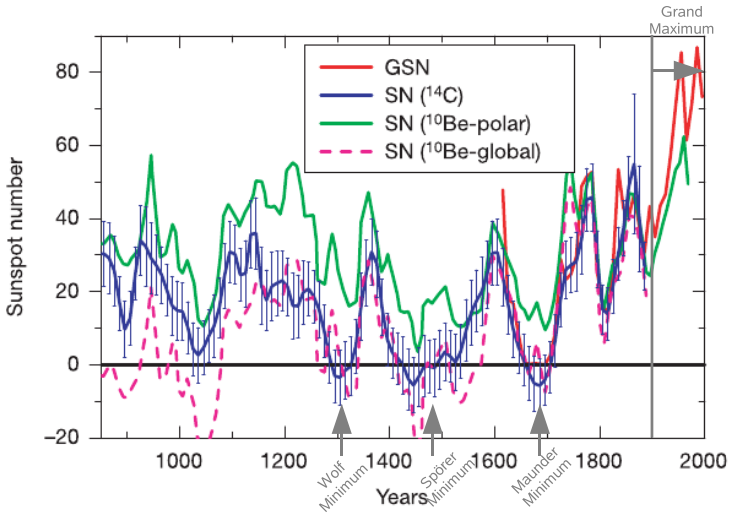


Figure 1.1: Reconstructed sunspot numbers from different cosmogenic isotopes as compared with the directly measured sunspot number. Reconstructions from  $^{14}\text{C}$  is the solid blue, from  $^{10}\text{Be}$  the solid green line and the dashed magenta line, and the blue solid line is the 10-year averaged sunspot group number since 1610. Plot taken from Solanki et al. (2004). The grey arrows and letters indicate the most recent grand minima and the current grand maximum.

wing ratio available since 1978 and Ca II K images since 1907, the total photospheric magnetic flux for which regular measurements exist since 1974, and the solar irradiance satellite measurements since 1978 (Lockwood et al. 1999, Donnelly et al. 1983, Viereck et al. 2004, Ermolli et al. 2010, Willson and Hudson 1991, Fröhlich 2006, Arge et al. 2002). All of these data show the well known 11 year solar cycle, with each cycle having a different amplitude and duration (see Sect. 1.2.2).

Further back in time, on millennium time scales, one has to rely on other indirect and less continuous data of solar activity, such as concentrations of cosmogenic isotopes produced by cosmic rays reaching the Earth's atmosphere. The isotopes used are  $^{14}\text{C}$  and  $^{10}\text{Be}$ , from tree rings and ice cores respectively (Stuiver and Braziunas 1989, Beer et al. 1990, Beer 2000, Usoskin 2008). Some of these records extend back to around 9500 B.C., this is, the whole Holocene period (Solanki et al. 2004, Usoskin 2008, Usoskin et al. 2009). Sunspot number records and cosmogenic isotope concentrations show periodic variations on time scales longer than the 11 year cycle. Some of which are the well known 22 year magnetic cycle (Hale and Nicholson 1925), the Gnevyshev-Ohl Effect, the Gleissberg cycle or an 80 to 90 year variation in the cycle amplitudes (Gleissberg 1939, Feynman and Fougere 1984, Peristykh and Damon 2003), and the 210-year Suess (also called de Vries) cycle (Stuiver and Braziunas 1989, Wagner et al. 2001), among others (for a review see Hathaway 2010, Petrovay 2010). Epochs of notably low and high solar

activity have also been reported from the mentioned data, apparently not showing a periodic behaviour (Usoskin et al. 2007, Usoskin 2008). The so-called grand minima, are extended periods of low solar activity when practically no sunspots are seen on the solar surface. Some examples of these are the Wolf (1280 – 1340), the Spörer (1409 – 1551) and the Maunder (1645 – 1715) minima. The grand maxima are the extended periods of high solar activity when the number of sunspots is exceptionally higher than the mean. Solanki et al. (2004) showed that during the last 70 years of the past century we lived in an unusually high level of activity, as observed in the sunspot number reconstructed from the cosmogenic isotopes  $^{14}\text{C}$  and  $^{10}\text{Be}$ . Figure 1.1 shows the reconstructed sunspot number by Solanki et al. (2004) where we have indicated the periods of unusually low and high activity in grey. The directly observed sunspot group number (red) is also seen to have suffered a rapid increase from 1900 to 1940 and has maintained such level since then.

The impact of solar activity on the Earth has been widely discussed as early as 1801 by Herschel, who found a correlation between the sunspot number and the price of wheat (Herschel 1801). Solar activity refers to active phenomena on the Sun, including active regions, sunspots, faculae, plages, prominences and flares. Herschel argued that during a sunspot maximum the presence of more sunspots would darken the Sun and reduce the radiative output, thus cooling the Earth. Now we know this argument is completely erroneous since solar irradiance increases during sunspot maximum due to the dominating presence of bright faculae (see Sect. 1.3.2). Although his reasoning was not correct, the Sun-Earth connection was made. A later paper by Eddy (1976) suggested that winter temperatures in western Europe were correlated with solar activity. During the period between 1500 and 1850 western Europe suffered from extremely cold winters and this period is referred to as the “Little Ice Age”, which partly coincides with the period of the Maunder Minimum (1645 – 1715). However, recent climate modeling has been able to explain the cooling during the Little Ice Age by the effect of volcanic eruptions (Jungclauss et al. 2010a,b).

Total solar irradiance (TSI) is the total energy received per unit area and time at the top of the Earth’s atmosphere, and is the dominant external energy source for the Earth’s atmosphere. Thus, changes in the solar radiative output clearly have the potential to affect climate. Climate models use the so called solar radiative forcing,  $\Delta F$ , directly related to the increase in TSI, given by Eq. (1.1)

$$\Delta F = \Delta \text{TSI}(1 - A)/4, \quad (1.1)$$

where  $A$  is the Earth’s albedo. Recent estimates of the TSI increase since the Maunder minimum span the range from  $\Delta \text{TSI}_{\text{mm}} \approx 0.2 - 6 \text{ W m}^{-2}$  depending on the model and the assumptions used (see Sect. 1.3.4), which translates into solar forcing as  $\Delta F_{\text{mm}} \approx 0.03 - 0.9 \text{ W m}^{-2}$ , if one takes the Earth’s albedo as  $A = 0.4$ . Numerous climate models have attempted to reproduce the increase in global surface temperature of the Earth since the beginning of the 20th century by combining the effects of both natural forcings (solar and volcanic) and anthropogenic forcings (e.g. greenhouse gases). A good fit is obtained only when including the effect of both forcings as we can see from Fig. 1.2. However, if one uses the solar radiative forcing estimates from the calculated increase in TSI, the model will not give a best fit to the observed global temperature records. To obtain the

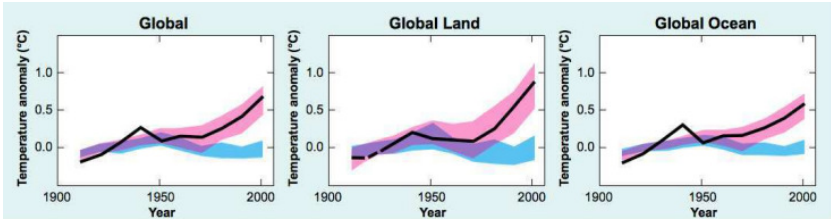


Figure 1.2: annual and decadal mean surface temperature from observations in black. The same are calculated using a model of the general circulation of the atmosphere and oceans, using all forcings (pink) and only natural forcings (blue). The width of the colored lines indicate the uncertainties in the estimates. From IPCC (2007).

best fit to the temperature data the model needs to amplify the magnitude of the solar forcing by a factor of 2 to 3 (Haigh 2007).

Explanations for the underestimate of the solar forcing may come from a too low value in the TSI increase estimates (Shapiro et al. 2011) or from climate models directly. If the present TSI increase estimates are correct, to explain the solar forcing underestimate in climate models it is necessary to account for mechanisms that might amplify the atmospheric response to solar variability. There are two potential mechanisms: one is the effects of solar UV radiation on the stratosphere and another one is the impact of cosmic ray flux on cloud formation. The UV spectrum shows variations from several percent up to more than 50% for the shorter wavelengths (see Sect. 1.3.2). The stronger variations in the UV spectrum may affect the temperature and ozone structure of the middle atmosphere. Indeed, the solar signal was found in the higher net production of ozone during periods of higher solar activity (Randel and Wu 2007). This takes place as ozone is produced by short wavelength solar UV and is destroyed at somewhat longer wavelengths, while the solar variation is greater in the far UV. Therefore, ozone production is modulated by solar activity stronger than its destruction. At the same time, since higher concentrations of ozone translate into greater absorption at wavelengths below 330 nm and above 500 nm (Haigh 2004), changes in the composition and the structure of the stratosphere could affect the radiation that reaches the lower atmosphere or tropopause and hence, lead to a rise in the temperature in these regions (Haigh 1994, 2007).

Solar activity also modulates the flux of the galactic cosmic rays reaching the Earth. The magnetic field of the heliosphere acts as a shield to cosmic rays, preventing mainly lower energy cosmic rays from entering the Earth's atmosphere. The very energetic particles will be unaffected and can reach the surface of the Earth producing cosmogenic isotopes. The number of cosmic rays that reach the Earth is not constant, being modulated by the solar activity. During periods of high activity, this is, when the number of sunspots, flares and coronal mass ejections is high, the heliospheric magnetic field deflects the cosmic rays more effectively. Thus, solar activity and the flux of cosmic rays reaching the Earth are anticorrelated. Cosmic rays could have an impact in cloud cover by changing the atmospheric ionization (Dickinson 1975, Marsh and Svensmark 2000). This idea is mainly based on observations of galactic cosmic ray counts and the global cloud cover over several solar cycles, the latter compiled by the International Satellite Cloud

Climatology Project, ISCCP. However, it is still not clear to what extent the cosmic rays induce the changes directly or if they are a proxy for another factor influencing the cloud cover, or if the correlation is real at all (Haigh 2007).

The rapid increase in global surface temperature in the last 40 years has brought back the debate to what extent variations in the solar radiative output can explain the global warming. Solanki and Krivova (2003) used the records of three possible solar quantities influencing the Earth's climate, namely the total solar irradiance, UV irradiance and the cosmic ray flux. These correlate well with the temperature record before 1970 but cannot explain alone the rise after 1970. They found that the Sun could contribute no more than 30% to the temperature increase, at least through the studied quantities. Solar radiative forcing is a quantity that needs to be taken into account if we want to understand the magnitude of the anthropogenic factors on the Earth's climate. For this reason reliable reconstructions of the solar irradiance back in time are needed.

At this point there are two main challenges important for the Earth's climate: the prediction of past solar irradiance variations and the prediction of future solar activity. The work presented in this thesis covers both the prediction of future solar activity and the prediction of past solar irradiance variations.

## 1.2 The Sun's magnetic cycle

This section describes different magnetic features found on the solar surface, which are strongly associated with solar activity. The distribution of the magnetic features on the photosphere is indicative of a large-scale magnetic field that changes polarity approximately every 11 years. This is seen in the characteristics and distribution of the sunspot groups. Therefore, the Sun's magnetic cycle has a mean periodicity of 22 years, with each cycle being different from each other.

### 1.2.1 Photospheric magnetic features

Magnetic structures are found over the whole Sun in a large range of sizes (from 100 km to small fractions of the whole solar surface), morphology, flux intensity (up to 6 kG) and with life times from hours to months (for a review of solar magnetic fields see Solanki 1993, 1998, Solanki et al. 2006). In general, three main zones can be distinguished on the solar surface: the *active regions*, the *ephemeral regions*, and the *quiet Sun*, i.e. everything else outside active regions.

Active regions are seen in the form of magnetic bipolar regions and are thought to be the result of emerging magnetic flux tubes, or clusters of concentrated field lines (Parker 1979, Spruit and Roberts 1983, Fan et al. 1994). The magnetic flux tubes travel all the way from the bottom of the convection zone and break through the solar surface. As the magnetic flux tubes rise, they interact with the ongoing convection and this is seen in the photospheric layers as a disruption in the granulation pattern (e.g. Zwaan 1985).

The most prominent manifestations of emergent magnetic flux are *sunspots*, dark regions of highly concentrated magnetic fields located at the footpoints where the flux tubes cut into the photosphere. They have diameters of 4000 km up to 50000 km. Their intense magnetic fields (1800 G on average for sunspot umbrae) inhibit the convective motions

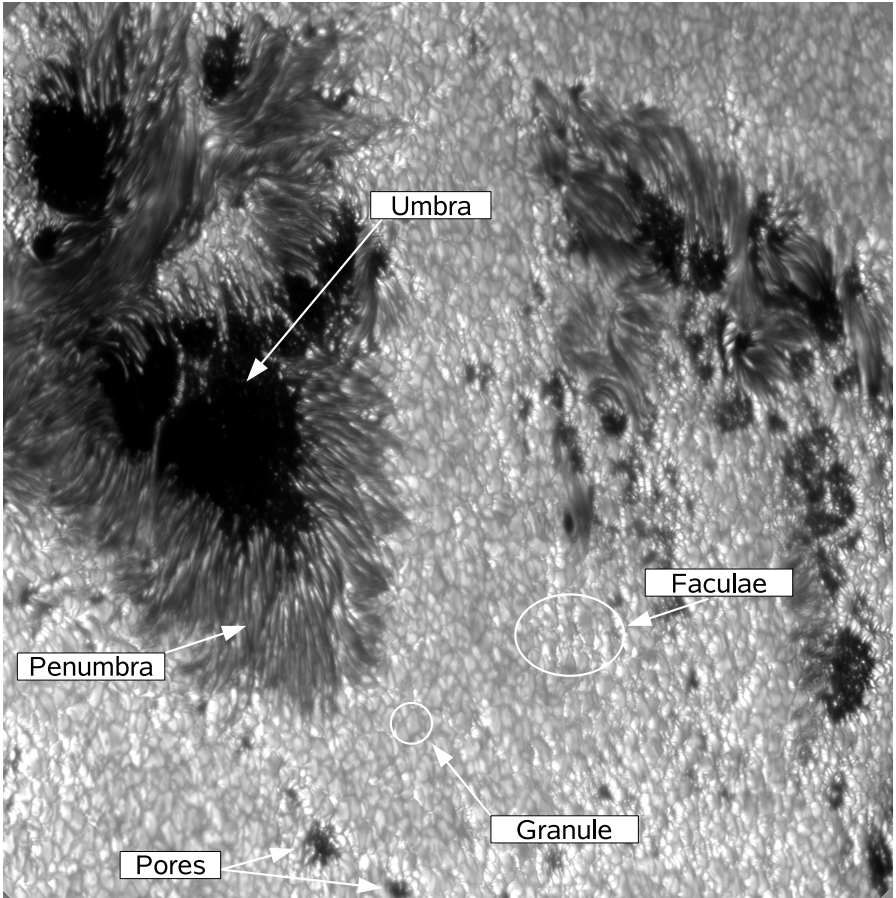


Figure 1.3: High resolution image of an active region near the solar limb in continuum at a wavelength of 487.7 nm taken with the 1-m Swedish Solar Telescope in La Palma (Spain) by Göran Scharmer in 2002. Superimposed on the image, the main features that compose the photospheric magnetic field are indicated by the white lines and circles.

that transport energy from the layers below the photosphere outwards, and thus these regions suffer of reduced surface temperatures. Other smaller dark regions (diameters of about 400 – 5000 km) found in active regions are pores. They do not develop penumbra as sunspots (Keppens 2000). Still smaller magnetic features with diameters smaller than 400 km can be seen all over the solar surface and are called *magnetic elements* (Solanki 1993). The magnetic elements are more frequent in active regions. Here they assemble to form faculae (or plage, as seen in the higher chromospheric layers). Faculae are seen in

white light or continuum images of the Sun as bright patches, specially near the limb. In contrast to sunspots, faculae are hotter and hence brighter than their surroundings at equal optical depth. The key to this difference in brightness lies in the *diameter* of the magnetic flux tubes and can be explained qualitatively via the “hot wall” effect. The walls of the flux tube are heated by the convective motions and for tubes with diameters of around 100 km or less, that result in faculae, the heat from the walls is able to penetrate the tube and heat up the material inside (e.g. Spruit 1976, Knölker and Schüssler 1988, Steiner and Stenflo 1990).

Outside of active regions, magnetic elements are located in the boundaries of supergranular cells and also, at smaller spatial scale, of granular cells (Title et al. 1987, Simon et al. 1988). Granular cells are signatures of convection cells and have diameters ranging from hundreds to thousands of kilometers. The magnetic elements trace the lanes that depict the pattern of comparatively narrow dark downflow lanes of plasma and central bright upflow cells characteristic of the granulation pattern. The magnetic elements located here form the so called *magnetic network*. Figure 1.3 is a high resolution continuum image of an active region in the Sun near the limb, taken with the Swedish Solar Telescope. The different magnetic features described in the main text are indicated by the white arrows and circles.

## 1.2.2 Large-scale structure

The solar surface magnetic field is highly structured down to scales that are at the limit of observational resolution (spatially, temporally and of magnetic intensity). However, the appearance and distribution in time of the photospheric magnetic features show evidence of the existence of an organized, large-scale magnetic field in the solar interior. The most obvious indicator is the sunspot cycle, discovered by Schwabe already in 1843.

Magnetic flux appears on the solar surface in the form of bipolar groups, seen in the photosphere as compact groups of individual sunspots (or sunspot groups). The sunspot groups exhibit a number of properties describing a pattern that repeats every approximately 11 years.

- *Sunspot number*: The number of sunspot groups seen on the solar surface vary periodically with time. At the beginning of a cycle, no sunspots (or very few) are observed. As the cycle advances in time, the rate of emerging spots increases until reaching a time of maximum. During the maxima the sunspots are so numerous that they may cover a few percent of the visible solar surface. The fractional coverage varies from cycle to cycle, which tells us that the cycles have varying amplitudes (highest value of monthly means of sunspot number) and strengths (total area covered by sunspots in one cycle). One can also see this in the bottom panel of Fig. 1.4 which gives daily means of sunspot area over time. After the maximum, the sunspot number decreases with time and reaches again a state of minimum. The time lapse between two consecutive minima specifies the duration or length of the cycle, which is also different for each cycle. The mean length of the sunspot cycles (as recorded since 1610) is 11.1 years, with some cycles being as short as 8 years and as long as 14 years.

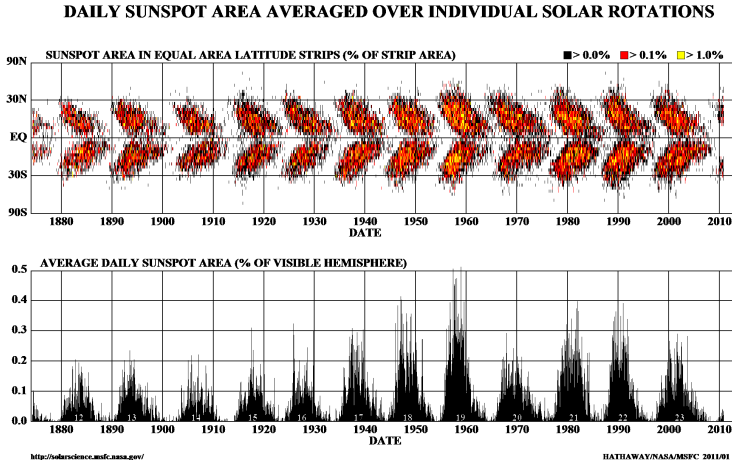


Figure 1.4: Butterfly diagram (top) and average daily sunspot area (bottom) taken from D. Hathaway (<http://solarscience.msfc.nasa.gov>).

- Latitude distribution:** During the cycle, sunspot groups are found in a range of latitudes between  $\pm 5^\circ$  and  $\pm 30^\circ - \pm 40^\circ$  more or less symmetrically with respect to the equator. These zones are called activity zones or activity belts. The first groups that appear at the beginning of the cycle are found at the higher latitudes and as the cycle progresses, the sunspots' emergence latitude is shifted towards the equator. This is clearly seen in the butterfly diagram, or equivalently, a plot of sunspot latitudes versus time. The top panel of Fig. 1.4 is a butterfly diagram for the period covering solar cycles 12 – 23. From the butterfly diagram one can also notice that around minima sunspots from both old (at low latitudes) and new cycles (at higher latitudes) coexist. Hence, consecutive cycles appear to overlap with each other during some periods.
- Tilt angles:** Sunspot groups have two distinct regions of opposite magnetic polarity, the leading or preceding portion being nearest to the equator and the following the farthest. The axis of sunspot groups make a small angle,  $\alpha$ , with the East-West direction (see Fig. 1.5). Usually, the more westward portion is closer to the equator than the following portion. The tilt angles have been observed to increase with the latitude of the sunspot group. This is known as Joy's law (Hale et al. 1919).
- Polarity rules:** The polarities of sunspot groups are arranged according to Hale's polarity laws (Hale and Nicholson 1925). (1) The polarity of the leading portion is the same for all pairs in one hemisphere but opposite in the other, and (2) this configuration remains for one cycle and reverses the sign in the next one. The original pattern repeats itself every two sunspot cycles, therefore its duration is of roughly 22 years and is referred to as the magnetic cycle of the Sun (Hale period).

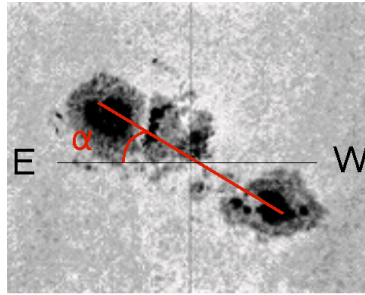


Figure 1.5: Schematic of the tilt angle,  $\alpha$ , presented by a sunspot group with respect to the east-west direction. The portion to the west corresponds to the leading polarity and the portion to the east the following polarity.

Other large scale patterns seen on the Sun are differential rotation and meridional circulation. The Sun rotates at different speeds according to latitude, i.e. it rotates faster at the equator than at the poles. This is known as differential rotation. The meridional circulation refers to the large scale flow from the equator towards the poles near the solar surface with a return flow in the opposite direction at the bottom of the convection zone. Although in principle there is no evidence for cyclic variations of differential rotation or meridional circulation, recent studies by Hathaway and Rightmire (2010) claim variations within the cycle. Other authors working on the solar dynamo assume variations of the meridional flow from cycle to cycle, needed to reproduce the polarity reversals (Wang et al. 2002, Dikpati and Gilman 2006).

### 1.2.3 Prediction methods

The prediction of future solar activity is of great interest since it is strongly associated with space weather events. The most direct impact comes from fast processes such as solar flares and coronal mass ejections which determine space weather and are of importance on a daily basis for, for example, communication satellites and space exploration. The amplitude and intensity of a sunspot solar cycle can give a qualitative measure of the number of the mentioned fast processes occurring during the maximum of a solar cycle. Hence, the great interest in solar cycle prediction.

The work done around solar cycle prediction is very extensive. A wide variety of prediction methods have been developed to predict solar activity at different time scales. This section is focused on prediction methods involved in solar cycle amplitude prediction. Following the classification by Petrovay (2010), the prediction methods are classified into three main groups: precursor, extrapolation, and model-based predictions. In contrast to the dynamo model-based predictions, precursor and extrapolation methods use observational data alone. In Sect. 1.2.3.1 we first discuss the extrapolation and precursor methods and in Sect. 1.2.3.2 we briefly review recent predictions based on solar dynamo models.

### 1.2.3.1 Statistical methods

*Precursor methods* aim at predicting an upcoming solar maximum by using a measure of solar magnetic activity (sunspot number, polar fields, geomagnetic indices) at a given time before the maximum is reached. Most of them use a characteristic of the preceding cycle(s) to determine the amplitude of the next.

The even-odd rule, also known as the Gnevyshev-Ohl rule, comes from the observation that odd numbered cycles are typically stronger than even numbered ones, so that there is a general tendency of alternation between even and odd cycles in amplitude (Gnevyshev and Ohl 1948). However, some exceptions can be found such as the pair of cycles 22-23, 17-18 and 7-8. Correlations between the amplitudes of consecutive cycles have also been found, and which have proven to be quite weak (0.35). Higher linear correlations are found between the activity level at cycle minimum and the monthly smoothed sunspot number of the next cycle maximum (Brown 1976) ( $r = 0.72$ ). This correlation can be further improved (up to values of  $r = 0.79$ ) when considering activity levels two to three years before cycle minimum (Cameron and Schüssler 2007, Petrovay 2010). However, they loose practical use in the sense that the epoch of the minimum cannot be known with certainty until around 2 years before maximum. Also, as discussed by Cameron and Schüssler (2007), these relations have no underlying physical connection as they can be explained by a combination of the Waldmeier effect and the overlap of cycles as seen, e.g., in the butterfly diagram. The Waldmeier effect is the anticorrelation between the length of the ascending phase, or rise time, and the amplitude of the same cycle. Hence, since stronger cycles have a steeper rise, the minimum will take place earlier, when the activity levels of the previous cycle haven't reached very low levels. A weak inverse correlation of about  $r = -0.35$  is also found between the total cycle length and the cycle amplitude first noticed by Wolf (1861). Correlations between the amplitude of cycle  $n$  and the length of cycles  $n - 1$  and  $n - 3$  are also found, with correlations of  $r = -0.35$  and  $r = -0.6$ , respectively (Hathaway et al. 1994, Solanki et al. 2002a).

Geomagnetic indices characterize the variability of the Earth's magnetic field. Geomagnetic disturbances can be caused by two different sources: solar activity (flares and coronal mass ejections) in phase with the sunspot cycle, and variations of the strength of the interplanetary magnetic field occurring mainly during the declining phase of the solar cycle (Feynman 1982). There are different indices characterizing different aspects or time scales of the dynamic geomagnetic field. The aa-index is a three hour weighted mean of the northern and southern k-index values measured by antipodal stations, where the k-index is a number that quantifies the geomagnetic activity relative to an undisturbed geomagnetic field. The relationship between the geomagnetic aa-index near the time of sunspot minimum and the amplitude of the next cycle was already studied by Ohl (1966). As with the relations with the sunspot number, the prediction can only be done shortly before reaching sunspot maximum as the aa-index minimum occurs after sunspot minimum.

*Extrapolation methods* are also called time series analysis. They use only a time series of a solar activity indicator, such as the sunspot number, under the assumption that it is homogeneous, in contrast to precursor methods where the solar cycles are taken as individual units from minimum to minimum. Thus, a prediction for any time during the solar cycle is equally valid.

Different approaches involve linear regression methods and spectral methods. Linear regression methods forecast the value of, for example, the sunspot number at a time  $t$ , by a linear combination of the values at all previous times (Brajša et al. 2009, Hiremath 2008). Spectral methods assume that the long term variation of solar activity is due to the effect of one or more periodic cycles. Examples of this method are frequency and Fourier analysis, where the sunspot number record is represented as the superposition of several periodic components. In the period spectrum of the sunspot number one can distinguish three main prominent peaks corresponding to the 11-year sunspot cycle, the 22-year cycle and a period of about 80 years associated to the Gleissberg cycle. Long-period fluctuations of the sunspot number were noticed by Gleissberg (1939) and are now associated with periodicities spanning a range of 60 – 120 years according to the period spectrum of the smoothed monthly sunspot number (Petrovay 2010).

### 1.2.3.2 Dynamo model based predictors

The observed properties of sunspot cycles (see Sect. 1.2.2) are indicative of an organized, large-scale magnetic field inside the Sun that reverses polarity every approximately 11 years. A prediction method based on the Babcock-Leighton mechanism was already proposed by Schatten et al. (1978). Although Schatten et al. (1978) did not make use of a mathematical model, they used polar field measurements as a proxy of the maximum sunspot number based on the idea that the polar fields and the toroidal fields that produce sunspots are related via differential rotation. A difficulty presented by this method is that direct measurements of the magnetic field in the polar areas of the Sun are only available since 1976 from Wilcox Observatory. Mathematical models based on dynamo theory, on the other hand, are used to reproduce the Sun's magnetic field and its evolution in time. In the recent years several authors have attempted to predict the amplitude of the upcoming solar cycle 24 using surface flux transport dynamo models (Dikpati and Gilman 2006, Choudhuri et al. 2007).

Current dynamo models basically solve the magnetohydrodynamical induction equation for the evolution of the mean large-scale magnetic field of the Sun. The mean large-scale magnetic field is assumed to be axisymmetric about the Sun's rotation axis and antisymmetric about the equatorial plane. Thus, it is useful to separate it into two components: poloidal (meridional) and toroidal (longitudinal). Now the dynamo problem comes down to the generation of toroidal field from an existing poloidal field, and a poloidal field from an existing toroidal field (Charbonneau 2010). The toroidal field is generally thought to be the product of the shearing due to differential rotation. After several rotation periods, the field lines from the poloidal field are wrapped around the rotation axis of the Sun, creating the toroidal field that resides in the bottom of the convection zone. The site and mechanism for the conversion of a toroidal to a poloidal configuration through the  $\alpha$ -effect is still not clear.

In interface dynamos, the  $\alpha$ -effect is located near the bottom of the convection zone. However, they had a limited success in reproducing observed characteristics of the solar cycle such as the butterfly diagram. In the flux transport dynamos, the  $\alpha$ -effect follows the Babcock-Leighton mechanism, where the rising flux tubes are twisted due to the action

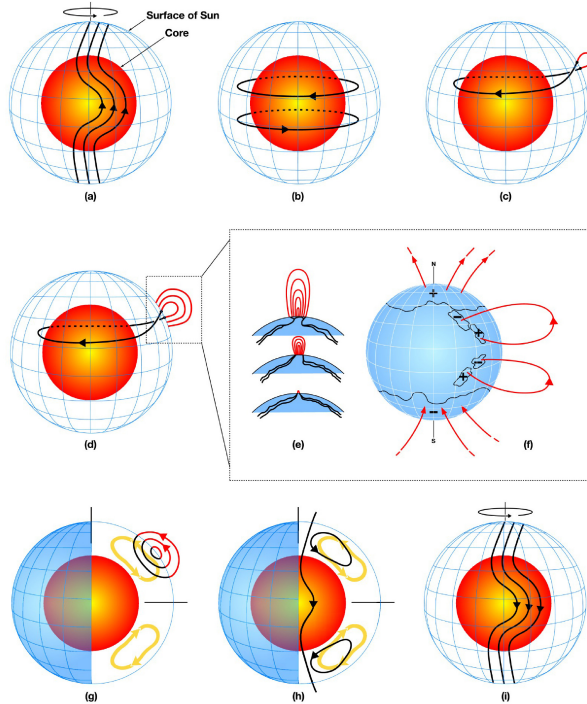


Figure 1.6: Schematic of solar flux transport dynamo process taken from Dikpati and Gilman (2009). The red inner sphere represents the radiative core of the Sun and the blue outer mesh the solar surface. In between the two layers is the convection zone, throughout which the dynamo process takes place. (a) Magnetic field lines from the poloidal field are sheared due to differential rotation near the base of the convection zone. (b) As a product, the toroidal field is produced. (c) When the toroidal field is amplified enough, it becomes buoyant and loops rise to the surface. The loops are twisted due to Coriolis force and appear as sunspots on the surface (black dots). (d)-(f) Additional flux emerges and spreads from decaying sunspots. The polarities, following Hale's law are specified. (g) Meridional circulation (yellow arrows) carries the magnetic flux poleward, (h) eventually reversing the polar field. Some of this flux is further transported towards the bottom of the convection zone and towards the equator. (i) The newly reversed poloidal flux is again sheared by differential rotation that will produce a toroidal field of opposite sign as in (b).

of the Coriolis force near the surface (Fig. 1.6). As a consequence, the axis connecting opposite polarities of the sunspot groups observed on the solar photosphere appears tilted with respect to the east-west direction, generating the poloidal field (Fig. 1.6(f)). Meridional circulation at the surface advects the magnetic flux from the sunspots to the poles,

reversing the polarity of the polar fields of the previous cycle (Fig. 1.6(g)). The reversing of the polar fields as observed from photospheric magnetograms occurs during sunspot cycle maximum. The equatorward return flow keeps transporting the toroidal field down to the base of the convection zone and towards low latitudes (Fig. 1.6(h)). When the field is sufficiently strong, it becomes buoyant giving rise to the emerging flux tubes that are seen as sunspots on the solar surface with opposite polarity configuration as the previous cycle (Fig. 1.6(i)).

Surface flux transport dynamo models can be further classified into advection or diffusion dominated models depending on the ratio of advective to diffusive time scales. In advection dominated models the magnetic diffusivity is less than  $20 \text{ km}^2\text{s}^{-1}$  so that the poloidal fields produced at the solar surface through a Babcock-Leighton type mechanism are basically transported to the bottom of the convection zone by the meridional circulation (Dikpati and Gilman 2006, Dikpati et al. 2006). At the typical speed of the meridional circulation (around  $10 \text{ km s}^{-1}$ ) the flux from active regions in a cycle takes around 30 years to reach the bottom of the convection zone. Hence, the toroidal field producing solar activity in a given cycle is a consequence of the shearing of the poloidal fields from 2-3 solar cycles earlier, giving the possibility of prediction. The diffusion dominated models use a higher value of the magnetic diffusivity of  $240 \text{ km}^2\text{s}^{-1}$  (Chatterjee et al. 2004, Choudhuri et al. 2007, Jiang et al. 2007). In this case, the poloidal fields diffuse downwards to the bottom of the convection zone within a time comparable to its transport to the poles by meridional circulation, i.e. not longer than one solar cycle. Thus the polar fields of cycles  $n$  and  $n-1$  are strongly correlated with the amplitude of cycle  $n$  (cf. Solanki et al. 2002a). However, the polar fields in this case are not a real physical precursor of the activity of the next cycle since their correlation is due to their common source.

As a follow up from the latter models, changes in the flow speed of the meridional circulation may be used as a precursor of the coming cycle since it influences the forming polar fields. In a recent study by Hathaway and Rightmire (2010), the authors show that the poleward flow has sped up in the late phase of cycle 23 as compared to the previous cycle. Flux transport models have shown that faster meridional flow will prevent leading polarities of sunspot groups to diffuse across the equator and cancel with the leading polarities of sunspot groups in the opposite hemisphere, resulting in weaker polar fields (Wang et al. 2009). These results, however, assume a latitude-independent meridional flow. On the other hand, Cameron et al. (2010) interpreted the variations found by Hathaway and Rightmire (2010) as changes in the characteristic latitudinal pattern followed by the meridional circulation instead of a fluctuation in the large-scale flow speed. Inflows towards the activity belts where active regions are found would suppress the transport of the following polarities to the poles resulting in lower polar fields (Jiang et al. 2010b). Helioseismic observations and the modeling of the intracycle variation of the meridional flow demonstrated that the amplitude of the inflows are correlated with cycle activity (Gizon and Rempel 2008) suggesting that the amplitude of these may also be correlated with the cycle strength. The fact that the amplitude of the inflows should increase with cycle strength is closely related to the cycle-to-cycle variation found in the observed cycle-averaged tilt angles of sunspot groups (Dasi-Espuig et al. 2010, see Ch. 2), as a possible explanation for the positive correlation with cycle strength. The inflows towards the ac-

tivity belts would act in opposite directions on the two distinct polarities of the sunspot groups, reducing the tilt angle. Thus, for stronger cycles the reducing effect would be stronger. This opens the possibility of using the sunspot group tilt angles as a predictor of the strength or amplitude of an upcoming cycle. Still, more work is required to test these results and the physical bases behind them.

## 1.3 Total solar irradiance

The previous section dealt with the magnetic features seen on the photosphere that compose solar activity and the various prediction methods of future solar activity. This section describes the prediction of past solar irradiance variations and in particular using the model SATIRE.

### 1.3.1 Measurements

Total solar irradiance (TSI) is the total energy received per unit area and time at the top of the Earth's atmosphere. Before the satellite era, TSI measurements from Earth didn't have enough precision to detect variability (thus the so-called "solar constant") as the Earth's atmosphere attenuates most of the solar radiation in the infrared and blocks it completely in the UV range below 300 nm in wavelength. Space-born measurements of the solar irradiance have been carried out almost continuously since November 1978 after the launch of the NIMBUS 7 spacecraft. Several instruments have been monitoring TSI since then during different periods of time: HF on Nimbus 7, ACRIM I on SMM, ERBE on ERBS, ACRIM II on UARS, VIRGO and DIARAD/VIRGO on board SOHO, ACRIM III on ACRIM satellite and TIM on SORCE.

Panel (a) in Fig. 1.7 shows daily averaged values of the TSI measured by different instruments. The accuracy of the measurements has proved sufficient to track variations on daily, rotational, and yearly time scales. However, as one can see from the plot, no single instrument has managed to survive longer than a single solar activity cycle. A careful cross-calibration to combine the data from the different radiometers must be done to create a coherent composite record that covers the full 2.5 cycles of measurements. Three independent composites are available and are presented in Fig. 1.7 from (b) the Physikalisch-Meteorologisches Observatorium Davos (PMOD) in Switzerland (Fröhlich 2000, 2003), (c) the ACRIM (Active Cavity Radiometer Irradiance Monitor) team (Willson and Hudson 1991, Willson 1997), and (d) the Institut Royal Meteorologique Belgique (IRMB) (Dewitte et al. 2004).

These composites show substantial differences, in particular regarding the long-term trend of the irradiance (Fröhlich 2006). This is best seen when comparing the relative TSI values between the minima preceding solar cycles 22 and 23. Both the IRMB and the ACRIM composites show a higher level of TSI during the minimum preceding solar cycle 23 relative to the minimum preceding solar cycle 22, this difference being largest for the ACRIM composite (Fig. 1.7(c)). In contrast, the PMOD composite shows a slight decline between the two solar minima of 1986 and 1996. Wenzler et al. (2009) and Krivova et al. (2009) employed a semi-empirical model that reconstructs TSI from available magnetograms (see Sect. 1.3.3) and found a good correspondence with the PMOD composite

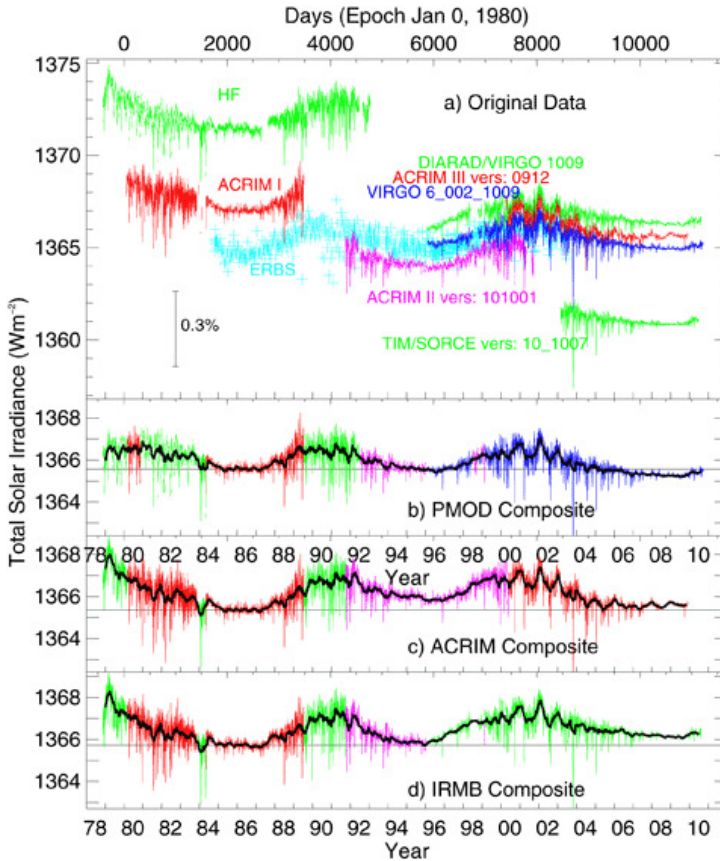


Figure 1.7: (a) Daily averaged values of the solar TSI from radiometers on different space platforms since 1978. The data are plotted as published by the corresponding instrument teams. The lower panels correspond to composites of TSI as daily values plotted in different colors to indicate where the data are coming from. The sources are (b) the Physikalisch-Meteorologisches Observatorium Davos (PMOD) in Switzerland, (c) ACRIM, and (d) the Institut Royal Meteorologique Belgique (IRMB). The black lines are one month running means. Courtesy C. Fröhlich (<http://www.pmodwrc.ch/pmod.php?topic=tsi/composite/SolarConstant>).

with no difference in the minima between the three cycles. The correspondence with the ACRIM and IRMB composites were significantly poorer. This implies that the irradiance changes as seen in the PMOD composite can be successfully reproduced by their model. Therefore, any secular trend (from minimum to minimum) in the TSI as seen

in the ACRIM and IRMB composites between 1978 and 2003, may be a consequence of a jump in the data from the HF radiometer that was not corrected in these other two composites.

Fröhlich (2009a) found that the TSI level from the PMOD composite during the past solar minimum in 2008-2009 was more than  $0.2 \text{ W m}^{-2}$  deeper than the minimum in 1996. He interpreted this decrease as a possible evidence against the magnetic origin of the secular change in the TSI. However do see the work by Krivova et al. (2011a), where their analysis suggests that the decrease seen in PMOD during 2008-2009 is more likely to be due to problems with the PMO6V radiometers.

### 1.3.2 Variations and their origin

The irradiance measurements have proven irradiance to vary at all measured time scales. The measurements were presented in the previous section and are plotted in Fig. 1.7, showing a noisy appearance due to the short term fluctuations and an overall 11-year modulation in phase with that seen from the sunspot number and sunspot area. The typical magnitude of the variation from cycle minimum to maximum in the total solar irradiance for the past 3 cycles is about 0.1%, although at shorter time scales (days), changes up to about 0.3% have been recorded. Solar irradiance variations also show a strong wavelength dependence (see Fig. 1.8). Although the contribution at wavelengths shorter than 400 nm to the total solar irradiance (red histogram in Fig. 1.8) is only around 8%, 60% of the total irradiance changes over the solar cycle are produced in this spectral range (blue histogram in Fig. 1.8). In the UV part of the spectrum, solar irradiance can vary from several percent up to more than 50% at wavelengths around 100 nm.

Irradiance variations at time scales of minutes to hours are mainly due to the changing granulation pattern (Solanki et al. 2003). Granules are seen in the photosphere and are the signatures of convective cells (see Fig. 1.3 in Sect. 1.2.1). In the convective cells, the hot material flows up from subphotospheric layers to the surface appearing as bright cells. At the surface the material cools and falls back into the interior creating darker and narrower downflow lanes that surround the bright cells. The granulation pattern is constantly changing every 5–10 min according to their typical lifetimes, so that the evolving bright upflow cells and dark downflow lanes dominate the irradiance variations at such time scales.

At time scales longer than hours, irradiance changes are thought to be due, primarily, to the evolving magnetic fields on the solar surface. Different other mechanisms have been considered to explain irradiance variations. Some of these suggestions are that irradiance changes are driven by variations in the internal structure altering the convective energy transport and thus, global temperature changes (Sofia and Li 2004, Tapping et al. 2007), or variations in the solar radius (Hoyt and Schatten 1993, Antia 2003). For further details on these other mechanisms see Domingo et al. (2009). However, empirical models that reconstruct total solar irradiance variations taking into account only the effect of the magnetic fields on the solar surface are able to reproduce up to 96% of the observed irradiance variations (Krivova et al. 2003, Ball et al. 2011).

Observing an image of the solar photosphere, e.g. Fig. 1.3, suggests that the brightness of the solar disc is rather heterogeneous and linked to the different features on the photosphere. At the same time, these features are the result of emergent magnetic flux (see

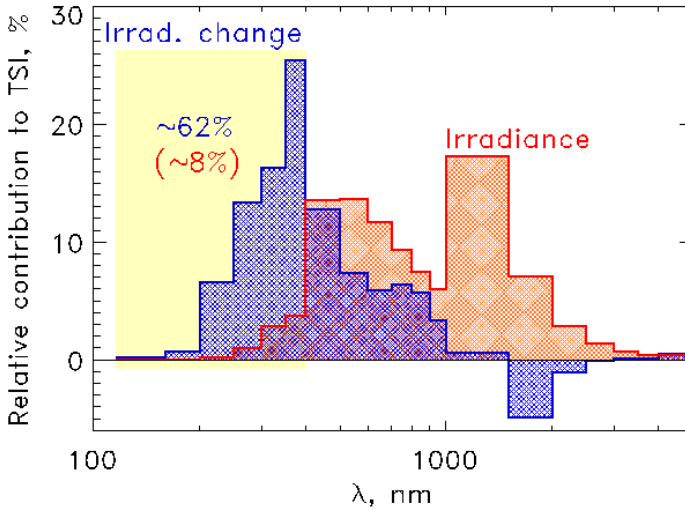


Figure 1.8: The red histogram is the relative contribution to the total solar irradiance of different wavelength ranges and the blue histogram is the relative contribution to the solar cycle variations. The area marked in yellow corresponds to the spectral range where about 60% of the total irradiance variations occur. Courtesy of N. A. Krivova.

Sect. 1.2.1) that evolves in time. The photospheric magnetic features are important contributors to the solar irradiance, since they have different brightness contrasts compared to the quiet Sun. The quiet Sun is, as a first approximation, assumed to be field-free<sup>1</sup> and any changes in the brightness of the photospheric magnetic features are compared to the quiet Sun brightness.

Sunspots, with temperatures roughly between 3000 K and 5000 K, are cooler than their hotter surroundings (at equal optical depth)<sup>2</sup> at about 5780 K (Thomas and Weiss 2008). The facular brightness depends further on their position on the solar disc, wavelength, and magnetic field strength (Ortiz et al. 2002, Solanki and Krivova 2009). The dependence of the brightness on the position on the solar disc, or more specifically on the heliocentric angle  $\mu = \cos \theta$ , is usually referred to as center-to-limb variation (CLV). The continuum brightness contrast of the magnetic elements exhibits increasing values as the limb is approached until reaching a maximum and thus, faculae near the limb appear so prominent. The “hot wall” model (see Sect. 1.2.1) also explains qualitatively the CLV. At

<sup>1</sup>The quiet Sun contains weak magnetic fields located in the interiors of supergranules in the so-called intranetwork (Livingston and Harvey 1971, 1975, Zhang et al. 1998).

<sup>2</sup>For a tube in pressure equilibrium with the exterior, the pressure inside the gas is reduced because of the presence of magnetic pressure and thus the optical depth at unity level is lowered. Looking inside the tube we see deeper layers of the atmosphere than the surrounding (Wilson depression).

disc center,  $\mu = 1$ , faculae are observed with a vertical *line-of-sight* (LOS), so that one would be looking directly into the flux tube. However, for higher values of  $\mu$ , i.e. closer to the limb, the LOS is no longer vertical and hence one would be seeing the hot walls of the flux tube instead (see the sketch in Fig.10 by Spruit 1976).

### 1.3.3 SATIRE models

The previous section discussed the physical effects of the surface magnetic features on the emergent intensity and thus the TSI variations. Based on these ideas many models have been developed to reconstruct irradiance to both test the physical models that postulate that irradiance variations are caused by the surface magnetic fields (see, e.g. Domingo et al. 2009), and to extend the irradiance record beyond the time for which measurements are available. Different models use different proxies of solar activity to determine the fraction of the solar surface that is covered by a certain magnetic feature, i.e. sunspots or faculae. Simpler models involve photometric indices for sunspot darkening and facular brightening that describe the fractional change in irradiance caused by sunspots and faculae, respectively, relative to the quiet Sun (Lean et al. 1998, Lean 2000, Fröhlich 2009b). The photometric indices obtained from observations, e.g. white light images are used to retrieve information on sunspots, and CaII K images for faculae. In these models a linear combination of the photometric indices is used to describe irradiance changes in time. More advanced irradiance models include physical models to describe the contrast of the magnetic features as a function of wavelength and disc position. The fraction of the solar disc covered by each component is also obtained from photospheric images and CaII K images or magnetograms. The key difference of the more advanced models with respect to the former is that they characterize the different time dependent magnetic features on the solar surface by time-independent model atmospheres (Fontenla et al. 1999, Fontenla and Harder 2005, Unruh et al. 1999) and thus don't rely solely on linear regressions to compute solar irradiance.

One example of the models of the second type is the SATIRE (Spectral And Total Irradiance REconstructions) model. SATIRE is also based on the assumption that irradiance changes on time scales of days or longer are caused by surface magnetic fields. The surface magnetic features are divided into various atmospheric components, each described by a characteristic brightness spectrum from corresponding model atmospheres (Unruh et al. 1999). Three versions of SATIRE have been developed depending on the considered time scale at which irradiance is reconstructed (Krivova et al. 2011a). *SATIRE-S* is used to model solar irradiance in the satellite era (since 1974) with high precision using magnetograms (see Fig. 1.9; Fligge et al. 2000, Krivova et al. 2003, Wenzler et al. 2004, 2005, 2006, Ball et al. 2011) and has been quite successful, reproducing up to 96% of the observed irradiance variations. *SATIRE-T* is used for the telescope era (since 1610) and uses the sunspot number record (Balmaceda et al. 2007, Krivova et al. 2007, 2010), and *SATIRE-M* reconstructs irradiance at millennial timescales (Krivova et al. 2011b, Vieira et al. 2011, Krivova et al. 2010) using sunspot numbers reconstructed from the  $^{10}\text{Be}$  and  $^{14}\text{C}$  concentrations.

To obtain the solar irradiance at a given time,  $t$ , and wavelength,  $\lambda$ , with a SATIRE type model it suffices to derive the filling factors,  $f^a(t)$ , that quantify the amount of the solar surface that is covered by a given magnetic feature,  $a$  (i.e. sunspot umbra, penumbra,

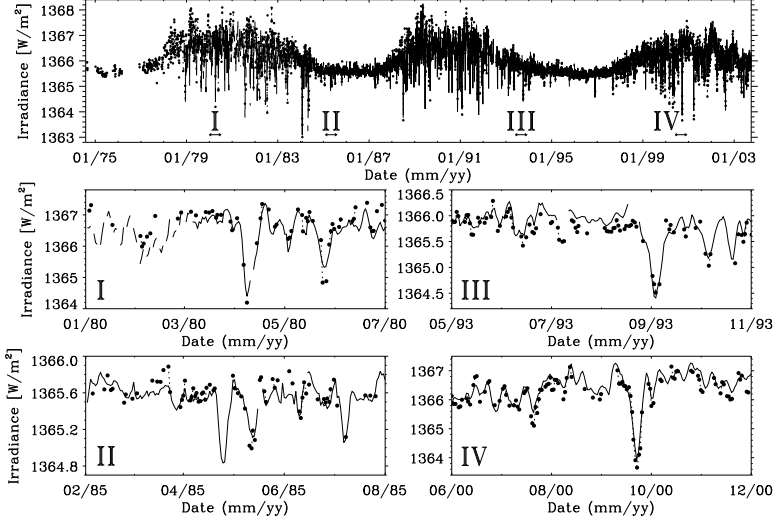


Figure 1.9: Top panel: PMOD composite record of total solar irradiance (solid line) and reconstructed daily total solar irradiance based on NSO-512 data (filled circles connected by the dotted lines when there are no data gaps) from the minimum of cycle 21 to the maximum of cycle 22. Middle and lower panels: Enlargements of four shorter intervals corresponding to double-headed arrows under roman numerals. Plot taken from Wenzler et al. (2006).

faculae, or network), and their respective radiative flux,  $F^a(\lambda)$ . Following the formalism in Krivova et al. (2011b), the solar irradiance,  $S(t, \lambda)$ , is then given by the sum of the radiative flux contribution of each individual magnetic component, and the quiet Sun, weighted by its filling factors

$$S(t, \lambda) = \sum_a f^a(t) F^a(\lambda) + \left(1 - \sum_a f^a(t)\right) F^q(\lambda). \quad (1.2)$$

Since the magnetic field distribution on the solar surface is divided into different magnetic features, the filling factor for the quiet Sun is everything else that is not covered by any of the magnetic components. This expression can be modified to include positional information of the different components. In this case, the global filling factors  $f^a$  are substituted by local filling factors  $\alpha_{i,j}^a$ , where  $(i, j)$  denote a particular pixel in a solar image or magnetogram, and the radiative fluxes  $F^a$  are substituted by intensities  $I^a(\mu)$ , where  $\mu = \cos \theta$  and  $\theta$  is the heliocentric angle,

$$S(t, \lambda) = \sum_{i,j} \left[ \sum_a \alpha_{\mu(i,j)}^a(t) I_{\mu(i,j)}^a(\lambda) + \left(1 - \sum_a \alpha_{\mu(i,j)}^a(t)\right) I_{\mu(i,j)}^q(\lambda) \right]. \quad (1.3)$$

Note that the modelled intensities are assumed to be independent of time. The time evolution of solar irradiance is given by the changing surface distribution of the magnetic

features. It is also important to point out that the positional information is only available in the case of the SATIRE-S, where magnetograms are used to derive the filling factors. Thus, SATIRE-S employs Eq. (1.3) while the SATIRE-T and SATIRE-M models solve Eq. (1.2). The SATIRE-S model is described in more detail as it has been used in the work presented in this thesis.

The SATIRE-S model takes into account 4 main components: the quiet Sun, faculae and network, sunspot umbra, and sunspot penumbra (hereon denoted by the superscripts  $q, f, u, p$ , respectively). Fligge et al. (2000) and Krivova et al. (2003) used continuum images to locate the pixels  $(i, j)$  that are covered by sunspot umbra and penumbra, and magnetograms to locate the pixels  $(i, j)$  where faculae and the network fall. These masks of the magnetic feature distribution are then used to compute the filling factors  $\alpha_{\mu(i,j)}^a$ . The sum of the 4 filling factors for one pixel  $(i, j)$  at a given time,  $t$ , is equal to 1, so that the magnetic flux of each pixel is completely described by the four main components of the model in different proportions. The filling factor for the quiet Sun is given by  $\alpha^q = 1 - \alpha^f - \alpha^u - \alpha^p$ .

The intensity of each component,  $I_{\mu}^{q,f,u,p}(\lambda)$  as a function of wavelength,  $\lambda$ , and position,  $\mu$ , is computed from a set of model atmospheres (Unruh et al. 1999). Unruh et al. (1999) calculated  $I_{\mu}^{q,f,u,p}(\lambda)$  using the spectral synthesis code ATLAS9 of Kurucz (1992) from plane-parallel model atmospheres. The quiet Sun is described by the standard model atmosphere FAL-C while for faculae a modified version of FAL-P of Fontenla et al. (1993) is employed (for details see Unruh et al. 1999). Sunspot umbra and penumbra are described by a radiative equilibrium model (Kurucz 1991, Solanki 1997) with effective temperatures of  $T_{\text{eff}} = 4500$  K and  $T_{\text{eff}} = 5450$  K, respectively.

The model has one free parameter,  $B_{\text{sat}}$ , that enters in the calculation of the filling factors of faculae. Since the magnetic elements forming faculae are usually not spatially resolved by observations <sup>3</sup> there is an ambiguity between the apparent field strength as measured by magnetograms and the intrinsic field strength of the elements. The apparent field strength depends on the spatial resolution of the observations, therefore, the intrinsic field strength is always higher or equal to the apparent field strength. The difference between apparent and intrinsic field strength implies that the magnetic elements only fill a fraction of the solar surface within a spatial resolution element (i.e. pixel  $(i, j)$ ). The free parameter  $B_{\text{sat}}$ , thus represents the value of the magnetogram signal at which the pixel is fully represented by the FALP model atmosphere. The value of  $B_{\text{sat}}$  is found by fitting the irradiance reconstructions with observations.

To obtain the total solar irradiance with a 4-component SATIRE-S model Eq. (1.3) is integrated over all wavelengths with  $a = f, u, p$ .

$$S(t) = \int_{\lambda} \sum_{\mu(i,j)} \left[ \alpha_{\mu(i,j)}^q(t) I_{\mu(i,j)}^q(\lambda) + \alpha_{\mu(i,j)}^f(t) I_{\mu(i,j)}^f(\lambda) + \alpha_{\mu(i,j)}^u(t) I_{\mu(i,j)}^u(\lambda) + \alpha_{\mu(i,j)}^p(t) I_{\mu(i,j)}^p(\lambda) \right] d\lambda \quad (1.4)$$

---

<sup>3</sup>Recent observations from the SUNRISE balloon-borne solar observatory yielded high-quality data, being able to detect and totally resolve magnetic fields at a resolution of 100 km in the quiet Sun (e.g. Lagg et al. 2010, Solanki et al. 2010)

### 1.3.4 Secular trend

Different historic proxies of solar magnetic activity like sunspot, auroral and geomagnetic records, as well as cosmogenic isotope concentrations suggest that it also varies on longer time scales (e.g. Eddy 1976, Lockwood et al. 1999, Solanki et al. 2004). On average, solar activity has increased since the Maunder minimum (see Fig. 1.1, Solanki et al. 2004). Different TSI reconstructions in the past have used diverse methods to estimate the increase of the TSI since the Maunder minimum.

As described in Sect. 1.3.3, the SATIRE-S model is used to reconstruct solar irradiance during the period when measured magnetograms are available, i.e. since 1974. If one wants to reconstruct solar irradiance further back in time, one uses SATIRE-T or SATIRE-M depending on how far back the reconstruction goes. Records of sunspot areas and positions have been employed to describe the evolution of sunspots and go as far back as 1874. Before that one has to rely on the sunspot number recorded since 1610 or concentrations of cosmogenic isotopes to derive sunspot numbers. However, a long and reliable proxy for facular areas is not yet available and thus their evolution is obtained by assuming that the facular areas are related to those of sunspots (Chapman et al. 1997). This is a reasonable assumption since both are found in active regions. The weak magnetic features like e.g. ephemeral regions, are, however, not well represented by the sunspot areas. For this reason estimating long term trends in the solar irradiance is a difficult task. Precisely, it is the long term trends of solar irradiance that are of interest for climate studies.

The first reconstructions of TSI that go back to the Maunder minimum (Zhang et al. 1994, Lean et al. 1995) used the stellar observational analysis from Baliunas and Jastrow (1990) to estimate the secular change in irradiance. However, the stellar data from Baliunas and Jastrow (1990) were later revised and their original results were not confirmed (Hall and Lockwood 2004), proving the stellar data to be an unreliable source from which to estimate the secular variation. A physical mechanism that produces a secular variation is the overlap of the activity cycles of ephemeral regions (Harvey 1992) and was proposed by Solanki et al. (2000, 2002b). Ephemeral regions are small bipolar regions with lifetimes of around a day, found at all latitudes on the solar surface. Thousands of ephemeral regions emerge during a day, with their total magnetic flux equivalent to that of one or more major active regions (Harvey 1992, 2001). The ephemeral regions present a cyclic variation as that of sunspots, appearing at the solar surface already during the descending phase of the previous sunspot cycle (see Sect. 4.3). Therefore, a significant background magnetic flux is present during sunspot minima that could lead to a secular change.

The model developed by Solanki et al. (2000, 2002b) reconstructs the total and open flux back to 1700 from the sunspot number. The results from their model were compared to the open flux reconstructed by Lockwood et al. (1999) from the geomagnetic aa-index and found to be in good agreement. The results also indicated a doubling of the total surface magnetic flux since the beginning of the last century. The time evolution of the total surface magnetic flux is of importance for the understanding of solar irradiance since it is the cause of irradiance variations. Using the model of Solanki et al. (2002b), Balmaceda et al. (2007) and Krivova et al. (2007, 2011b) have computed the TSI since 1610 with a SATIRE-T type model and retrieved a value of the increase of around  $1.25 \text{ W m}^{-2}$  within an uncertainty range of  $0.9 - 1.5 \text{ W m}^{-2}$ . Figure 1.10 plots the TSI recon-

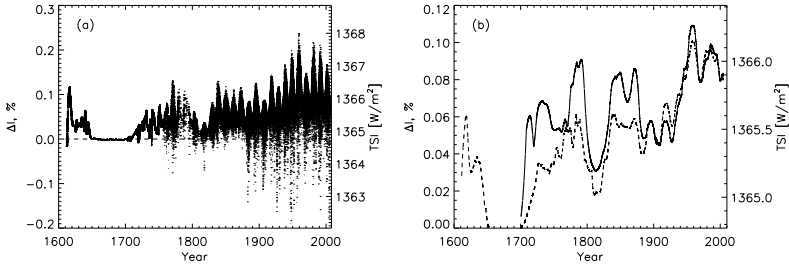


Figure 1.10: Total solar irradiance reconstructions since 1600 from Krivova et al. (2007) (a) for the model based on the Group sunspot number, and (b) 11-year running mean of the reconstructions for the model based on Group (dashed line) and Zurich (solid line) sunspot numbers.

structions by Krivova et al. (2007), from which we can clearly notice the increase since the end of the Maunder minimum. Wang et al. (2005) also included the contribution of the ephemeral region flux, although they neglected the extended length of the ephemeral region cycles. They used a surface flux transport model to simulate the evolution of the photospheric magnetic flux. From this, they calculated the TSI including the facular brightness variations between the cycle minima in the model of Lean (2000). Their estimate of the increase is of around  $1 \text{ W m}^{-2}$  since the beginning of the 18th century. The two estimates are consistent with other estimates derived under various assumptions (Foster 2004, Crouch et al. 2008, Steinhilber et al. 2009). Recently, two new and controversial estimates have been published by Shapiro et al. (2011) and Schrijver et al. (2011). Shapiro et al. (2011) assert that the whole solar surface during the Maunder minimum had an intensity brightness equivalent to that seen in the darkest parts of supergranular cells, obtaining a substantially larger increase in the TSI of  $6 \pm 3 \text{ W m}^{-2}$  since then. In contrast, Schrijver et al. (2011) claim that the TSI levels during low activity phases like the Maunder minimum are comparable to the period of the minimum in 2008-2009. Therefore, their work suggests little or no relative TSI change between the present and the Maunder minimum ( $\approx 0.03 \text{ W m}^{-2}$ ).

The aforementioned TSI reconstructions reproduce the observations fairly well but diverge as they go back in time, so that the TSI increase since the Maunder minimum is sensitive to the choice of the reconstruction. When reconstructing back to 1700 or further, assumptions on the amount of faculae and network present on the photosphere and on the quiet Sun intensity have to be made. It is here where the biggest uncertainties enter in the TSI models. The network fields play a major role during epochs of extended low activity since it is still not clear whether they are a consequence of the solar activity directly linked to the global dynamo action or are created by a local dynamo on the solar surface (Vögler and Schüssler 2007, Danilovic et al. 2010). If the former were the case, during epochs like Maunder minimum when the global dynamo was not operating, the network field would not be present. This is the case for the TSI reconstructions that rely

only on sunspot proxies, since the only source of faculae and network are the sunspots. Thus, if there are no sunspots on the solar surface there are no faculae nor network. If the network field were to be created by a local dynamo, then it would be present on the solar surface since the local dynamo can operate independently from the global 11-year solar dynamo. The reconstructed TSI during the period of the Maunder minimum would then give lower values if the network field is assumed to have disappeared and the increase in TSI since the Maunder minimum will be higher in comparison to reconstructions that assume that the network is still present. However, the operation of the local dynamo on the solar surface is itself an open topic that requires further investigation.

## 1.4 Outline of the thesis

In the past century a lot of work has been done regarding the prediction of future and past solar activity, given its importance for the Earth's climate. The work done in this thesis covers both, where a new physics-based proxy for the prediction of future solar activity (Ch. 2) and a more realistic method for the reconstruction of past solar irradiance (Ch. 3 and Ch. 4) are presented.

Chapter 2 focuses on the potential of using the tilt angle of sunspot groups as a proxy to forecast the amplitude of the sunspot cycles. The sunspot records from the Mount Wilson and the Kodaikanal observatories cover almost 80 years (7 solar cycles) of continuous observations and provide measurements of the tilt angles of sunspot groups (Howard et al. 1984, Howard 1991, Sivaraman et al. 1993, 1999). Hence, the great value of these data sets. We have analysed the data from the two observatories on a cycle-to-cycle basis to see how the tilt angle of the sunspot groups varies and to test the relationship between the average tilt angle of all sunspot groups in one solar cycle and other parameters of the solar cycle such as the length, amplitude, and strength. Anti-correlations are found between the cycle averaged tilt angle and the amplitude and strength of the same cycle, useful to estimate the average tilt angle of the sunspot groups of solar cycles for which only the sunspot number is known. The positive correlations between the cycle averaged tilt angle of a cycle and the amplitude and strength of the next cycle may be used as a predictive tool. With a tilt angle expression based on the Babcock-Leighton idea of the solar dynamo, we are able to predict the amplitude of the following solar cycle around 10 years before the maximum is reached. Also, since this relationship is linked to the Babcock-Leighton mechanism, the results obtained favour this type of dynamo.

The cycle-to-cycle variation of the tilt angles of sunspot groups was implemented by Cameron et al. (2010) in the surface flux transport model developed by Baumann (2005). The surface flux transport model computes the distribution of the magnetic field on the solar surface at any time, given the areas and positions of the sunspot groups. The output is thus equivalent to a magnetogram. Cameron et al. (2010) showed that the global diffusive term in their model was no longer needed to reproduce correctly the open flux and the polar field reversal times if the cycle-to-cycle variation of the tilt angles was included. Here we use the improved surface flux transport model of Cameron et al. (2010) to obtain simulated magnetograms. From these we are able to reconstruct the total solar irradiance with the SATIRE-S model, so that the changes in the total solar irradiance are described by the evolution of active regions alone. Chapter 3 briefly describes the surface flux

transport model and explains how the SATIRE-S model is adopted to the employment of the simulated magnetograms from which we reconstruct the total solar irradiance for the period of observations.

The results presented in Chapter 3 show that reconstructing the total solar irradiance with the SATIRE-S model and the simulated magnetograms is not enough to reproduce correctly the irradiance of the PMOD composite of observations during the minima and the ascending phases. We therefore included the flux from ephemeral regions in Chapter 4. The ephemeral regions are small bipolar regions. The overlap of their cycles was already proposed by Solanki et al. (2000, 2002b) to explain the secular variation seen in the total magnetic flux. The ephemeral regions also play a role in the irradiance since they provide a background field that changes the level of the quiet Sun, leading to a secular change. In Chapter 4 we describe the scheme followed to model the ephemeral region cycles to include their magnetic flux in the SATIRE-S model. After this improvement, we reconstruct the total solar irradiance since 1878 to study longer term variations and its secular increase. We also compare our results with those from Krivova et al. (2007) and Wang et al. (2005) and discuss the possible causes of their differences.

Finally, Chapter 5 summarises the results presented in the previous chapters and gives an outlook into the ongoing and future work.

## 2 Sunspot group tilt angles and the strength of the solar cycle \*

### 2.1 Abstract

It is well known that the tilt angles of active regions increase with their latitude (Joy's law). It has never been checked before, however, whether the average tilt angles change from one cycle to the next. Flux transport models show the importance of tilt angles for the reversal and build up of magnetic flux at the poles, which is in turn correlated to the strength of the next cycle. Here we analyse time series of tilt angle measurements and look for a possible relationship of the tilt angles with other solar cycle parameters, in order to glean information on the solar dynamo and to estimate their potential for predicting solar activity. We employed tilt angle data from Mount Wilson and Kodaikanal observatories covering solar cycles 15 to 21. We analyse the latitudinal distribution of the tilt angles (Joy's law), their variation from cycle to cycle, and their relationship to other solar cycle parameters, such as the strength (or total area covered by sunspots in a cycle), amplitude, and length. The two main results of our analysis follow. 1. We find an anti-correlation between the mean normalised tilt angle of a given cycle and the strength (or amplitude) of that cycle, with a correlation coefficient of  $r_c = -0.95$  (99.9% confidence level) and  $r_c = -0.93$  (99.76% confidence level) for Mount Wilson and Kodaikanal data, respectively. 2. The product of the cycle's averaged tilt angle and the strength of the same cycle displays a significant correlation with the strength of the next cycle ( $r_c = 0.65$  at 89% confidence level and  $r_c = 0.70$  at 92% confidence level for Mount Wilson and Kodaikanal data, respectively). An even better correlation is obtained between the source term of the poloidal flux in Babcock-Leighton-type dynamos (which contains the tilt angle) and the amplitude of the next cycle. Further we confirm the linear relationship (Joy's law) between the tilt angle and latitude with slopes of 0.26 and 0.28 for Mount Wilson and Kodaikanal data, respectively. In addition, we obtain good positive correlations between the normalised-area-weighted tilt angle and the length of the following cycle, whereas the strength or the amplitude of the next cycle does not appear to be correlated to the tilt angles of the current cycle alone. The results of this study indicate that, in combination with the cycle strength, the active region tilt angles play an important role in building up the polar fields at cycle minimum.

---

\* This chapter is published in *Astronomy & Astrophysics*, **518**, 7D (2010)

## 2.2 Introduction

Solar cycles differ from each other, showing different lengths, amplitudes, and strengths. Understanding the cause of such variations and, ideally, reproducing them is one of the aims of dynamo theory.

Magnetic flux transport dynamo models of the Sun's global magnetic field have been shown to reproduce the amplitude and duration fairly well, among other characteristics, of the solar cycle for a few cycles at least (Charbonneau 2005, 2007, Dikpati and Gilman 2006). Some of the key ingredients of such models include differential rotation, meridional flow, latitude distribution of sunspots, latitudinal drift, and a systematic tilt angle of the bipolar groups (Joy's law). These ingredients together explain the polarity reversal of the magnetic field at the poles every  $\sim 11$  years. Due to differential rotation, the magnetic field lines are wound up around the Sun's rotation axis and when this field is strong enough it becomes buoyant and rises to the surface as sunspots (Babcock 1961, Dikpati and Gilman 2008). The magnetic flux from the sunspots is carried by the meridional flow to the poles, finally causing the reversal. It was already proposed by Leighton (1969) that for the reversal to occur there must be cancellation between the leading portions of spots on opposite hemispheres through the slight tilt of the bipolar regions. In this way a greater fraction of the following polarity flux reaches the poles.

Schrijver et al. (2002) tested the hypothesis where the polar magnetic field on the Sun is determined by the accumulation of field transported poleward from sunspots at lower latitudes as a consequence of the tilt in the bipoles. Their model was not able to reproduce the polar field measurements of the past years if only the rate at which sunspots emerge is varied from one cycle to another. Furthermore, Wang et al. (2002) included a cycle to cycle variable meridional flow in order to achieve agreement with other observations, demonstrating that this variable meridional flow could serve as a regulator of the polarity reversal process. Flux-transport simulations have also shown that the strength of the polar fields, which feed the dynamo and help determine the strength of the next cycle, is sensitive to the average tilt angle of the active regions of the previous cycle (Baumann et al. 2004). Here we investigate whether there is a variation in the cycle-averaged tilt angle and Joy's law from cycle to cycle and whether there is a relationship between the tilt angles and the strength, i.e. the activity level, of the following cycle.

Previous studies of the sunspot tilt angles have mainly focused on their relationship with other spot parameters such as magnetic flux, drift motions, rotation, area, polarity separation, and cycle phase among others (Howard 1991, 1996, Sivaraman et al. 2007). Variations from one activity cycle to the next, however, have never been explored. This could shed some light on the mechanism by which the magnetic field of active regions is transported to the poles and may thus have the potential for forecasting future solar activity.

Prediction of future solar activity is one of the main challenges in solar physics and is not only of scientific importance but potentially helps to make predictions about changes to our natural environment that can affect our lives, e.g. space weather and Earth's climate. Most of the present day predictions are based on statistical analyses of solar activity in the past (Hathaway et al. 1999, Hathaway 2009). A more physics-based approach is offered by models of the evolution of the Sun's magnetic field, although recent dynamo

computations have given controversial results for cycle 24 (Dikpati and Gilman 2006, Choudhuri et al. 2007, Jiang et al. 2007).

The paper is structured as follows. In Sect. 2.3 we describe the data, the method and some tests. Section 2.4 presents the results, which are then discussed in Sect. 2.5. In Sect. 2.6 we present our main conclusions.

## 2.3 Data and tests

### 2.3.1 Data

For our analysis we employ sunspot data derived from white light images taken at Mount Wilson and Kodaikanal observatories. These observatories have regularly observed the solar disc in white light since the beginning of the 20th century. The data we use cover the years 1917 to 1985 and 1906 to 1987 for Mount Wilson and Kodaikanal, respectively. This means that cycles 15 to 21 are completely covered by the Kodaikanal (hereafter KK) record, but the first 4 years of cycle 15 and the last year of cycle 21 are missing in the Mount Wilson (hereafter MW) series. Howard et al. (1984) measured the positions and areas of individual sunspots on digitised MW images and then grouped the sunspots using a technique based on proximity. The grouping of individual sunspots was done by Howard et al. (1984) by applying a running box,  $3^\circ$  wide in latitude and  $5^\circ$  wide in longitude, centred at each spot on the solar disc. Any other spot that fell inside the box was included as part of the group. To distinguish between the leading and following portions of the sunspot groups, they first computed the mass centre. The portion to the east of the mass centre was defined as the leading portion and the portion to the west as the following. This definition was applied to all sunspot groups since they had no magnetic information (Howard 1991). The tilt angle of a sunspot group,  $\alpha$ , is defined as  $\tan \alpha = \Delta\phi / [\Delta l \cos \phi]$ , where  $\phi$  is the latitude of the centre of the sunspot group and  $\Delta\phi$  and  $\Delta l$  are the differences in latitude and central meridian position between the centre of gravity of the leading and following portions of the group, respectively.

The final data set includes dates of observations, positions, area and number of individual sunspots for each sunspot group and for its leading and following portions, as well as the tilt angle. A description of the calculation of the tilt angles can be found in the paper by Howard (1991). The white light images from Kodaikanal observatory were treated using the same techniques and procedures by Sivaraman et al. (1993).

In the present study we also use the sunspot area data set compiled by Balmaceda et al. (2009) using observations from a number of different observatories that were carefully cross-calibrated in order to reduce, as much as possible, systematic and other differences between observations at different sites as well as the number of data gaps. The combined data set goes back to 1874.

### 2.3.2 Data evaluation

The first inspection of the MW and KK data revealed a great number of zero values for the tilt angles ( $\sim 22\%$  in MW and  $\sim 30\%$  in KK). Therefore, we checked whether all zeros are real or just missing values. We assumed that the tilt angle can only be determined if the

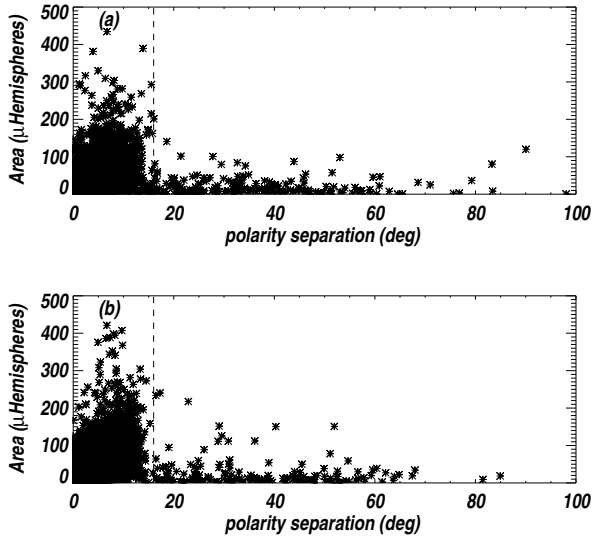


Figure 2.1: Area versus polarity separation between the leading and following portions of a sunspot group for (a) Mount Wilson and (b) Kodaikanal data sets. The dashed line corresponds to  $16^\circ$ .

leading and following portions of a group have at least one spot each. Thus we neglected the zero tilt angle values in all cases when either portion of a group contained no spots. By applying this criterion, we found only one real measurement of a tilt of exactly zero degrees in the MW data set and none in the KK data set. The rest of the zero values only mark that it was not possible to measure the tilt angles for some reason. In order to accept a tabulated tilt angle as valid, we also required that the distance between the leading and following portions is less than  $16^\circ$ . This is justified by the distribution of sunspot group areas with polarity separation (see Fig. 2.1). Most of the groups lie in a range between 0 – 350 microhemispheres in area and  $0^\circ$  –  $16^\circ$  in polarity separation. Only around 0.6% and 0.4% of all the groups in the MW and KK data sets, respectively, present a polarity separation bigger than  $16^\circ$ . Of these, most have areas below 70 microhemispheres and are thus most likely typos since their total area is small and at such polarity separations it is most improbable that the two polarities belong to the same group. All together, i.e. based on both criteria, we have rejected 22.5% of MW groups and 30.6% of KK ones.

In our analysis we considered mainly cycle averages to study the variation of the tilt angles from cycle to cycle. The values of these averages are not greatly affected by gaps in the measurements if these are distributed homogeneously throughout each cycle. If, however, gaps are, for example, dominantly found in the ascending phase of a solar cycle the mean value of the tilt angle for that cycle will be lower than the real value. This is a

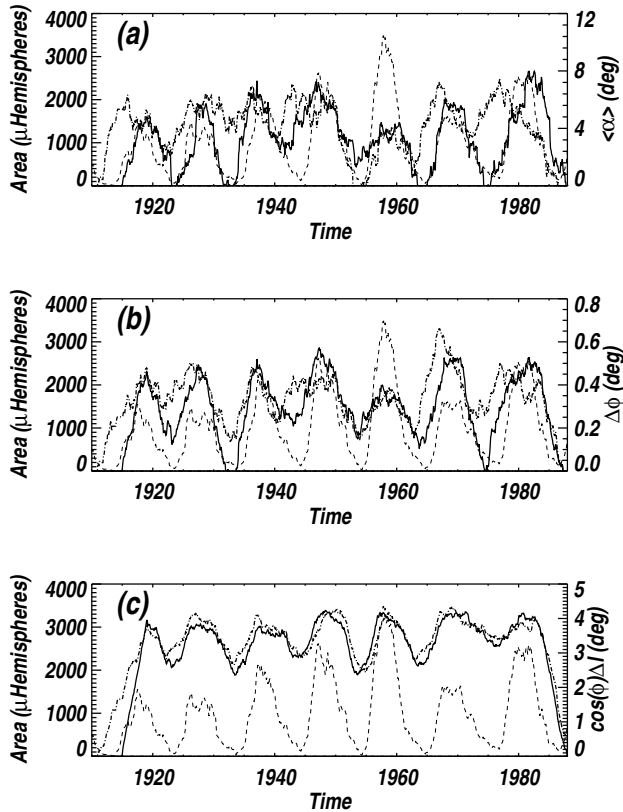


Figure 2.2: In all panels: Dashed thin line and left-hand Y-axes show the monthly means of the sunspot area from Balmaceda et al. (2009) vs. time; the solid and the dot-dashed thick lines represent Mount Wilson and Kodaikanal data, respectively. (a) Monthly area-weighted means of sunspot tilt angle smoothed over 4 years (right-hand Y-axis), (b) area-weighted latitude separation (right-hand Y-axis) and (c) area-weighted longitude separation of leading and following parts of sunspot groups (right-hand Y-axis).

direct consequence of the butterfly diagram (spots at the beginning of a cycle appear at higher latitudes) and Joy's law (tilt angles are higher for sunspot groups located at higher latitudes). Unfortunately it is not possible to distinguish between spotless days and gaps in the data sets of MW and KK observatories. We find that no spots were present or no observations were made on  $\sim 60\%$  and  $\sim 55\%$  of all days in the MW and KK data sets respectively. In fact most of them are located within solar activity minima, which

is reasonable because the number of truly spotless days is largest at minimum activity. It was possible to determine the spotless days by comparing the MW and KK data sets with a more complete daily sunspot data set from Balmaceda et al. (2009). In this data set, where it is possible to distinguish between gaps and spotless days, only 6.5% of the data are missing due to gaps in the considered period. After the comparison we retrieved a  $\sim 59\%$  and a  $\sim 56\%$  of truly missing dates in MW and KK data sets respectively. These remaining gaps seem on average to be more or less randomly distributed over cycle phases. They should not significantly affect the averages over a cycle. However the gaps do affect the calculation of the cycle length and strength. In our work we use the length as defined and calculated by the National Geophysical Data Centre (see Section 2.4.2). In the case of the strength, we used the daily sunspot area data set from Balmaceda et al. (2009) due to its low percent of gaps. To avoid systematic errors, we linearly interpolated across the sunspot area data gaps.

Next we consider another possible source of bias. Since during a strong cycle more spots are found on the Sun's surface the grouping criterion by Howard ( $3^\circ$  wide in latitude and  $5^\circ$  wide in longitude) could lead to an erroneous grouping for such cycles, because spots that do not belong to the group, but rather to a nearby neighbouring region, could be included. We expect such misclassification to occur mainly in the longitudinal direction due to the asymmetry of the box. It would lead to an enhancement of the longitudinal separation between the following and leading portions of the sunspot groups ( $\Delta l \cos \phi$ ) for the strongest cycles. Such a spuriously increased longitude separation would lead to a reduced average tilt. Figure 2.2 (a) shows the time series of monthly means of sunspot group tilt angles weighted by their corresponding sunspot group areas (see right-hand Y-axis) for both MW (solid line) and KK (dot-dashed line) records. A smoothing of 4 years was necessary due to the high noise the data presented.

The mean area-weighted tilt angles are calculated as follows:

$$\langle \alpha_\omega \rangle = \frac{\sum A_j \alpha_j}{\sum A_j},$$

where  $A_j$  and  $\alpha_j$  are the area and the tilt angle of the sunspot group  $j$ , respectively. In the case of monthly means, the sum goes over all sunspot groups in one month, while in the case of cycle means, the sum goes over all sunspot groups present during one cycle. Also plotted are monthly means of sunspot area (dashed line and left-hand Y-axes) from Balmaceda et al. (2009). Cycle 19 is clearly the strongest and has, at the same time, the lowest values of the tilt angles of the 7 analysed cycles. We test in Fig. 2.2 (b) and (c) the possibility of a systematic error. Here we plot monthly means of sunspot latitude ( $\Delta \phi$ ) and longitude ( $\Delta l \cos \phi$ ) separations between the leading and following portions of sunspot groups. The solid line is again used for the data from MW observatory and the dot-dashed line for KK observatory. The drop in  $\Delta \phi$  during cycle 19 indicates that the low values of the tilt angles during this period are due to a lower latitudinal separation of both polarities while the fact that cycle 19 is not conspicuous in Fig. 2.2 (c) indicates that its low tilt angles are not due to a larger longitudinal separation. This result does not exclude that the grouping algorithm might have combined together sunspots that with magnetic information would have been grouped differently. In any case we believe that, if there is a systematic error in the tilt angles, this is not seen in the latitude and longitude positions of the leading and following portions of sunspot groups.

### 2.3.3 Joy's law

The tilt angle dependence on the latitude was first found by Joy in 1919 (Hale et al. 1919) and later confirmed by other authors (Howard 1991, Wang and Sheeley 1991, Sivaraman et al. 1999). It provides strong constraints on the magnetic field strength of the flux tubes in the tachocline, which emerge to form the observed active regions (D'Silva and Choudhuri 1993, Schüssler et al. 1994). This relation shows a positive trend: the tilt angles are larger for sunspots at higher latitudes. We have used data from MW and KK observatories in order to rederive this relationship as a test. In Fig. 2.3, the tilt angles averaged over the complete data sets for latitude bins of  $5^\circ$  are plotted versus latitude. MW data are represented by asterisks connected by the dashed line and KK observations by open circles connected by the solid line. The results for both data sets are in agreement with each other within  $1 - 2\sigma$  and are very close to the results obtained by Sivaraman et al. (1999), with the mean difference between our points and theirs being  $|\Delta| \sim 0.1^\circ$  and  $|\Delta| \sim 0.2^\circ$  for MW and KK, respectively. These differences are most probably due to different selection criteria applied to the data.

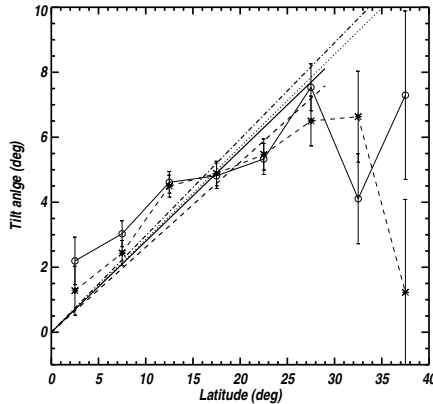


Figure 2.3: Mean tilt angle for bins of 5 degrees latitude vs. latitude for MW (asterisks connected by the dashed line) and KK (open circles connected by the solid line). The error bars represent  $\pm 1$  standard error. The thick dashed and solid lines are linear fits forced to pass through the origin to the MW and KK data, respectively. The dotted and dot-dashed lines correspond to lines where the slope has been taken as the ratio of tilt with latitude (see description in the text) for the MW and KK data respectively.

We have also obtained linear fits to the data points excluding the last two bins since the number of groups in these is very low compared to the other bins (about 2% and 0.5% of the total) and the errors are higher by a factor of  $\geq 2$ . The fits are forced to pass through the origin since we expect no tilt for sunspot groups at the equator. The values for the fits are:

$$\alpha = (0.26 \pm 0.05)\lambda$$

and

$$\alpha = (0.28 \pm 0.06)\lambda$$

for MW and KK data, respectively, where  $\alpha$  represents the tilt angle (in degrees) and  $\lambda$  the latitude (in degrees). The correlation coefficient of the regression lines are  $r^2 = 0.85$  for the MW data and  $r^2 = 0.76$  for the KK data. The linear fits are shown in Fig. 2.3, where the thick dashed line is for the MW fit and the thick solid line for the KK fit. Fitting the data points while taking into account that each point has a different value for the standard deviation gives the same result for the slope up to the third decimal. Also plotted are the lines  $\alpha = M\lambda$  where  $M$  is calculated as  $M = \Sigma_j \alpha_j / \Sigma_j \lambda_j$  and  $\alpha_j$  and  $\lambda_j$  correspond to the tilt angle and latitude of sunspot group  $j$ . The dotted line represents the MW data with a slope of  $M = 0.29$  and the dot-dashed line the KK data with a slope of  $M = 0.30$ . This is shown as comparison since it is not affected by the fact that each bin contains a different number of points.

The slopes found here are lower than those obtained by Wang and Sheeley (1989, 1991) from daily magnetograms for cycle 21 ( $\text{siny} = 0.48 \cos \theta + 0.03$  where  $\gamma$  is the tilt angle and  $\theta$  the colatitude). However, our values for the slope, 0.26 and 0.28, are closer to the 0.15 value deduced by Schüssler and Baumann (2006) who used a flux-transport model to fit data from MW and Wilcox Solar observatories of the total photospheric field. The difference to the results of Wang and Sheeley (1989, 1991) could have a variety of causes, such as the different types of data considered (spots vs. magnetograms), differences in spatial resolution (cf. Howard et al. 1984, Wang and Sheeley 1989) combined with the dependence of tilt angle on the size of a region (D’Silva and Howard 1993, Howard 1993), or the fact that they considered a single cycle. Our results for the slope of the regression line show considerable scatter from cycle to cycle, even to the extent that we do not consider the values obtained for individual cycles to be particularly reliable (see Sect. 2.4.1).

## 2.4 Results

### 2.4.1 Average value of tilt angles

It was first pointed out by Howard (1991) that the average tilt angle of all sunspot groups during the period 1917 – 1985 deduced from MW data was  $4.2^\circ \pm 0.2^\circ$ . For the whole MW data set period (1917 – 1985) we obtained a value of  $4.25^\circ \pm 0.18^\circ$ , in excellent agreement with Howard (1991), while for the whole KK data set (1906 – 1987), we deduced  $4.51^\circ \pm 0.18^\circ$ .

Next we treat MW and KK data on a cycle-by-cycle basis, obtaining a different value of the average sunspot tilt angle for each cycle. Figure 2.2 (a) displays monthly area-weighted means of sunspot tilt angles smoothed over 4 years through cycles 15 to 21 for the MW and KK data sets. Table 2.1 gives area-weighted cycle averages and  $1\sigma$  standard error. Note that cycles 15 and 21 are not complete in the MW data set, as discussed in Sect. 2.3.1, and thus the value of the mean tilt angle for cycle 15 might be underestimated and the value for cycle 21 overestimated, according to the combination of Maunder’s butterfly diagram and Joy’s law. The low value of the sunspot tilt angles for cycle 19, as

Table 2.1: Area-weighted mean tilt angles in degrees for each cycle for MW and KK records.

Cycle	MW $\pm 1\sigma$	KK $\pm 1\sigma$
15	5.69 $\pm$ 0.57	5.00 $\pm$ 0.50
16	5.08 $\pm$ 0.46	5.91 $\pm$ 0.43
17	5.83 $\pm$ 0.42	6.41 $\pm$ 0.41
18	5.69 $\pm$ 0.35	4.97 $\pm$ 0.38
19	3.84 $\pm$ 0.33	4.59 $\pm$ 0.38
20	4.63 $\pm$ 0.38	5.73 $\pm$ 0.36
21	5.30 $\pm$ 0.40	5.37 $\pm$ 0.42

compared to the other cycles, indicated by Fig. 2.2 (a), is also seen in the cycle averaged values.

In addition to the average tilt angles, we also attempted to determine Joy’s law per cycle in the same manner as done in Sect. 2.3.3. However, the scatter of the individual values of the mean tilt angle per  $5^\circ$  latitude bins turn out to be too large. The correlation coefficient for a linear regression to the points are for some cycles as low as  $r^2 = 0.17$  for MW and  $r^2 = 0.026$  for KK. Also, the errors in the calculated slopes are comparable to or slightly bigger than the difference between these values from MW to KK data sets. Therefore, no clear difference could be determined between the slopes of Joy’s law from cycle to cycle.

## 2.4.2 Cycle parameter definitions

For the parameter study we focus on three main characteristics of a solar cycle: strength, amplitude, and length. Strength is defined as the total surface area covered by sunspots throughout a given solar cycle. We calculate it from the daily sunspot area data set compiled by Balmaceda et al. (2009) as the integral of sunspot area over the duration of each cycle. This record is used since it has significantly fewer data gaps than the MW and KK data sets, as discussed in Sect. 2.3.2. The cycle amplitude is the highest value of monthly averaged sunspot number and the length is the period of time between two consecutive minima. Times of solar activity minimum, amplitudes, and the lengths of cycles are taken from the National Geophysical Data Centre<sup>1</sup>.

We looked for possible relationships of these parameters with four different quantities based on the tilt angles: cycle mean tilt angle,  $\langle\alpha\rangle$ , cycle mean tilt angle normalised by the mean latitude of sunspots during that cycle,  $\langle\alpha\rangle/\langle\lambda\rangle$ , cycle mean area-weighted tilt angle,  $\langle\alpha_\omega\rangle$ , and the cycle mean area-weighted tilt angle normalised by the mean latitude of sunspots during the same cycle,  $\langle\alpha_\omega\rangle/\langle\lambda\rangle$ . (For a brief discussion of how these choices are influenced by the scatter in the tilt angles see Appendix A). The area-weighted tilt angles are used to give more importance to the bigger groups, which exhibit less scatter, and the normalised tilt angles are considered in order to remove the effect of the latitudinal dependence (Joy’s law) on the cycle-averaged (area-weighted) tilt angles. Note that for the MW data set, cycles 15 and 21 are not taken into account in the relationships concerning

<sup>1</sup><http://www.ngdc.noaa.gov/stp/SOLAR/getdata.html>

$\langle\alpha\rangle$  and  $\langle\alpha_w\rangle$  due to their incompleteness and could be thus biased by Joy's law. This is not the case for the quantities  $\langle\alpha\rangle/\langle\lambda\rangle$  and  $\langle\alpha_w\rangle/\langle\lambda\rangle$  since normalising by the mean latitude removes this source of bias. Sunspots in stronger cycles lie at higher latitudes (Solanki et al. 2008), so that simply due to Joy's law these cycles would have larger mean tilt angles. Dividing by the mean latitude largely removes this difference (both, Joy's law and the dependence of mean latitude on cycle strength are linear), so that  $\langle\alpha\rangle/\langle\lambda\rangle$  and  $\langle\alpha_w\rangle/\langle\lambda\rangle$  indicate intrinsic changes of Joy's law from cycle to cycle.

### 2.4.3 Relationships within the same cycle

We first investigate the possible relationship of the cycle averaged sunspot tilt angles with the three solar cycle parameters of the *same* cycle. These relations may help to shed light on the underlying magnetic flux tubes at the base of the convection zone and the processes that affect them on their way to the surface (in the case of the strength and amplitude of the cycle) and on the possibility that the tilt angles of active regions are involved, along with other features (e.g. meridional flow), in the regulation of the cycle period of the dynamo (in the case of length), or conversely are influenced by it.

We calculated linear correlation coefficients between the 3 solar cycle global parameters and the 4 quantities based on the tilt angles (see Sect. 2.4.2). Due to the low number of cycles, we also determined the probability that the correlations are due to chance ( $P$ ). These are calculated from the probability density function of the student's t-distribution, which depends both on the correlation coefficient and the number of points in the sample. All the values are listed in Table 2.2 for MW and KK data. Table 2.2 suggests that both the strength and the amplitude of a cycle show a significant negative correlation with the average tilt of the same cycle,  $\langle\alpha\rangle$ , for at least KK data. For MW data, the probabilities that the correlations are due to chance,  $P$ , are about 30%, but for KK data (that includes both cycles 15 and 21), the corresponding probabilities are lower than 10%. These correlations are significantly strengthened once we eliminate the enhanced effect of Joy's law on cycles with sunspots on average at higher latitudes by considering  $\langle\alpha\rangle/\langle\lambda\rangle$ . The probabilities then fall to values below 2% for both MW and KK data sets. For the area-weighted tilt angles, the correlation coefficients are weaker. Although these are also strengthened after the normalisation by  $\langle\lambda\rangle$ , reaching probability values below 3%, they remain slightly higher than for  $\langle\alpha\rangle/\langle\lambda\rangle$ . The correlations between the length and the 4 tilt angle based parameters are in general low, of low confidence and inconsistent in sign between the two data sets.

Figure 2.4 shows  $\langle\alpha_i\rangle/\langle\lambda_i\rangle$  versus  $S_i$ , where  $i$  is the cycle number. The dashed line represents a linear fit to the points and the error bars correspond to  $1\sigma$  errors calculated by means of error propagation, where the errors for the mean tilt angle and the mean latitude correspond to their standard error. The error bars have been calculated assuming Gaussian statistics and are thus overestimated. In MW data (Fig. 2.4 (a)) cycles 15 and 21 are represented by squares and dashed lines for the error bars to denote their incompleteness. Note that all data points lie roughly within  $1\sigma$  of the regression lines. This suggests that given the accuracy of the measured tilt angles (given largely by the scatter shown by active regions) the obtained correlation coefficients are near the maximum value achievable for data with such large uncertainty.

Table 2.2: Correlation coefficients between the 4 quantities based on the tilt angle and the strength ( $S$ ), amplitude ( $A$ ) and length ( $L$ ) of the same cycle.

Parameter	Mount Wilson						Kodaikanal					
	$r_c$	$P$	$r_c$	$A$	$P$	$L$	$r_c$	$P$	$r_c$	$A$	$P$	$L$
$\langle \alpha \rangle$	-0.59	0.30	-0.60	0.28	0.64	-0.29	0.64	-0.77	0.04	-0.69	0.09	-0.58
$\langle \alpha_{\omega} \rangle$	-0.48	0.41	-0.48	0.41	0.44	-0.46	0.44	-0.46	0.30	-0.66	0.11	0.19
$\langle \alpha \rangle / \langle \lambda \rangle$	-0.95	$1 \times 10^{-3}$	-0.83	0.02	0.37	-0.40	0.37	-0.93	$2 \times 10^{-3}$	-0.82	0.02	-0.48
$\langle \alpha_{\omega} \rangle / \langle \lambda \rangle$	-0.81	0.03	-0.91	$4 \times 10^{-3}$	0.86	0.08	0.86	-0.80	0.03	-0.91	$4 \times 10^{-3}$	0.03

Correlation coefficients are represented by  $r_c$  and the probability that the correlation is due to chance by  $P$  for both the MW and KK data sets.

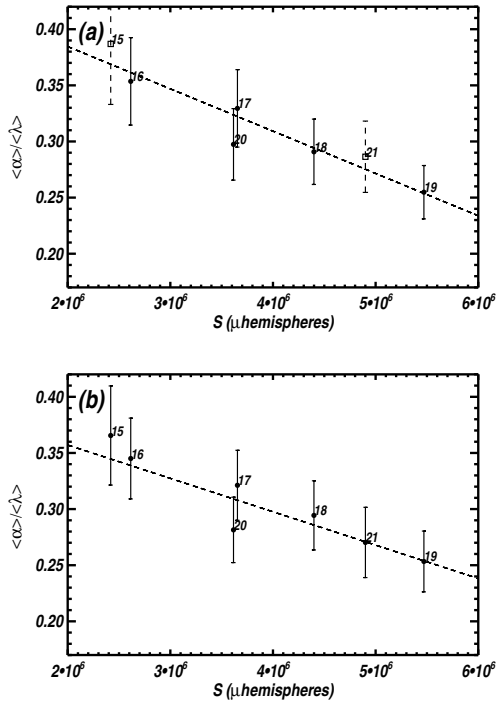


Figure 2.4: Cycle averaged tilt angle normalised by the emergence latitude vs. strength of the same cycle. The error bars represent  $1\sigma$  errors and the dashed line is a linear fit to the points. Panel (a) displays the results based on MW data ( $r_c = -0.95$ ), where cycles 15 and 21 are shown as squares and dashed lines for the error bars, and panel (b) on the KK data set ( $r_c = -0.93$ ).

## 2.4.4 Relationships with the following cycle

Prediction of future solar activity is important not only for space weather and climate, but also to test current dynamo models. In this section we investigate how the cycle averaged tilt angles are related to the global parameters of the *next* cycle. We calculated the correlation coefficients between the tilt-angle parameters  $\langle\alpha\rangle$ ,  $\langle\alpha\rangle/\langle\lambda\rangle$ ,  $\langle\alpha_\omega\rangle$  and  $\langle\alpha_\omega\rangle/\langle\lambda\rangle$  of cycle  $i$  and the parameters  $S$ ,  $A$  and  $L$  of cycle  $i + 1$  and the probability that these correlations are due to chance.

In general the correlations of the strength and amplitude with the 4 tilt angle based

Table 2.3: Correlation coefficients between the 4 quantities based on the tilt angle and the strength ( $S_{i+1}$ ), amplitude ( $A_{i+1}$ ) and length ( $L_{i+1}$ ) of the *next* cycle

Parameter	Mount Wilson				Kodaikanal							
	$S_{i+1}$	$A_{i+1}$	$L_{i+1}$	$P$	$S_{i+1}$	$A_{i+1}$	$L_{i+1}$	$P$				
$\langle \alpha \rangle_i$	0.40	0.50	0.47	0.42	-0.88	0.05	-0.58	0.17	-0.52	0.23	-0.32	0.48
$\langle \alpha_\omega \rangle_i$	0.54	0.35	0.63	0.25	-0.77	0.13	0.19	0.68	0.18	0.70	-0.57	0.18
$\langle \langle \alpha \rangle / \langle \lambda \rangle \rangle_i$	-0.57	0.18	-0.52	0.23	-0.46	0.30	-0.52	0.23	-0.47	0.29	-0.37	0.41
$\langle \langle \alpha_\omega \rangle / \langle \lambda \rangle \rangle_i$	-0.07	0.88	-0.06	0.99	-0.67	0.10	-0.007	0.99	0.003	0.99	-0.61	0.15

Correlation coefficients are represented by  $r_c$  and the probability that the correlation is due to chance by  $P$  for both the MW and KK data sets.

quantities are low and inconsistent between the two data sets. Only correlations between  $(\langle\alpha_w\rangle/\langle\lambda\rangle)$ , and  $L_{i+1}$  appear to be statistically significant for both data sets. Table 2.3 lists the correlations found between the tilt angle based parameters and the length of the next cycle. For MW data, the probabilities that the correlations are due to chance are below or around 10% for all the averages considered except for  $\langle\alpha\rangle/\langle\lambda\rangle$ . The strongest correlation found is with the mean tilt angle  $(\langle\alpha\rangle)$  of value  $r_c = -0.88$ . In contrast, for KK data only  $\langle\alpha_w\rangle/\langle\lambda\rangle$  presents a correlation ( $r_c = -0.61$ ) with a chance probability below 15%. This suggests that if the tilt angles are large, then the next cycle will be short. The fact that the correlation of tilt with the length of the next cycle is significant, but is poor with the strength of the next cycle is consistent with the finding that the length and strength of a cycle are poorly correlated ( $r_c = -0.37$ , Charbonneau and Dikpati 2000 and  $r_c = -0.35$ , Solanki et al. 2002a)

Now, tilt angles influence the amount of magnetic flux reaching the poles (Baumann et al. 2004) and the polar magnetic flux during activity minimum has been found to be one of the proxies that best predicts the strength of the next cycle (Makarov et al. 1989, Dikpati et al. 2008). However, the tilt angle is not the only parameter influencing the polar flux, which is in line with the poor correlation found between tilt angles and the strength of the following cycle (values range from 0.40 to 0.54 for MW and  $-0.58$  to 0.19 for KK and are not even consistent in sign between the two data sets). Obviously, the total amount of magnetic flux emerging over a cycle,  $\phi_{tot}$ , is another central parameter influencing the polar flux (Baumann et al. 2004). Hence a more physically motivated quantity to consider is  $\phi_{tot}\langle\alpha\rangle/\langle\lambda\rangle$  or  $\phi_{tot}\langle\alpha_w\rangle/\langle\lambda\rangle$ . Since no regular and consistent magnetic information is available prior to cycle 20 we use sunspot areas as proxies of  $\phi_{tot}$ . I.e. instead of  $\phi_{tot}\langle\alpha\rangle/\langle\lambda\rangle$  we determine  $S\langle\alpha\rangle/\langle\lambda\rangle$ . Sunspot areas are proportional to the amount of magnetic flux emerging through the spots since the field strength averaged over a sunspot is similar (Solanki and Schmidt 1993).

Figure 2.5 shows  $(S\langle\alpha_w\rangle/\langle\lambda\rangle)_i$  versus  $S_{i+1}$ . Again the errors are treated by means of error propagation and assuming Gaussian statistics and are thus overestimated. In this case we were not able to propagate the errors precisely since we have no information on the errors of the individual measured sunspot areas that would affect the calculation of  $S_i$  or  $S_{i+1}$ . The error bars in Fig. 2.5 are calculated assuming that  $S_i$  is known accurately. Using  $S$  instead of  $\phi_{tot}$  also means that we implicitly assume that the ratio of magnetic flux in faculae and network to that in sunspots is the same for each cycle. Consequently, the plotted  $1\sigma$  error bars represent lower limits to the true uncertainties. Both data sets show a moderate positive correlation between  $(S\langle\alpha_w\rangle/\langle\lambda\rangle)_i$  and  $S_{i+1}$  (see upper row of Table 4 for  $r_c$  and  $P$  values). It is interesting to point out that both data sets, although independent, display almost identical fits:  $y_i = 0.20S_{i+1} + 495066.6$  and  $y_i = 0.20S_{i+1} + 535359.8$  for MW and KK data sets respectively, where  $y = S\langle\alpha_w\rangle/\langle\lambda\rangle$ .

Finally, we carry out a variant of the above analysis that is guided by dynamo models that include the influence of the meridional circulation at the solar surface (Wang and Sheeley 1991, Choudhuri et al. 1995). According to such models the amount of flux reaching the poles depends (for a fixed differential rotation, meridional circulation and diffusion rate) on the tilt angles and the latitude distribution of the active regions. If a region is at relatively high latitude, then in general both polarities are dragged to the pole by meridional circulation, leading to a negligible change in the magnetic flux there. For active regions close to the equator the magnetic flux of the leading portion can reach

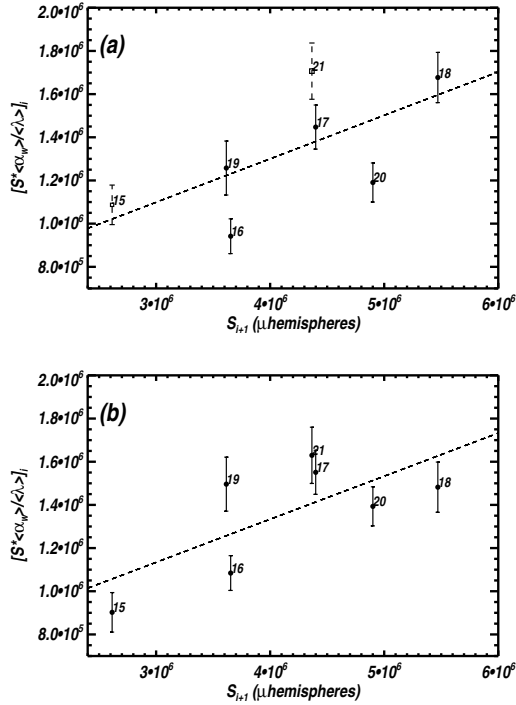


Figure 2.5: Strength of cycle multiplied by normalised mean area-weighted tilt angle vs. the strength of the next cycle for (a) MW data ( $r_c = 0.65$ ) and (b) KK data ( $r_c = 0.70$ ). The dashed lines are linear fits to the data points and the error bars represent  $1\sigma$  error (assuming Gaussian statistics). For the MW data set cycles 15 and 21 are shown as squares and dashed lines for the error bars to indicate their incompleteness.

and cancel the opposite polarity of the leading portion of an active region in the other hemisphere. This leads to an imbalance in the sense that mainly flux from the following polarity reaches the pole. Hence regions at low latitudes contribute disproportionately to the reversal and accumulation of magnetic field in the poles. This is thought to affect the strength of the next cycle since the polar fields are the input for the next cycle. We take into account this latitude dependence by multiplying an exponential function of the latitude to the area-weighted tilt angles. The monthly means of area- and latitude- weighted tilt angles are computed as follows:

$$\overline{\alpha_{a,\lambda}} = \frac{\sum A_j \alpha_j e^{-\frac{|\lambda_j|}{\lambda_0}}}{\sum A_j},$$

where  $A_j$  is the area of the sunspot group  $j$  from MW and KK data sets,  $\alpha_j$  the tilt an-

gle of the same group,  $\lambda_j$  its latitude and  $\lambda_0$  is a constant that determines how rapidly the exponential function drops with latitude. The value of  $\lambda_0$  depends on the latitudinal velocity profile of the meridional flow, which (for reasons of symmetry) is zero at the equator. Small values of  $\lambda_0$  correspond to a meridional flow whose horizontal component increases rapidly with  $\lambda$ . In the absence of clear observational constraints we have set  $\lambda_0$  to  $10^\circ$ ,  $20^\circ$  and  $30^\circ$  and have repeated the analysis for each of these values.

In Fig. 2.6 we plot  $\overline{S\overline{\alpha_{a,\lambda}}}$  (solid curve) for the whole time series smoothed over 24 months, with  $\overline{S}$  being the monthly means of sunspot area from Balmaceda et al. (2009). The dashed curve is the 12 month smoothed  $\overline{S}$  and the solid curve has been shifted by +11 years to better compare  $\overline{S\overline{\alpha_{a,\lambda}}}$  with  $\overline{S}$  of the following cycle. Since the whole curve has been shifted by a constant value and each cycle has a different duration, the lengths of the cycles of the solid and dashed curves do not match. However, it is seen that the consecutive rise in strength from cycles 16 to 19 and the drop from cycle 19 to 20 are reproduced. The correlation coefficients between the peaks of both curves reach a maximum value of 0.79 ( $P=3\%$ ) for MW and 0.78 ( $P=4\%$ ) for KK when taking  $\lambda_0 = 10^\circ$  (see lower row of Table 2.4). All of the 7 cycles are considered in both data sets since the maxima of cycles 15 and 21 are included in the MW record. The correlation coefficient values range from 0.74 to 0.79 for the MW data set and 0.78 to 0.79 for the KK data set when smoothing over 24, 36 and 48 months. Since the first 4 years of cycle 15 are not complete in the MW data set, we chose a 24 month smoothing as optimal to reduce the noise while not losing the maximum of cycle 15.

Table 2.4: Correlation coefficients between expressions containing  $\alpha$  of cycle  $i$  and the strength or maximum amplitude of cycle  $i + 1$ .

	Mount Wilson		Kodaikanal	
	$r_c$	$P$	$r_c$	$P$
$(\overline{\langle \alpha_{w,s} \rangle} S)_i$ vs. $S_{i+1}$	0.65	0.11	0.70	0.08
$\max(\overline{S\overline{\alpha_{a,\lambda}}}) + 11\text{yrs}$ vs. $\max(\overline{S})$	0.79	0.03	0.78	0.04

Correlation coefficients are represented by  $r_c$  and the probability that the correlation is due to chance by  $P$  for both the MW and KK data sets. The two rows correspond to different expressions explained in the main text.

## 2.5 Discussion

Our understanding of the solar dynamo remains incomplete despite the large amount of effort invested into it (Charbonneau 2005). One hindrance to a better understanding is the limited number of observational constraints, some of which are reviewed by Gilman (1986, 2002) and Rempel (2008).

In this paper we have analysed the time-dependence of the tilt angle, which has added two more observational constraints that dynamo models must satisfy. The first is that there is an inverse correlation between the strength of a cycle and the tilt angle ( $\alpha$ ) of

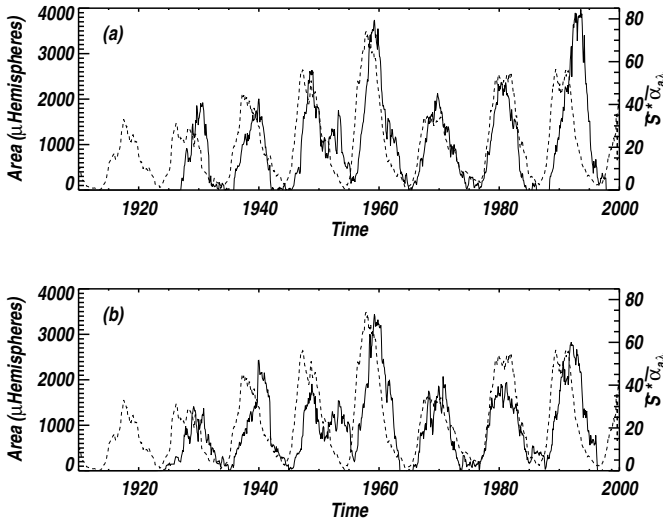


Figure 2.6: Comparison of actual and predicted sunspot area. The dashed curve shows monthly sunspot areas smoothed over 12 months from Balmaceda et al. (2009). The solid curve is the prediction based on the tilt angles and sunspot areas of the previous cycle for (a) MW and (b) KK records, both smoothed over 24 months.

sunspot groups observed during that cycle. This correlation was found to increase when the latitudinal dependence of Joy's law was taken into account (that is when  $\alpha/\lambda$  was considered instead of  $\alpha$ ).

The results in the previous section are based on observations. While this paper concentrates on the observational signature, it is worthwhile to digress and speculate on the possible causes of this inverse correlation. In doing so we emphasise that our discussion is only speculative whereas the results of the previous section are based firmly in the observational data sets. One possibility is that the field strength of magnetic flux tubes in the overshoot region below the convection zone is larger during strong cycles. Since stronger flux tubes are less affected by the Coriolis force this would explain the observed correlation. In Babcock-Leighton type dynamos the toroidal flux tubes at the base of the convection zone are believed to be the result of the differential rotation winding up the poloidal magnetic field. The magnetic energy density of the loops formed in this way is likely to be limited to equipartition values with the kinetic energy density of the differential rotation. This gives a magnetic field strength of  $\approx 10^4$  G. Such a loop can then lose mass via an instability which drains mass from the slightly sub-adiabatic region where the flux tube is located into the convection zone, which increases the field strength to  $\approx 10^5$  G over a timespan of approximately 6 months (Rempel and Schüssler 2001). As the flux tube becomes stronger, it becomes subject to the Parker instability which causes it to erupt

to the surface. The Parker instability depends on both the field strength and on the sub-adiabaticity of the layer where the flux tubes are stored: magnetic fields of tubes that are stored slightly deeper can become stronger prior to the onset of the Parker instability.

To explain the observations requires either that in strong cycles the tubes are produced or stored slightly deeper (Caligari et al. 1995), or the region where the flux tubes are stored becomes slightly more stable, or that the intensification process acts more quickly so that higher field strengths can be reached before the tubes erupt. A combination of these processes may also be at work.

There are a number of nonlinear, competing, factors which are likely to be relevant. For example the increased flux of a strong cycle will be more resistant to downward pumping, and will perhaps decrease the depth of the convective overshooting at the base of the convection zone. This might decrease the depth at which the flux is located, but will also affect the thermodynamic properties of the layer. Another effect, which acts in the correct direction, is the magnetic tension associated with the enhanced poloidal flux of strong cycles. This will tend to pull the field lines deeper into the overshoot region, however the effect is likely to be weak, possibly depending on how the poloidal field is structured.

In relation to changing the subadiabaticity, Rempel and Schüssler (2001) have argued that the energy to intensify the toroidal flux tubes to  $10^5$  G comes from moving material along the entropy gradient near where the tubes are stored. The amount of energy involved has been estimated (e.g. Steiner 2004) to be approximately  $10^{40}$  ergs. On the observational side, Baldner and Basu (2008) reported a  $10^{-2}\%$  change in the wave speed squared near the base of the convection zone. The observed change is small and anticorrelated with activity. Its effect in the current context is to change the subadiabaticity – enhancing the stability in the region where the flux tubes are stored. How strong the effect would be, and how it balances with other effects, needs to be evaluated.

Another possibility is that the observed tilt angles have been influenced by the near-surface flows. These inflows consist of a time-dependent component of the solar differential rotation (Howard and Labonte 1980) called zonal flows, and a time-dependent component in the meridional plane which has been observed by tracking magnetic features (Komm et al. 1993) and with helioseismology (Basu and Antia 2003). Some models suggest that both components of the inflow are driven by the excess cooling associated with plage (Spruit 2003, Rempel 2006). If so, the strength of the inflow will be determined by the amount of plage, which is directly related to the strength of the current cycle.

Both components of the inflows will tend to decrease the tilt angle over time. This effect acts on the flux tube both as it rises through the inflow and as it evolves on the surface after emergence. The sign of this effect is correct, enhanced inflows during strong cycles will reduce the observed tilt angles. To estimate the magnitude of the effect we now concentrate on the meridional component of the inflow (the effect of the time variations of the zonal flows turns out to have a similar magnitude).

The time dependent meridional flow includes an inflow towards the active region belts (Zhao and Kosovichev 2004) which had an amplitude of  $\pm 5$  m/s for cycle 23. To estimate the expected magnitude of the effect on the tilt angle, we assume that sunspots are, on average, subject to this flow for  $\approx 5$  days before they are observed. These 5 days include the rise time through the flow, the sunspot formation time as well as a delay caused by the fact that not all sunspots appear on the side of the Sun facing the Earth. The maximum

relative velocity with which the two polarities could be driven towards one another by such a flow is 10 m/s. This maximum is unlikely to be reached, so for the purposes of obtaining a preliminary estimate we assume that they actually move towards each other with half this speed, that is 5 m/s. Over the course of the 5 days this gives a 2.16Mm decrease in the latitudinal separation of their leading and trailing fluxes. For an active region with a longitudinal separation between the leading and trailing fluxes of 100 Mm, this is a decrease in tilt angle of around 1.23 degrees. If we allow for the fact that cycle 19 was stronger than cycle 23, so that its inflows would have been stronger, then the magnitude of the effect is approximately consistent with the observations.

The above are not the only possibilities for the observed negative correlation, and have been presented only to give an indication of some of the different types of possibilities. It is possible that some of these explanations will be able to be excluded on either observational or theoretical grounds. More modelling and observations will be required to pinpoint the main mechanism.

The second result is that there is a reasonably strong correlation between the product of the strength of a cycle and its average tilt angle and the strength of the next cycle,  $r_c = 0.65$  and  $r_c = 0.70$  for the two data sets, respectively. This product was considered because it corresponds to the poloidal source term in dynamos based on the Babcock-Leighton idea. The correlations were found to improve when the quantities were made to more closely match the poloidal source term of the models. Specifically, we found an improvement when we included a latitudinal dependence designed to model the effectiveness of flux emergence in producing global poloidal fields (which depends upon some of the flux crossing the equator so that regions emerging close to the equator are more effective). This observational constraint supports the flux-transport dynamo model. It shows that the strength of a cycle is correlated at the 79% or 78% level (depending on the data set) with the poloidal flux of the previous cycle. Importantly, the drop in strength from cycle 19 to 20 is well reproduced. This tilt angle then appears to account for a substantial part of the variation from cycle to cycle of the activity level.

This is good news in two regards. Firstly, it suggests that, by measuring the tilt angle and amplitude of a cycle, we will be able to make early predictions of the strength of the proceeding cycle. The predictive accuracy is not higher than, for instance methods based on precursors (see Hathaway et al. 1999), but can be made much earlier. This can be seen in Figure 6 where the “predictions” have been shifted by eleven years (note that a two year smoothing has been performed which reduces the predictive horizon to 10 years). A possible improvement of predictive skill at later times might be possible by combining different schemes, but this will depend on how independent they are. Secondly, it suggests that a major part of the nonlinear cycle modulation is associated with the tilt angle. Several possible non-linearities were discussed above, such as the near-surface inflows, the depth at which the tubes are stored and the properties of the plasma near the base of the convection zone. More work is required to distinguish between these and other possibilities.

## 2.6 Conclusions

We have analysed the sunspot data from Mount Wilson (MW) and Kodaikanal (KK) observatories in order to study Joy's law, the variation of sunspot group tilt angles from cycle to cycle and the relationship of this variation with 3 solar cycle parameters: strength, amplitude, and length. The correlations found from the analysis are listed in Tables 2.1, 2.2, 2.3, and 2.4. From the analysis we highlight the following:

(1) A linear fit to Joy's law gives  $\alpha = (0.26 \pm 0.05)\lambda$  for the MW and  $\alpha = (0.28 \pm 0.06)\lambda$  for the KK data sets. Here  $\alpha$  is the tilt angle and  $\lambda$  the latitude, both expressed in degrees.

(2) The mean tilt angle changes from cycle to cycle (Fig. 2.2 (a) and Table 2.1). The range of values exceeds the uncertainties in the cycle-averaged tilt angles.

(3) A negative correlation between the normalised tilt angle, or  $\langle\alpha\rangle/\langle\lambda\rangle$ , and the strength of the same cycle is found ( $r_c = -0.95$  and  $r_c = -0.93$  for MW and KK data sets, respectively).

(4) We also find a negative correlation between the latitude normalised area-weighted tilt angle ( $\langle\alpha_w\rangle/\langle\lambda\rangle$ ) and the length of the next cycle ( $r_c = -0.67$  and  $r_c = -0.61$  for MW and KK data sets, respectively).

(5) Finally, we discovered a positive correlation between the strength of one cycle multiplied by its mean area- and latitude- weighted tilt angle,  $(S\langle\alpha_w\rangle/\langle\lambda\rangle)_i$ , and the strength of the *next* cycle,  $S_{i+1}$ , ( $r_c = 0.65$  and  $r_c = 0.70$  for MW and KK data sets, respectively). Higher correlation coefficients are obtained between a tilt-angle based expression obtained through guidance from Babcock-Leighton type dynamo models and the amplitude of the next cycle ( $r_c = 0.79$  and  $r_c = 0.78$  for MW and KK, respectively).

These results show the importance of the tilt angle of sunspot groups for both the prediction of solar activity and the understanding of the physics behind the solar dynamo.

# 3 Solar irradiance reconstructions from a Surface Flux Transport Model

## 3.1 Abstract

Solar irradiance is one of the important drivers of the Earth's global climate and its reconstructions are thus of crucial interest for climate studies. We assume that variations of total solar irradiance are due to changes in the solar surface magnetic flux. To describe the latter we employ a surface flux transport model, which produces daily full-disc magnetograms of the solar surface. These are then used as input data in a SATIRE-S (Spectral And Total Irradiance Reconstructions for the Satellite era) type model to reconstruct the total solar irradiance back to times when no magnetograms are available. In this chapter we present a reconstruction for cycles 21 – 23 to compare it with the PMOD composite of irradiance observations. There is a reasonable agreement between the reconstructed values and the observations for both short term and long term variations. However, the shapes of the cycles are not completely reproduced, in particular that of cycle 23. The reconstructions show slightly higher irradiance levels during the maxima of cycles 21 and 22, a lower minimum between cycles 22 and 23, and a general disagreement during the whole cycle 23. Fits for cycles 21 and 22 alone improve the results during these two cycles. To ameliorate the total solar irradiance reconstructions the next step will be to include the flux emerging from ephemeral regions or small bipolar regions (see Ch. 4), which are missing in the reconstructions presented in this chapter.

## 3.2 Introduction

Reconstructions of total solar irradiance (TSI) have been going on since the late 1980's, with the use of models based on proxies of solar activity (e.g. Foukal and Lean 1988, Lean 2000, Fligge et al. 2000, Wenzler et al. 2006). Most successful models assume that irradiance changes on time scales of days or longer are driven by the evolving magnetic features on the solar surface (Krivova et al. 2003, Wenzler et al. 2006, Ball et al. 2011). The brightness contrast of these features and the evolution of their surface coverage contributes to the changing TSI. Dark sunspots and bright faculae and network contribute respectively to decrease and enhance the amount of radiation emitted by the Sun (see Sect.1.3.2).

TSI models by Lean (2000) consider the contribution of sunspots and faculae separately to the total irradiance. The darkening due to sunspots is calculated using a semi-empirical brightness ratio between sunspots and quiet Sun, and observations of sunspot areas and sunspot number for the earlier periods. The intensity brightening due to faculae is obtained from MgII core-to-wing ratio. Models like the ones developed by Fligge et al. (2000) and Krivova et al. (2003) also treat separately the irradiance from each magnetic feature on the solar surface. However, they use the spatial information of the magnetic features from direct full-disc observations of the Sun. Continuum images provide the location and area of sunspots and the magnetograms the magnetic field intensity of faculae and network. The intensity brightness of sunspots, faculae and network is taken from time-independent model atmospheres (Unruh et al. 1999). The model atmospheres give the intensity of the corresponding magnetic feature dependent on the wavelength and the position on the solar disc. The down side of this type of model, i.e. of the SATIRE-S model, is that one can only reconstruct irradiance for the times when magnetogram measurements are available. Krivova et al. (2007) employed a different SATIRE model, called SATIRE-T for the telescope era (see Sect. 1.3.3), to reconstruct TSI since 1700. In their case, disc integrated values of the model atmospheres and disc integrated magnetic flux of the considered magnetic features are used. They also included an additional magnetic feature in the calculation of the TSI, the ephemeral regions or small bipolar regions. The solar magnetic flux is determined using a model from Solanki et al. (2002a) from the sunspot number.

In the present work, we aim at reconstructing TSI in the past at times when there are no magnetograms available using a SATIRE-S type model. To keep the spatial information of the magnetic features we employ a surface flux transport model (SFTM) and obtain the magnetic flux distribution on the photosphere, as a magnetogram does. Keeping the spatial information allows to reconstruct TSI more accurately since the brightness of the magnetic features also depends on the position on the solar disc (see Sect. 1.3.2). Wang et al. (2005) reconstructed TSI since 1713 using the irradiance model from Lean (2000) and a SFTM to calculate the magnetic flux on the photosphere. Although the model from Lean (2000) also assumes that the irradiance changes are due to the evolution of magnetic fields on the solar surface like in the SATIRE-S model, it doesn't contain spatial information of the distribution of the magnetic fields. They investigated a secular trend in the TSI from their reconstruction over the last 26 cycles and derived an increase since the Maunder minimum. In this chapter we first test the SATIRE-S model and the SFTM by trying to reproduce the TSI during the observed period since 1978. After this preliminary and incomplete study we aim at reconstructing further back in time (see Ch. 4).

In Sect. 3.3 and Sect. 3.4 we describe, respectively, the basics of the SFTM used to retrieve information on the distribution of the magnetic flux on the solar photosphere and the modifications made in the SATIRE-S model to suit the data from the SFTM. Section 3.5 presents the results obtained from the TSI reconstructions as compared with the observations and finally Sect. 3.6 summarises the outcome of the reconstructions and discusses them in the context of other TSI reconstructions and the possible missing effects in the models.

### 3.3 The Surface Flux Transport Model

#### 3.3.1 The induction equation

SFTM basically solve the induction equation to simulate the time evolution of magnetic fields on the solar photosphere. The induction equation, Eq. (3.1), in vector form contains two terms.

$$\frac{\partial \mathbf{B}}{\partial t} = \nabla \times (\mathbf{v} \times \mathbf{B}) - \nabla \times (\eta \nabla \times \mathbf{B}) \quad (3.1)$$

The first term on the right hand side of Eq. (3.1) is the induction term where  $\mathbf{v}$  represents the velocity field. The second term is the diffusion term, where  $\eta$  is the magnetic diffusivity defined as

$$\eta = \frac{c^2}{4\pi\sigma} \quad (3.2)$$

with  $\sigma$  being the conductivity of the plasma. Considering  $\eta$  as constant and using some vector identities Eq. (3.1) becomes

$$\frac{\partial \mathbf{B}}{\partial t} = \nabla \times (\mathbf{v} \times \mathbf{B}) + \eta \nabla^2 \mathbf{B}. \quad (3.3)$$

The 2-D SFTM used here was developed by Baumann (2005). It assumes that the magnetic field on the surface of the Sun is purely radial. This is reasonable since the magnetic field of the faculae and network is only weakly inclined relative to the vertical (Solanki 1993, Martinez Pillet et al. 1997). The SFTM also assumes that the transport of the large-scale magnetic field on the photosphere is the cause of the effects of differential rotation,  $\omega$ , meridional flow,  $\mathbf{v}$ , and surface diffusivity,  $\eta_h$ . Thus, the model solves Eq. (3.3) in spherical coordinates for the radial magnetic field component  $B_r(\theta, \phi, t)$  as follows

$$\begin{aligned} \frac{\partial B_r}{\partial t} = & -\omega(\theta) \frac{\partial B_r}{\partial \phi} - \frac{1}{R_\odot \sin(\theta)} \frac{\partial}{\partial \theta} \left( v(\theta) B_r \sin(\theta) \right) \\ & + \frac{\eta_h}{R_\odot^2} \left[ \frac{1}{\sin \theta} \frac{\partial}{\partial \theta} \left( \sin \theta \frac{\partial B_r}{\partial \theta} \right) + \frac{1}{\sin^2 \theta} \frac{\partial^2 B_r}{\partial \phi^2} \right] \\ & + S(\theta, \phi, t) - D_r(\eta_r B), \end{aligned} \quad (3.4)$$

where  $\theta$  and  $\phi$  represent the colatitude and longitude, respectively, on the solar surface and  $R_\odot$  is the radius of the Sun. The first two terms in the right side of Eq. (3.4) come from the advection component of the induction equation, where  $\omega(\theta)$  is the differential rotation and  $v(\theta)$  is the meridional flow. Thus, the velocity profile in Eq. (3.3) is a sum of the differential rotation in the  $\theta$  direction and the meridional flow in the  $\phi$  direction. The following two terms correspond to the diffusive component with  $\eta_h$  representing the magnetic surface diffusivity. Finally,  $S(\theta, \phi, t)$  and  $D_r(\eta_r B)$  are additional terms describing the emergence and the radial loss of magnetic flux, respectively. The parameter  $D_r$  was introduced by Baumann (2005) and Baumann et al. (2006) to account for the diffusion in the radial direction (i.e. the third dimension missing in the 2-D SFTM), as originally proposed by Schrijver et al. (2002), to model more realistically long-term trends of solar activity (for details see Baumann 2005). In particular, this decay term was needed to reproduce the reversal of the polar fields after the strong cycle 19 as it was followed by a weak cycle 20. Without it, the net field reaching the poles during cycle 20 wouldn't

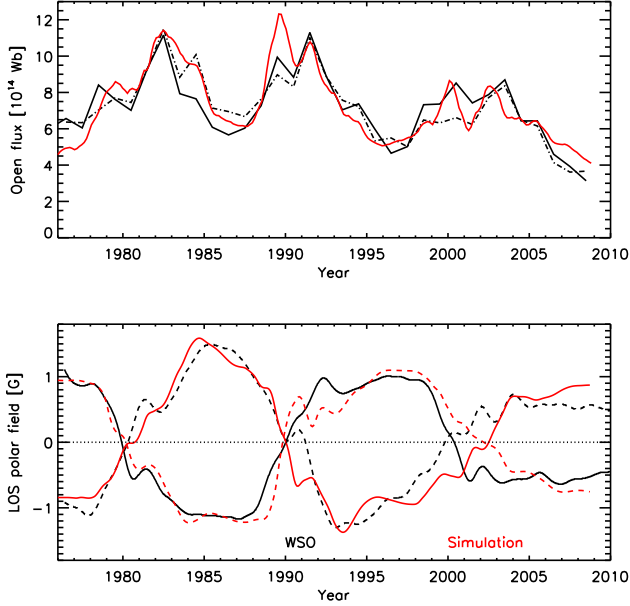


Figure 3.1: Top: Open flux as computed from the surface SFTM (red), the open flux as reconstructed from the aa-index (black solid line) and the OMNI data (black dashed line). Bottom: Line of sight polar field as calculated by the SFTM (red) compared to the observations from the WSO (black). The simulation results have been multiplied by a factor of 1.5 to match the observations due to calibration effects Svalgaard et al. (1978).

have been enough to cancel out the polar field from cycle 19 and no reversal would have occurred. The SFTM has been able to reproduce observables such as the polar field, open flux and total photospheric flux (Schüssler and Baumann 2006, Cameron and Schüssler 2007, Jiang et al. 2010a).

### 3.3.2 The source function: including the tilt angle of sunspot groups

The emergence of magnetic flux on the solar surface in the form of bipolar magnetic regions is characterized by the source function  $S(\theta, \phi, t)$  in the SFTM. Following Baumann et al. (2004), the new flux of an active region is injected to the solar surface in the form of two opposite polarity regions centered at latitude  $\lambda_+$  and longitude  $\phi_+$ , and  $\lambda_-$  and  $\phi_-$ . The magnetic field distribution corresponding to each polarity,  $\pm$ , is given by the gaussian in Eq. (3.5) (Eq. 3 in Cameron et al. 2010).

$$B^\pm(\lambda, \phi) = B_{max} \left( \frac{0.4\Delta\beta}{\delta} \right)^2 \exp(2[1 - \cos(\beta_\pm(\lambda, \phi))]/\delta^2) \quad (3.5)$$

$B_{max}$  is an amplitude parameter fixed by fitting the simulation results to the total unsigned flux as observed by the Mount Wilson and Wilcox Observatories. The polarity separation is found to be  $\Delta\beta = 0.45A_R^{0.5}$  from the Kodaikanal and Mount Wilson sunspot group data sets where  $A_R$  is the total area of an active region.  $\beta_{\pm}(\lambda, \phi)$  are the heliocentric angles between a point on the surface  $(\lambda, \phi)$  and the center of the positive  $(\lambda_+, \phi_+)$  and negative  $(\lambda_-, \phi_-)$  polarity. To obtain the positions  $(\lambda_{\pm}, \phi_{\pm})$  and the separation between the two polarities,  $\Delta\beta$ , of an active region, one needs to know its position and area. The total area of an active region can be estimated from the sum of the areas of sunspots,  $A_s$ , and faculae,  $A_f$  (Schüssler and Baumann 2006, Jiang et al. 2010a, Cameron et al. 2010). For sunspots, Cameron et al. (2010) use daily sunspot group areas and positions from a data set compiled by the Royal Greenwich Observatory (RGO) from 1874 to 1976 and USAF/NOAA onwards <sup>1</sup>. Since there is no information on individual sunspots, the central location of each polarity portion is based on the central position of the group as taken from the data set, the polarity separation  $\Delta\beta$ , and the tilt angle  $\alpha$  with respect to the azimuthal direction. For faculae, the areas are taken from the observationally derived relation between facular and sunspot areas by Chapman et al. (1997).

Typically, a sunspot will appear on the solar surface and during the following days its area will grow as more magnetic flux emerges. It reaches a maximum area after which the sunspot slowly decays, diffusing its magnetic flux on the solar photosphere. The SFTM has a spatial resolution of  $1^\circ \times 1^\circ$  on the solar surface and thus, very small bipolar regions cannot be resolved. For this reason, the sunspot groups are injected onto the photosphere on the day when the maximum area is reached (Baumann 2005). A big sunspot (about  $1000 \mu\text{H}$  in area) could survive several rotations, thus appearing more than once on the visible hemisphere. The daily observations usually don't follow a sunspot group after it disappears to the far side of the Sun. A returning sunspot group to the visible hemisphere is usually given a different sunspot group number in the records, although exceptionally they can be identified as returning and maintain their original number. Therefore, it is possible that some sunspot groups are introduced twice in the SFTM, providing more flux to the photosphere than there should be in reality.

Dasi-Espuig et al. (2010) published an analysis of sunspot group tilt angles using observations from Mount Wilson and Kodaikanal observatories (see Ch. 2). The main findings in their paper are that the cycle averaged tilt angle of sunspot groups, or more precisely Joy's law, varies on a cycle-to-cycle basis and that these are anti-correlated with the strength of the cycle (total area covered by sunspots during one solar cycle). They further show that a combination of cycle averaged, area- and latitude- weighted tilt angles, and the strength of the same cycle are positively correlated with the strength of the next cycle with a correlation coefficient of  $r = 0.65$  (11% chance probability) and  $r = 0.70$  (8% chance probability) for Mount Wilson and Kodaikanal data sets respectively. Cameron et al. (2010) have included the cycle-to-cycle variation of the tilt angles in the SFTM. Here we employ the same model, but the tilt angles are taken from the observed linear relationship between the cycle strength and cycle averaged tilt angle instead. The tilt angle enters in the calculation of the positions of the individual polarities,  $(\lambda_{\pm}, \phi_{\pm})$ , needed to model the active regions in the source function (Eq. 3.5). After this new modification,

<sup>1</sup><http://solarscience.msfc.nasa.gov/greenwch.shtml>

they found a good match with the observed open flux and polar field reversal times when  $\eta_r = 0$ . Thus, the global diffusive term in Eq. (3.4),  $D_r$ , is no longer needed to reproduce such observations if the time variation of the tilt angle of sunspot groups is provided. However, Jiang et al. (2011a) do give a small value to the radial diffusivity (25 km<sup>2</sup>/s) when reconstructing the open flux since 1700. In their work the radial diffusivity is needed to compensate for errors in the sunspot numbers from the early records. Otherwise, the decay time due only to  $\eta_h$  is around 4000 years, affecting the field also during the last century.

The plots in Fig. 3.1 reflect the success of the SFTM in reproducing the open flux as inferred from the aa-index of geomagnetic variations (Lockwood 2003) and also with the OMNI spacecraft data. The top panel shows the reconstructed open flux (top panel) and the line-of-sight polar field (bottom panel) as compared to the observations (black) for the last 3 solar cycles, i.e. the same period covered by TSI observations and for which we reconstruct TSI (see Sect. 3.5). The bottom panel plots the line-of-sight polar field from which we can see that the simulation also matches the timing of the polar field reversals, as we can see from the comparison between the simulation (red) and the observations (black) from Wilcox Solar Observatory (WSO) at the times of minima. Only the reversal during cycle 23 is delayed in the simulations with respect to the observations.

### 3.4 SATIRE: method

Here we follow a similar method as the one described by Fligge et al. (2000) and Wenzler et al. (2004, 2005, 2006) to reconstruct TSI. Instead of using direct observations of the surface magnetic fields, we make use of a SFTM (described in Sect. 3.3). It simulates the magnetic fields on the surface of the Sun providing the same information as a magnetogram. Hence, we compute solar irradiance with SATIRE-S modified to suit the modelled magnetograms from the SFTM.

The SFTM provides a daily synoptic chart of the radial magnetic field of the whole solar surface (360° in longitude and 180° in latitude) with a spatial resolution of 1° x 1° on the solar surface. An example of one of such synoptic charts is Fig. 3.2. At such resolution, the portion of the Sun covered by a pixel is big enough to contain all of the magnetic features in the SATIRE-S model, namely faculae and network, sunspot umbra and sunspot penumbra. Consequently, the filling factors in a pixel will be between 0 and 1 for all components. The main issue now is to obtain the filling factors at such spatial resolution of the simulated magnetograms.

Firstly, we increase the spatial resolution by dividing each pixel,  $(i, j)$ , in the simulated magnetogram into 100 sub-pixels,  $(k, l)$ , to locate the observed sunspot groups and their area coverage on the magnetograms more accurately. The positions and areas of sunspot groups are taken from the same sunspot group data set used in the SFTM (sec. 3.3). Therefore, known the central coordinates in latitude and longitude of the sunspot groups,  $(\theta, \phi)_c$ , and their area,  $A_s$ , we are able to locate the sub-pixels  $(k, l)$  where the sunspot group falls. To do this we consider the bipolar group to be constituted by two circular portions of equal radius

$$r_{1,2} = \sqrt{\frac{A_s}{2\pi}}, \quad (3.6)$$

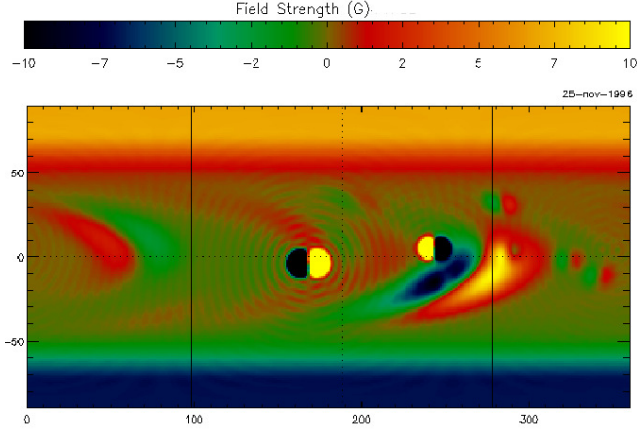


Figure 3.2: Radial component of the magnetic field strength (color coded) on the solar photosphere from the surface flux transport model. The x-axis is latitude in degrees and the y-axis is longitude in degrees. The dotted line shows the central meridian and the two black solid lines delimit the near side of the sun.

where the subscripts (1, 2) refer to the leading and following portions respectively. The center of each portion is displaced longitudinally with respect to the center of the sunspot group  $\phi_c$  an amount equivalent to their radius, while the latitude position is the same as that of the sunspot group center,  $\theta_c$ ,

$$\begin{aligned} k_{1,2} &= \theta_c, \\ l_{1,2} &= \phi_c \pm r_{1,2}. \end{aligned} \quad (3.7)$$

Note that in Eq. (3.7) we are not considering the tilt angle of the sunspot groups. At the original resolution of  $1^\circ \times 1^\circ$  on the solar surface, we don't expect that it will have a considerable effect in the total disc integrated irradiance. Once the sub-pixels ( $k, l$ ) where the sunspot groups fall are identified, we count them, obtaining  $n_s$ . In this way, the fraction of the original  $1^\circ \times 1^\circ$  pixel, ( $i, j$ ), that is covered by sunspots will be

$$f_s(i, j) = n_s(i, j)/100. \quad (3.8)$$

The rest of the pixel that is not covered by sunspot is considered to be filled by faculae and quiet Sun. The corresponding fraction is

$$f_{f+qs}(i, j) = (100 - n_s(i, j))/100. \quad (3.9)$$

For the calculation of the facular filling factors we need the magnetic field strength in the original pixel that remains after removing the magnetic field strength due to the sunspots. Thus, we approximate the field strength in a pixel due to everything that is not a sunspot as

$$\beta(i, j) = B_r(i, j)f_{f+qs}(i, j), \quad (3.10)$$

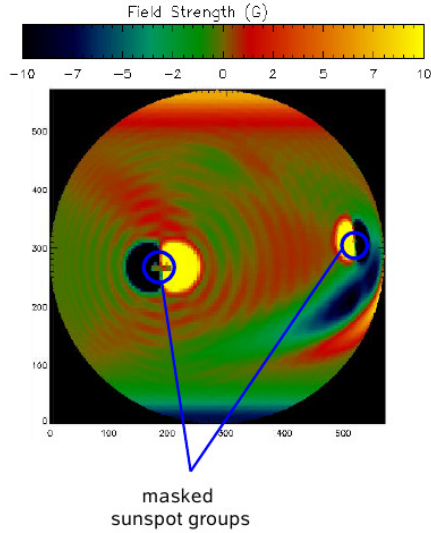


Figure 3.3: Projection of the synoptic chart in Fig 3.2 where the pixels covered by sunspots have been masked by their corresponding fractions (indicated by the blue circles). The X- and Y- axes are both in units of pixels. The strength of the radial magnetic field is color coded as given by the color bar.

where  $B_r(i, j)$  is the radial magnetic field strength of the pixel  $(i, j)$ . It is important to point out that we are distributing the magnetic flux of the pixel to sunspot and faculae linearly. In reality, however, the flux is more concentrated in sunspots than in faculae (Keppens and Martinez Pillet 1996). We don't correct for this since we expect that it will have an effect mainly in the short-term variation of the solar irradiance and we are more interested in the long-term behaviour.

From the masks  $f_s(i, j)$  and  $\beta(i, j)$  we calculate the filling factors for sunspots and faculae respectively, but first we project these images to obtain the portion of the solar disc visible from the Earth and the correct area contribution of each pixel. Figure 3.3 is the projection of the visible hemisphere of the synoptic chart in Fig. 3.2. Two young active regions can be spotted near the equator, one closer to the disc center and the other one closer to the limb, where the yellow patch represents the positive polarity and the blue one the negative. The blue lines and circles indicate the location of the sunspot groups inside the active region that have been masked. The coordinates for the projected images are denoted as  $(i', j')$ . The filling factors for sunspots are directly the fraction of surface covered by them,

$$\alpha_s(i', j') = f_s(i', j'). \quad (3.11)$$

The filling factors for faculae are extracted from  $\beta(i', j')$  in a similar way as described by Fligge et al. (2000) since even after increasing the spatial resolution we cannot locate nor

distinguish faculae from quiet Sun. The facular filling factor is taken to increase linearly with field strength,  $\beta(i', j')$ , from zero to unity at a saturation value,  $B_{sat}$ , of the field strength,

$$\alpha_f(i', j') = \begin{cases} \beta(i', j')/B_{sat} & \text{if } \beta(i', j') < B_{sat} \\ 1 & \text{if } \beta(i', j') \geq B_{sat} \end{cases} \quad (3.12)$$

$B_{sat}$  is the only free parameter of the model and it is interpreted as the average field strength at which the brightness of the magnetic element saturates (Solanki and Stenflo 1984, Foukal and Fowler 1984, Ortiz et al. 2002). This is, we assume that as the filling factor increases, so does the intensity contrast until it reaches a saturation value, above which it will contribute to a constant brightening given by the model atmospheres (Fligge et al. 2000). For the quiet Sun filling factors we use the following relation (see Sect. 1.3.3)

$$\alpha_q(i', j') = 1 - \alpha_s(i', j') - \alpha_f(i', j'). \quad (3.13)$$

To compute the TSI we employ Eq. (1.4) where we integrate over all wavelengths. The filling factors are converted from position  $(i', j')$  to  $\mu$  and the calculation of TSI is now the direct summation of the product of the filling factor and brightness intensity of each of the 4 magnetic components in the SATIRE model. To separate the umbral and penumbral contributions we use the ratio 0.25 of umbral to penumbral areas as employed by Wenzler et al. (2006) following Brandt et al. (1990).

## 3.5 Results

In Sect. 3.4 we described how to reconstruct the TSI using the SATIRE model and simulated magnetograms from a surface flux transport model. Here we present the reconstructed TSI for the period covering solar cycles 21 – 23 at different  $B_{sat}$  values and compare them to the PMOD composite of observations. The PMOD composite starts from November 1978<sup>2</sup>, thus our reconstructions start on the same date and go until the end of 2008.

We are interested in the correct reproduction of long-term variations of the TSI, i.e. to reproduce the amplitude and shape of the TSI cycles and the minima levels. For this reason we also chose to compare our reconstructions with PMOD after a smoothing of 3 months. Table 3.1 lists the correlation coefficient between PMOD and our reconstructions, the slope of a linear fit between the two data sets and its corresponding  $\chi^2$  value, for the range of  $B_{sat}$  values used, both before and after smoothing the data over 3 months. In the plots, the curves corresponding to the reconstructions are shifted to match the mean value of PMOD. The parameters in Table 3.1 for the smoothed data show higher values of the slope and correlation coefficients, and lower  $\chi^2$  values than for the unsmoothed data. This was expected since the reconstructions are not that accurate on a daily and rotational basis due to the low spatial resolution of the magnetograms. Daily and rotational variations are excluded by taking the moving average, resulting in higher correlation coefficients and lower  $\chi^2$  values. Figure 3.4 plots the smoothed reconstructed TSI for different saturation values together with the PMOD. These curves illustrate the fact that high saturation values diminish the effect of faculae in the TSI through the filling factors and lower saturation

<sup>2</sup><http://www.pmodwrc.ch/pmod.php?topic=tsi/composite/SolarConstant>

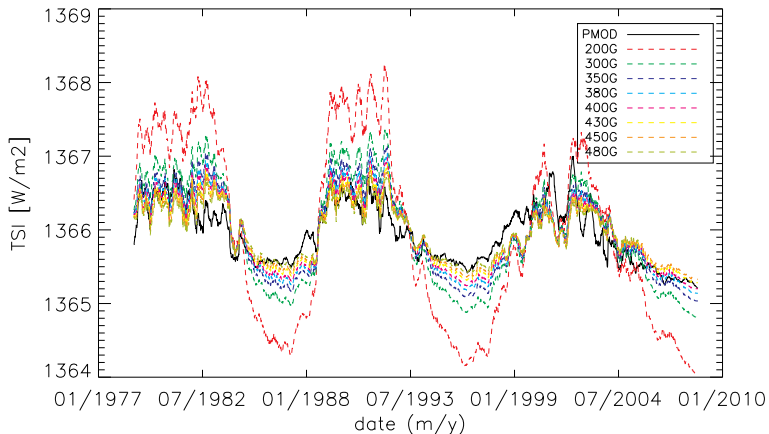


Figure 3.4: TSI reconstructions with different  $B_{sat}$  values smoothed over 3 months represented by different colors according to the legend. Black represents the PMOD composite also smoothed over 3 months.

Table 3.1: Correlation coefficient,  $r$ , slope,  $s$ , and  $\chi^2$  for reconstructions at different  $B_{sat}$  values vs. PMOD.

$B_{sat}$ [G]	no smoothing			3 months smoothing		
	$r$	$s$	$\chi^2$	$r$	$s$	$\chi^2$
200	0.718	1.664	8825.3	0.866	2.610	3829.2
300	0.753	1.118	3238.3	0.865	1.546	1359.8
350	0.759	0.960	2292.9	0.863	1.237	890.5
380	0.759	0.886	1952.4	0.860	1.090	707.3
400	0.757	0.842	1786.0	0.858	1.005	612.2
430	0.752	0.784	1602.1	0.854	0.892	499.5
450	0.747	0.750	1512.9	0.851	0.825	440.1
480	0.737	0.704	1416.3	0.844	0.734	368.6

values result in larger amplitude variations of the TSI cycle. The top panel in Fig. 3.5 plots in red the reconstructed TSI for  $B_{sat} = 400$  G, value for which the slope is closer to unity when smoothing over 3 months, and in black PMOD. The dips caused by the passage of sunspots are, in overall, deeper in our reconstruction than in PMOD. This could cause a systematically lower slope than in the case for the smoothed curves when comparing the reconstruction with PMOD. The two smaller plots are enlargements of shorter periods where one can appreciate the accuracy of the reconstruction at shorter time scales. The panel to the left covers a period of 6 months and the panel to the right of 2 years during the

descending phase of cycle 22. From these plots we can see that the reconstruction (red) is able to reproduce most of the dips caused by the passage of spots across the solar disc at the right times. However, for big and long lived sunspots the model fails to reproduce the shape of the dip, showing a thinner broadening and a darkening that starts later than observed (see Fig. 3.5, bottom left panel around 04/1980). This is a consequence of injecting the sunspots in the surface flux transport model at the time when they reach their maximum area (see Sect. 3.3). By introducing sunspots at the time when they reach their maximum area we are missing the previous days when the sunspot first appears and grows in size. The sunspots at the early stages will already cause a darkening in the observed TSI that we don't reproduce in our reconstructions due to the fact that they are not present in the surface flux transport model.

More important are longer time scales, where we also find some discrepancies. These are better noticed when plotting the difference between the reconstruction and PMOD.

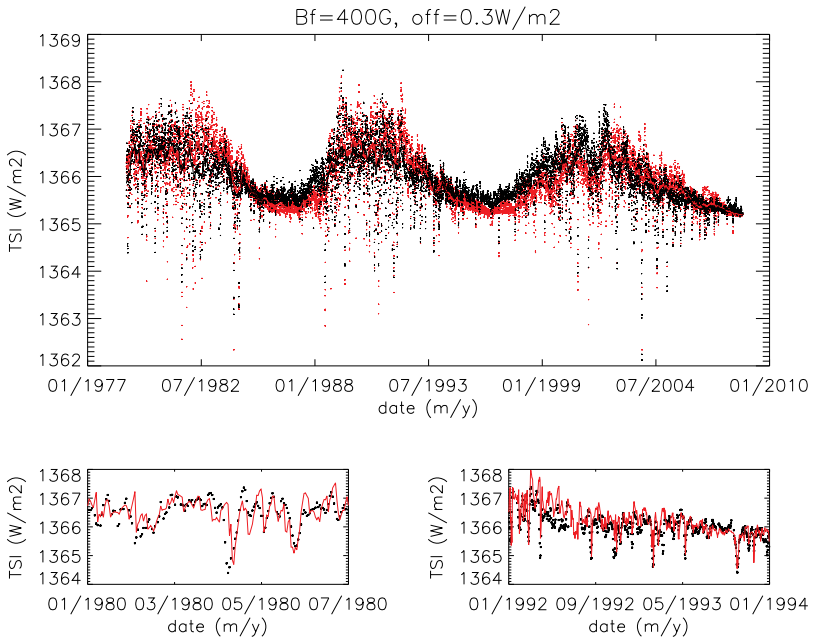


Figure 3.5: On the top the value of  $B_{sat}$  and the offset applied to the reconstruction are specified. Top panel: Reconstructed TSI (red dashed lines) as compared with PMOD (black dots). The thick solid curves are the same data after a smoothing of 3 months, in black for PMOD and in red our reconstruction. Bottom panel: Enlargements of two shorter periods. Black dots are again PMOD values and the red dashed lines represent the reconstruction.

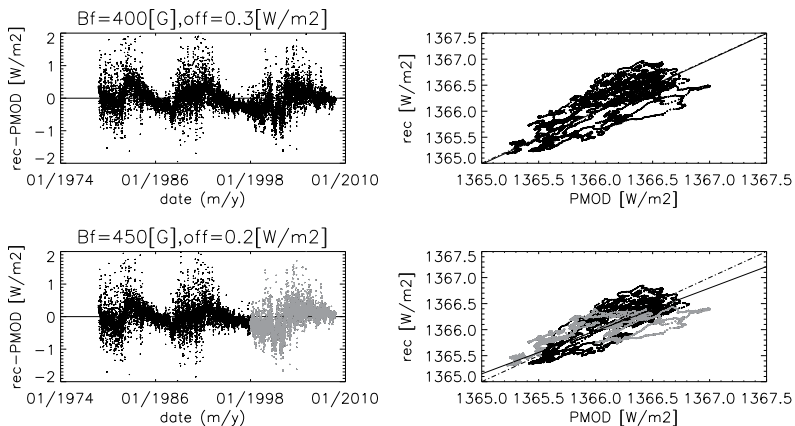


Figure 3.6: In all panels black is for cycles 21 and 22 and grey for cycle 23. The top panels correspond to the best fit reconstructions considering all 3 cycles while bottom panels consider only cycles 21 and 22. Left panels: Difference between the reconstructed values and PMOD over time. The thick black curve represents this difference smoothed over 3 months. Right panels: Reconstructed values vs. PMOD both smoothed over 3 months. The solid line represents a linear fit to the points and the dash-dotted line is the expected fit  $y = x$ .

Fig. 3.6 plots the differences in the left panels and the reconstruction versus PMOD in the panels to the right, for saturation values  $B_{sat} = 400$  G (upper) and  $B_{sat} = 450$  G (lower). The periods of time at which the differences are most noticeable are: (1) During the second half of the maximum of cycle 21 and the maximum of cycle 22, the reconstruction is higher than the observed level, and (2) during the minimum between cycles 22 and 23 and the ascending phase of cycle 23 the reconstructed TSI is lower than observed and slightly higher during the descending phase. This differences are also seen between the simulated and observed total unsigned flux (see Fig. 3.8). It is important to point out that the average tilt angle for cycle 22 was multiplied by a factor of 1.3 in the surface flux transport model to better match the simulated and observed open flux and polar field. The artificial increase in the tilt angles also caused an increase in the total unsigned flux on the solar surface during the minimum between cycles 22 and 23, obtaining a better correspondence with the observed total and open flux (see Fig. 3.8, cf. Jiang et al. 2010a). To test the sensibility of our irradiance model to the tilt angles we also computed the TSI with no artificial increase in the tilt angles of cycle 22, with an increase of 1.3 and 1.4. The  $\chi^2$  values in the three cases are very similar, between 600–700 for a  $B_{sat} = 400$  G and a smoothing of 3 months. The case with an increase of 1.3 gives the lowest  $\chi^2$  values of the three.

We also calculated the fit parameters between the reconstructions and the PMOD for cycles 21 and 22 alone. Table 3.2 lists the correlation coefficients, the slope of a linear fit between the reconstruction and PMOD and the  $\chi^2$  values of the fit, for both non-smoothed

Table 3.2: Correlation coefficient,  $r$ , slope,  $s$ , and  $\chi^2$  for reconstruction at different  $B_{sat}$  values vs. PMOD for cycles 21 and 22 alone.

$B_{sat}$ [G]	no smoothing			3 months smoothing		
	$r$	$s$	$\chi^2$	$r$	$s$	$\chi^2$
300	0.775	1.264	2225.4	0.896	1.951	604.5
400	0.785	0.954	1186.8	0.887	1.267	283.7
430	0.781	0.889	1058.9	0.882	1.123	236.9
450	0.776	0.851	997.9	0.879	1.037	212.4
480	0.767	0.799	933.2	0.872	0.923	183.6

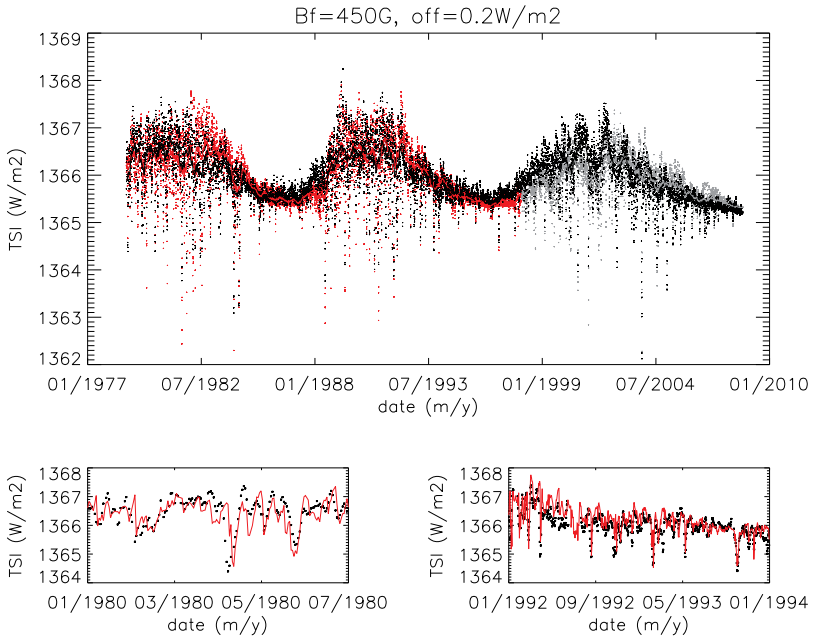


Figure 3.7: TSI reconstruction with a  $B_{sat} = 450$  G where the reconstructed curve has been offset by  $0.2\text{W m}^{-2}$  to match the mean level of PMOD. Top panel: Reconstructed TSI (red) as compared with PMOD (black). The solid curves are the same data after a smoothing of 3 months. Cycle 23 appears in light grey to indicate that the parameters of the fit between the reconstructions and PMOD are calculated excluding this last cycle. Bottom panel: Enlargements of two shorter periods for PMOD (black) and the reconstruction (red).

and 3 months smoothed data, for cycles 21 and 22 alone. The slopes and the correlation coefficients result higher than in the case for the 3 solar cycles. In this case, the slope

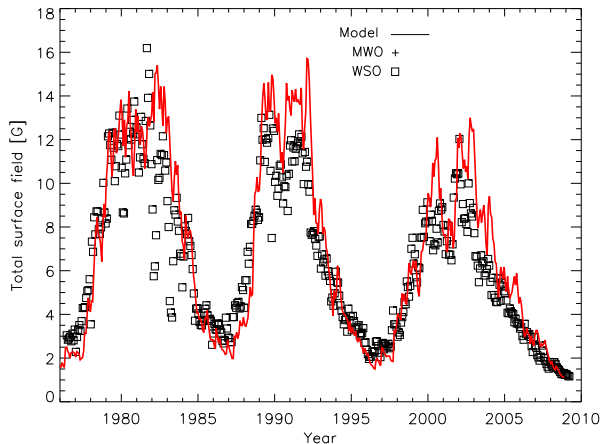


Figure 3.8: Average unsigned magnetic field for solar cycles 21–23 as simulated by the surface flux transport model after increasing artificially the mean tilt angle for cycle 22, compared with the observations from Mount Wilson (plus signs) and Wilcox Solar Observatories (squares).

closest to unity for the smoothed data,  $s = 1.037$ , is obtained at a  $B_{sat} = 450$  G, which is slightly higher than the  $B_{sat} = 400$  G found when taking the whole period of observations. Figure 3.7 shows plots comparing the reconstructed TSI with the observations for this saturation value. One can see that there are some slight differences between the thick red smoothed curves in Fig. 3.5 for the whole period, and Fig. 3.7 for cycles 21 and 22 alone. On one hand, the amplitude of the TSI for cycles 21 and 22 is better reproduced now and one can see in Fig. 3.7 that the minima between cycles 20 and 21, and 21 and 22, are at level with the PMOD while before (Fig. 3.5) they lay below. Also, the maxima of both cycles 21 and 22 are closer to the PMOD in this period, although one can see that still the reconstruction overestimates the TSI during the last half of the maximum of cycle 21. On the other hand, the TSI variations of cycle 23 are reproduced better when using a  $B_{sat} = 400$  G. A close examination at the difference plots in Fig. 3.6 show that the reconstructions for both  $B_{sat} = 400$  G and  $B_{sat} = 450$  G remain below PMOD during the ascending phase of cycle 23 by about  $0.2 \text{ W m}^{-2}$  on average.

### 3.6 Conclusions and discussion

As a new approach for reconstructing TSI, we have developed a modified version of the SATIRE-S model suited to work with simulated magnetograms. The simulated magnetograms are the product of a SFTM and provide the radial magnetic field on the solar photosphere. One mayor difference in the present SATIRE-S model as compared

with previous ones (e.g. Wenzler et al. 2006) comes from the fact that the magnetograms are not measured but are based only on sunspot data. The simulated magnetograms have a much lower resolution ( $1^\circ \times 1^\circ$  on the solar surface) and thus we can't always resolve spatially sunspot groups from faculae and network. The facular fields are introduced employing an empirical relationship between facular and sunspot areas (Chapman et al. 1997), while the only source of network fields are active regions.

The SATIRE-S model used here to reconstruct the irradiance uses both a sunspot group area and position record to locate the sunspots on the simulated magnetograms and the simulated magnetograms to locate and account for the magnetic field strength of faculae and network (see Sect. 3.4). We firstly reconstructed the period when there are direct observations of the TSI (since November 1978), and compared them with the PMOD composite (Table 3.1). The main findings after reconstructing the TSI for the last 3 solar cycles can be summarized as follows:

- On time scales of days the model gives reasonable, but not good results. It reproduces the dips caused by the passage of sunspots across the solar disc at the right times. However, due to the treatment of the sources in the SFTM, the shapes of the dips do not match completely the observed.
- The PMOD composite and the reconstructions of TSI show higher correlation coefficients and lower  $\chi^2$  values after smoothing the data over 3 months. This is reasonable since after smoothing the data the dispersion in the TSI caused by the sunspots is reduced (Table 3.1).
- When fitting the reconstructed values versus the PMOD, the closest slope to unity is achieved with a value of the free parameter of  $B_{sat} = 350$  G for the non-smoothed data and  $B_{sat} = 400$  G for the 3 months smoothed data (Table 3.1), of all the  $B_{sat}$  values that we tried.
- On time scales of months to years, we find that (1) at the maximum of both cycles 21 and 22 the reconstruction gives higher values than PMOD and (2) the minimum between cycles 22 and 23 and the ascending phase of cycle 23 lie below the PMOD values, while during the descending phase it remains higher.

Cycle 23 turned out to be more difficult to reproduce than cycles 21 and 22, needing an extra free parameter in the SFTM to reproduce consistently the open flux and the polar field. Thus, we also reconstructed cycles 21 and 22 alone and the results of these are presented in Table 3.2. A comparison between the results for only cycles 21 and 22 and the whole period of observations shows that for the 3 months smoothed data, the slope closest to one is achieved for a  $B_{sat} = 450$  G, higher than the  $B_{sat} = 400$  G found when reconstructing the whole period. This gives a better correspondence between the reconstructed TSI and PMOD for cycles 21 and 22, in particular during the minima.

Our reconstructions of the TSI have been partly successful in spite of the low spatial resolution of the simulated magnetograms. The correlation coefficients are as high as  $r = 0.76$  and  $r = 0.86$  for the non-smoothed and 3 months smoothed data, respectively, when the slopes,  $s$ , are closest to unity. The correlation coefficient for the non-smoothed data is certainly not as high as the  $r = 0.91$  found by Wenzler et al. (2006) when using a SATIRE-S model with continuum images and magnetograms to reconstruct the TSI for

the last 3 solar cycles. However, it is comparable to the  $r = 0.78$  found by Krivova et al. (2007) for their non-smoothed reconstruction using the standard SATIRE-T model. In the SATIRE-T model there is no spatial information of the magnetic features on the solar surface so that the filling factors are disc integrated (as are the intensities from the model atmospheres). The daily disc integrated magnetic flux from the different components contributing to the TSI is needed to obtain the filling factors and is indirectly determined in Krivova et al. (2007) by the model of Solanki et al. (2002a). In contrast to our SATIRE-S model, the SATIRE-T model employed by Krivova et al. (2007) includes additionally the flux from ephemeral regions or small bipolar regions. Ephemeral regions are small short lived bipoles that appear on the solar surface at a wider range of latitudes than sunspots (Harvey and Martin 1973, Harvey 1992). They don't possess sunspots, albeit the total flux of all ephemeral regions appearing on the photosphere in one day can be of the same order of magnitude as in an active region due to their high rate of emergence (Schrijver and Harvey 1994, Schrijver et al. 1998). More interestingly, ephemeral regions show a cyclic behaviour as in the case of sunspots that starts around 2 to 3 years before sunspot cycle minimum (Harvey 1992, 2001, Tlatov et al. 2010). The SFTM doesn't include the flux from ephemeral regions for two main reasons. One, the spatial resolution is not high enough to inject them on the solar surface as it's done for sunspots, and two, a daily continuous and homogeneous data set of ephemeral regions doesn't exist at the present time. The lack of flux from ephemeral regions in the SFTM could be reflected mainly during the minima and the ascending phases. This is due to the fact that ephemeral regions appear 2 to 3 years before the start of a new cycle and peak during the ascending phase of the new sunspot cycle. In the following chapter we include the flux from ephemeral regions, improving the TSI reconstructions during the minimum between cycles 22 and 23 and the ascending phase of cycle 23.

# 4 Solar irradiance reconstructions: including ephemeral regions

## 4.1 Abstract

In this Chapter we aim at reconstructing total solar irradiance (TSI) since 1878 with the SATIRE-S model in combination with the surface flux transport model. Chapter 3 described how the simulated magnetograms from the surface flux transport model are implemented in the SATIRE-S model to reconstruct TSI. That model describes the TSI changes caused by the evolution of active regions but does not include the effect of ephemeral regions. Ephemeral regions are small bipolar regions. In this Chapter we include the ephemeral region flux in the SATIRE-S model. The results show that after including the flux from ephemeral regions the TSI reconstruction for the observed period fits better the PMOD composite mainly during the times of minima and descending phases. The model is then used to reconstruct TSI since 1878. A comparison of the longer term TSI reconstruction with that from other authors shows differences in the cycle amplitudes but a similar secular change.

## 4.2 Introduction

The SATIRE-S model has been previously used to reconstruct solar irradiance during the period when measured magnetograms are available, i.e. since 1974 (Fligge et al. 2000, Krivova et al. 2003, Wenzler et al. 2004, 2005, 2006, Ball et al. 2011). To reconstruct solar irradiance further back in time, one uses SATIRE-T or SATIRE-M depending on how far back the reconstruction goes (Krivova et al. 2011b). To describe the evolution of sunspots, records of sunspot areas and positions are employed in the SATIRE-T model. However, recordings start only in 1874. Before 1874, the SATIRE-T model describes the evolution of sunspots based on the sunspot number, available since 1610. For earlier times, the SATIRE-M model is used and it relies on derived sunspot numbers from cosmogenic isotopes. The evolution of facular areas is more challenging to obtain since there are no reliable and direct measurements or proxies. This is partly solved by assuming that their evolution is related to that of sunspots, which is reasonable since they both are found in active regions. In our case, the surface flux transport model includes the facular flux by employing the observed quadratic relation between sunspot and facular areas by Chapman et al. (1997). The weak magnetic features like e.g. ephemeral regions, are, however, not well represented by the sunspot areas since they appear everywhere on the solar surface

and are always present, even at activity minima (Harvey and Martin 1973, Harvey 1992, 2001). For this reason, estimating long term trends in the solar irradiance is a difficult task.

Several long-term reconstructions have been produced in the past two decades (see Sect. 1.3.4 and, e.g. Solanki and Krivova 2004, Krivova and Solanki 2008 for an overview). The first TSI reconstructions since the Maunder minimum had a cyclic component (i.e. sunspot cycle variation) plus a secular component (i.e. cycle-to-cycle variation). The secular component was derived from stellar data that were later proved to be unreliable (Hall and Lockwood 2004). This led to the development of alternative methods to derive the secular trend.

Solanki et al. (2000, 2002a) presented a physical mechanism that explains the secular variation displayed by the open flux (Lockwood et al. 1999). Their model reconstructs the solar magnetic flux from the sunspot number and includes the overlap of the activity cycles of ephemeral regions. Using the reconstructed photospheric magnetic flux from the model by Solanki et al. (2002a), Krivova et al. (2007) computed TSI since the Maunder minimum using the SATIRE-T model. Foster (2004) also reconstructed TSI since the Maunder minimum, although he accounted for the facular component in his irradiance model by reconstructing the butterfly diagram for faculae from the record of sunspot areas and positions. Wang et al. (2005), in contrast, used a surface flux transport model to simulate the evolution of the total surface magnetic flux of the Sun to compute the variations of TSI. They included the flux from ephemeral regions although they dismissed the extension, and thus overlap, of the activity cycles of ephemeral regions, which is the key to a larger secular trend.

Our approach is to reconstruct TSI since 1874, i.e. as far back as the sunspot position and area record goes. For this we use the SATIRE-S model in combination with a surface flux transport model, described in the previous Chapter. The results from the previous Chapter suggested the need to include the flux from ephemeral regions, since the TSI levels during minima and the descending phases were lower than shown by the PMOD composite. Ephemeral regions appear around 2-3 years before sunspot minima, thus their flux is more noticeable during this period. Section 4.3 describes how the ephemeral region cycles are modelled and how their flux is included in the SATIRE-S model. Section 4.4 explains how the free parameters of the model are fixed and Sect. 4.5 presents the TSI reconstructions since 1878 and discusses them. Finally, Sect. 4.6 summarises the results.

### 4.3 Modeling the ephemeral region flux

Ephemeral regions are small bipolar regions, as shown in the lower left panel of Fig. 4.1. They have short lifetimes, typically of a few hours and are found over the entire solar surface, in contrast to active regions which are confined within latitudes  $\pm 40^\circ$ . The frequency of emergence is about 100 ephemeral regions per day, meaning that on average the total flux emerged in the form of ephemeral regions in a day is equivalent to that in one or more major active regions (Harvey and Martin 1973, Hagenaar 2001). The extensive work of Harvey and Martin (1973), Harvey (1992) also revealed that the number of ephemeral regions follows a cyclic pattern nearly in phase with the sunspot cycle, their minima occurring 2 to 3 years before sunspot minima. Hagenaar (2001), Hagenaar et al.

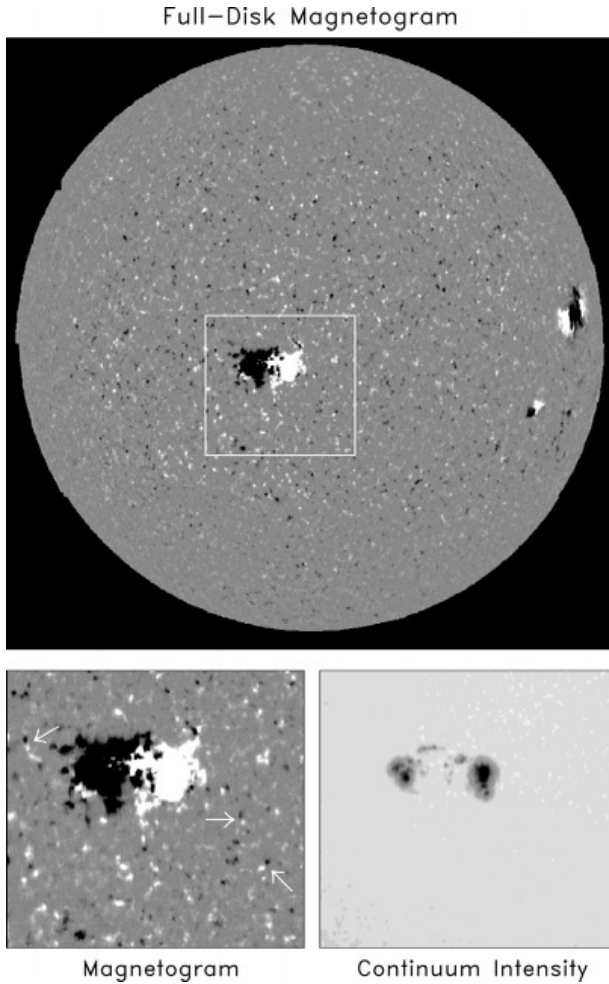


Figure 4.1: Full disc magnetogram of the Sun on 25 November 1996 showing a large bipolar active region with nearby ephemeral regions where black and white represent positive and negative magnetic field polarities. The two bottom panels are enlargements that correspond to the area outlined by the white box in the full disc magnetogram that show the size comparison and the association of sunspots (right panel) with a large active region (left panel). Ephemeral regions are indicated by the white arrows in the lower left panel. Taken from Harvey (2001).

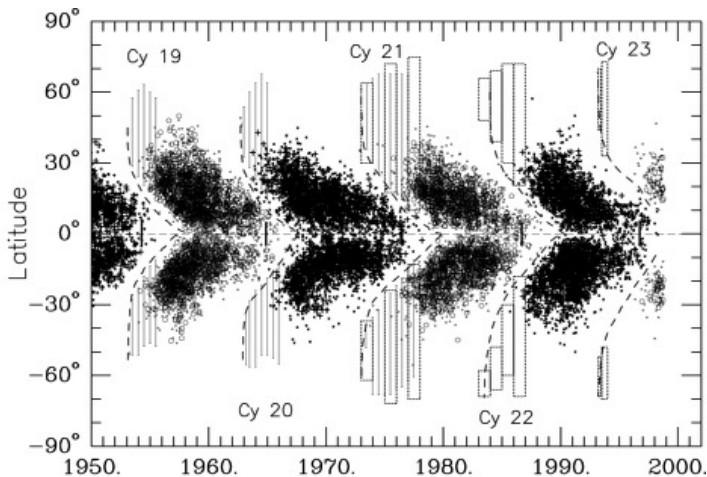


Figure 4.2: Butterfly diagram of sunspot groups and the latitude extent of ephemeral regions with the same orientation superposed. The vertical bars and boxes represent ephemeral regions identified as Ca II K regions and as magnetic bipoles respectively. The dashed curves are the boundaries between the activity of two consecutive cycles. Taken from Harvey (2001).

(2003), however, obtained different results, indicating an antiphase of the ephemeral region cycle with respect to the active region cycle. Ephemeral regions are identified with a cycle by the orientation of the bipole, that is, by their tilt angle. Although they show a wide range of orientations, they do present a preferred orientation, the same as that seen in the larger active regions, that persists throughout a cycle. During the declining phase of a sunspot cycle, the ephemeral regions emerging at high latitudes present an orientation reversed from the active regions and the low latitude ephemeral regions, indicating a new upcoming cycle. Figure 4.2 is the butterfly diagram of sunspot and ephemeral regions, showing the earlier appearance of the ephemeral regions to the sunspots in a cycle. Thus, the contribution of the ephemeral region flux to the magnetic flux on the solar surface and, hence, to the TSI, will be most noticeable during sunspot minima.

Direct and continuous measurements of ephemeral regions for extended periods of time are not available and the surface flux transport model does not account for the magnetic flux emerging from them due to the spatial resolution (see Sect. 3.3.2). Therefore we model their evolution in time using a simpler approach, to include the effect of these in the TSI reconstructions. Following Solanki et al. (2002b) and Vieira and Solanki (2010), the total flux emergence rate is the sum over all overlapping cycles considered

$$\varepsilon^{eph}(t) = \sum_{i=1}^N \varepsilon_i^{eph}(t), \quad (4.1)$$

where  $N$  is the number of cycles considered and  $\varepsilon_i^{eph}(t)$  is defined as

$$\varepsilon_i^{eph}(t) = X \langle \Phi_s \rangle_i g_i(t). \quad (4.2)$$

Here  $X$  is a scaling factor and  $\langle \Phi_s \rangle_i$  is

$$\langle \Phi_s \rangle = (0.2 \langle B_{z,u} \rangle + 0.8 \langle B_{z,p} \rangle) \langle A_s \rangle_i, \quad (4.3)$$

where  $\langle A_s \rangle$  is the maximum of the daily sunspot area of cycle  $i$ . We use the maximum of the daily sunspot area to account for the different strength of each cycle, so that stronger cycles will have more ephemeral region flux emerging than weaker cycles. The mean magnetic field strengths for sunspot umbra and penumbra are  $\langle B_{z,u} \rangle = 1800$  G and  $\langle B_{z,p} \rangle = 550$  G, respectively, following Krivova et al. (2007) and according to the measurements of Keppens and Martinez Pillet (1996). Again, we used the ratio of umbral to penumbral area equal to 0.25 following Brandt et al. (1990) and Wenzler et al. (2006). The function  $g_i(t)$  is defined as

$$g_i(t) = \cos^2 \left( \frac{\pi(t - t_i^m + t_x)}{T_i^{eph}} \right), \quad (4.4)$$

for  $t \in [t_i^m - l_i/2 - 2t_x, t_i^m + l_i/2]$ , where  $t_i^m$  is the time at which cycle  $i$  reaches maximum activity and  $l_i$  is the length of the active region cycle. The length of the ephemeral region cycle is related to the length of the active region cycle via a parameter,  $t_x$ , that represents the extension of the ephemeral region cycle in relation to the sunspot cycle,

$$T_i^{eph} = l_i + 2t_x. \quad (4.5)$$

The ephemeral region cycle, therefore, starts around  $2t_x$  years before the first sunspot cycle minimum, and ends during the second active region minimum. The fact that we relate the length and amplitude of the ephemeral region cycle to the corresponding sunspot cycle implies that we are assuming that the ephemeral regions are produced by the global dynamo, like in the case of active regions.

From Eq. 4.1 we obtain the daily total ephemeral region flux on the solar surface, that will be incorporated in the SATIRE-S model. The daily ephemeral region flux is disc integrated, so that we have no information on the location of ephemeral regions on the solar surface, in contrast to sunspots and faculae of which we know their location and area on the solar disc. This assumption is reasonable since ephemeral regions appear everywhere on the solar surface. The prime equation in SATIRE-S, Eq. (1.3), requires the filling factors and the intensity brightness of each component to convert magnetic flux into irradiance. We compute disc integrated filling factors for ephemeral regions,  $f^{er}(t)$ , and we use the corresponding disc integrated intensity (i.e. flux),  $F$ , of the model atmosphere. The latter does not depend on  $\mu = \cos \theta$ , where  $\theta$  is the heliocentric angle. We compute solar irradiance including the flux from ephemeral regions, in the following way

$$\begin{aligned} S(t, \lambda) = \sum_{\mu(i,j)} & \left[ (1 - \alpha_{\mu(i,j)}^f(t) - \alpha_{\mu(i,j)}^u(t) - \alpha_{\mu(i,j)}^p(t)) I_{\mu(i,j)}^q(\lambda) \right. \\ & \left. + \alpha_{\mu(i,j)}^f(t) I_{\mu(i,j)}^f(\lambda) + \alpha_{\mu(i,j)}^u(t) I_{\mu(i,j)}^u(\lambda) + \alpha_{\mu(i,j)}^p(t) I_{\mu(i,j)}^p(\lambda) \right] \\ & + f^{er}(t) F_f(\lambda) - f^{er}(t) F_q(\lambda), \end{aligned} \quad (4.6)$$

where the terms inside the sum are equivalent to those in Eq. (1.3) and give the disc integrated solar irradiance due to faculae, sunspots, and the quiet Sun only. Of the last two terms, the first takes into account the ephemeral regions where we have used the same model atmosphere as for faculae. The last term subtracts the excess in the fraction of the solar surface that is covered by quiet Sun after including the ephemeral regions. The disc integrated filling factors for ephemeral regions,  $f^{er}$ , are calculated in the same way as for the facular filling factors, i.e. equivalent to Eq. (3.12),

$$f^{er} = \begin{cases} B^{eph}/B_{er} & \text{if } B^{eph} < B_{er} \\ 1 & \text{if } B^{eph} \geq B_{er} \end{cases} \quad (4.7)$$

Here  $B^{eph}$  corresponds to the flux density of ephemeral regions, obtained directly by dividing the disc integrated flux  $\mathcal{E}^{eph}$  by the surface area of the Sun.

## 4.4 Results and discussion

### 4.4.1 Fixing the free parameters: $X$ and $t_x$

The model has now 4 free parameters: saturation values for faculae,  $B_f$ , and ephemeral regions,  $B_{er}$ , the scaling factor,  $X$ , and the time extension of the ephemeral region cycle with respect to the active region cycle,  $t_x$ . The two parameters from the modelling of the ephemeral region flux,  $X$  and  $t_x$ , can be estimated by matching the observed total photospheric flux. The saturation values are later constrained by the best fit between the reconstructed and the observed TSI. With the 4 parameters constrained we reconstruct the TSI back to 1878 (Sec.4.5).

Figure 4.3 shows the observed flux density integrated over the whole disc for the past 3 solar cycles. Overplotted are the flux density as calculated by the surface flux transport model (red), the flux density for ephemeral regions (green), and a weighted combination of both (blue). Since the surface flux transport model is missing the flux from ephemeral regions, a combination of both the simulated and the ephemeral region flux should reproduce the observations. However, adding the flux densities is not straightforward. The simulated flux density had to be scaled to match the observations since it doesn't include the flux from the small bipolar regions, and therefore we must take this into account when adding the flux densities. Also, the spatial resolution of the observed images used to calculate the total flux density over the solar disc is not enough to measure all of the ephemeral region flux, missing more than 60% of the existing flux (Krivova and Solanki 2004). We therefore multiply the modelled flux density of the ephemeral regions by a factor in the range 0.3 – 0.4 and the flux simulated using the surface flux transport model by a factor within 0.8 – 0.9. These two factors are not completely independent since their values are linked to the scaling factor  $X$ .

The three panels in Fig. 4.3 show three different combinations of the simulated and ephemeral region flux densities, which also give different values for  $X$  compared with the observations. The time extension parameter of the ephemeral region cycle,  $t_x$ , is fixed to 1 year so that the ephemeral region cycle starts 2 years before the active region cycle. Values of  $t_x = 1.5$  and 2 years result in too extreme values, causing the blue curve to overestimate the observed total flux density during the descending phases of the cycles.

At the same time, if the amplitude scaling factor  $X$  is decreased to match the descending phases, during the minima the total flux density is underestimated. We don't use any kind of fitting algorithm and we choose the best combination of factors by eye. The election of these is not easy as different combinations may retrieve results that satisfy the observations. Three cases are presented in Fig 4.3, where the blue curve fits fairly well the observed values, improving the match with respect to the simulated total flux density (red) during minima and ascending phases. Note that still the blue curve lies below the MWO data during the maximum of cycle 21 and the ascending phase of cycle 23, while it fits well for WSO data. The opposite happens during the maximum of cycle 22 and part of the descending phase of cycle 23.

We have used three different values of the scaling factor,  $X=0.45, 0.5,$  and  $0.6,$  to reconstruct TSI and fix the two saturation values,  $B_f$  and  $B_{er}$ , since although all three give very similar magnetic flux densities this does not imply that the irradiance will be the same, in particular at longer time scales.

#### 4.4.2 Fixing the free parameters: $B_f$ and $B_{er}$

Table 4.1 lists the values of the slope of a linear fit between PMOD and the reconstructions, along with the correlation coefficient,  $r_c$  and the  $\chi^2$  of the fit for different  $B_f$  and  $B_{er}$  values for the 3 different cases with  $X = 0.45, 0.5,$  and  $0.6.$  The parameters are given for both the non smoothed data and for a smoothing of 3 months. Since at the present moment we don't know the strength and duration of sunspot cycle 24, we can not model the ephemeral region cycle 24 and, hence, the fits have been done until the beginning of the year 2004. This way we are not taking into account the period of overlap of the beginning of the ephemeral region cycle 24 and the end of the active region cycle 23. From the values in Table 4.1 we can see that all of the correlation coefficients are very similar, around 0.7 and 0.8. Also, for the values of  $B_f$  and  $B_{er}$  displayed, the slopes are around 0.7 for the non smoothed data and around 0.8 – 0.9 for the smoothed data, except in the case of  $B_f = 450$  G and  $B_{er} = 900$  G where the value of the slopes drops to 0.6. These correlation coefficients are very similar to those listed in Ch. 3, where we reconstructed TSI without the flux from ephemeral regions. The  $\chi^2$  values, however, are significantly lower now ( $\approx 300$  lower) than in the case without ephemeral region flux. A higher saturation value for the ephemeral regions,  $B_{er}$ , while keeping constant the other parameters raises the slope and the  $\chi^2$ . At the same time, a higher saturation value for the faculae,  $B_f$ , while keeping the rest of the parameters fixed lowers the slope and the  $\chi^2$ . Therefore, it is possible to obtain more than one combination of saturation values that give a similar slope and correlation coefficient. For fixed values of  $B_f$  and  $B_{er}$ , the slope, the correlation coefficient and the  $\chi^2$  change very little with  $X$ . The correlation coefficient only varies in the third decimal place, while differences in the slope are seen in the second decimal place.

Fig. 4.4 shows plots for the difference between our reconstruction and the PMOD composite of observations (left panels) and our reconstruction versus PMOD (right panels) for the case without (top) and with (bottom) the flux from ephemeral regions. The plots correspond to the reconstructions with the parameters for which we obtain the best fit with the PMOD, i.e. lowest  $\chi^2$  and slope closest to one. These are  $B_f = 400$  G for the case without ephemeral regions and  $B_f = 450$  G,  $B_{er} = 1000$  G,  $X = 0.45$  and  $t_x = 1$ yr for

the case that includes ephemeral regions. When looking at the difference plots between our reconstruction and the PMOD composite after including the flux from ephemeral regions, we can see that the biggest deviations are found during the maximum of cycle 23, from the year 2000 onwards. From around the year 2000 onwards we also find that the reconstructed total magnetic flux density (blue curve in Fig. 4.3) fits better the data from the WSO, so that if the data from the MWO were correct, our reconstructed flux density would be too small to reproduce cycle 23 correctly. Thus, we calculated the fit parameters for cycles 21 and 22 alone to better constrain the combination of free parameters that best fit the PMOD composite (see Table 4.2). The last column in Table 4.2 marks with an **X** the values chosen for the free parameters that best fit the PMOD composite. Based on the results of Table 4.2 and the smoothed values listed in Table 4.1, we chose the reconstructions for which the slope is in both cases above 0.90 and below 1.05 while keeping the  $\chi^2$  as low as possible ( $< 176$ ). We retrieved two sets of free parameters, (1)  $B_f = 380$  G,  $B_{er} = 800$  G,  $X = 0.5$ ,  $t_x = 1$  yr and (2)  $B_f = 380$  G,  $B_{er} = 1000$  G,  $X = 0.6$ ,  $t_x = 1$  yr. Both cases give almost identical TSI reconstructions for the observed period. The enhanced amplitude scaling in the ephemeral region cycles,  $X$ , in set (2) with respect to set (1) is compensated by a higher value of the saturation parameter for ephemeral regions,  $B_{er}$ . From Fig. 4.4 we can also notice how the results of our TSI reconstructions have improved after including the flux from ephemeral regions in the SATIRE-S model. The difference plot for the reconstruction including the ephemeral regions (bottom) is flatter than for the reconstruction without (top). The improvements are seen mainly in the period of the descending phase of cycle 21 and the minimum between cycles 21 and 22, i.e. between the years 1984 and 1987, and during the descending phase of cycle 22 and the minimum between cycles 22 and 23, i.e. between the years 1994 and 1998. Once we have the set of free parameters fixed to match best the observations from the PMOD composite, we run the model to reconstruct TSI since 1878.

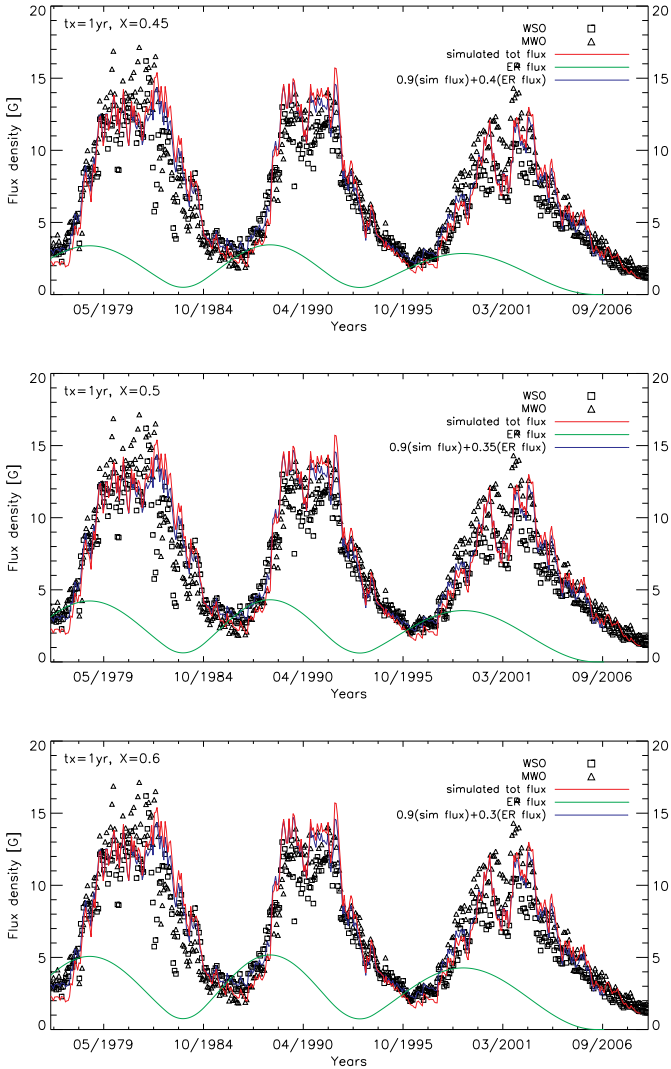


Figure 4.3: The magnetic flux density integrated over the whole solar disc in Gauss. Open squares and triangles represent the measurements by Wilcox Solar observatory (WSO) and Mount Wilson observatory (MWO), respectively. The red curve is the 27 day averaged disc integrated flux density from the simulated synoptic maps, the same in green from the ephemeral regions and the blue curve is a weighted combination of both. The different panels are for different sets of parameters, showing that it is possible to reproduce the observations with different combinations of the free parameters.

Table 4.1: Correlation coefficients ( $r_c$ ), the slope of a linear fit between PMOD and reconstruction along with the  $\chi^2$  of the fit, for different  $B_f$  and  $B_{er}$  values. The **X** and  $\leftarrow$  mark the set of free parameters chosen to best fit the PMOD composite, as described in the text.

$B_f(\text{G}), B_{er}(\text{G})$	$X$	$t_A(\text{yrs})$	no smoothing			90 days smoothing		
			slope	$r_c$	$\chi^2$	slope	$r_c$	$\chi^2$
380, 700	0.45	1	0.776	0.750	1300.1	0.894	0.866	334.3
	0.50	1	0.771	0.748	1297.2	0.883	0.863	335.0
	0.60	1	0.762	0.743	1304.4	0.860	0.853	349.8
380, 800	0.45	1	0.781	0.751	1308.4	0.907	0.868	338.9
	0.50	1	0.777	0.750	1301.4	0.900	0.867	334.9
	0.60	1	0.769	0.747	1297.4	0.877	0.861	337.1
380, 900	0.45	1	0.785	0.752	1318.7	0.917	0.868	346.3
	0.50	1	0.782	0.751	1309.4	0.908	0.868	339.5
	0.60	1	0.774	0.750	1298.6	0.891	0.866	334.1
380, 1000	0.45	1	0.789	0.752	1329.3	0.925	0.867	354.6
	0.50	1	0.785	0.752	1318.7	0.917	0.868	346.3
	0.60	1	0.779	0.751	1303.8	0.901	0.868	336.1
400, 800	0.45	1	0.745	0.745	1239.8	0.824	0.863	292.5
	0.50	1	0.741	0.743	1236.3	0.814	0.861	291.0
	0.60	1	0.733	0.739	1239.1	0.794	0.853	298.2
400, 900	0.45	1	0.749	0.745	1246.7	0.834	0.864	297.4
	0.50	1	0.745	0.745	1240.4	0.825	0.863	292.9
	0.60	1	0.738	0.742	1235.8	0.807	0.859	291.9
400, 1000	0.45	1	0.753	0.746	1254.5	0.842	0.864	303.8
	0.50	1	0.749	0.745	1246.7	0.834	0.864	297.4
	0.60	1	0.743	0.744	1237.3	0.818	0.862	291.2
450, 900	0.45	1	0.673	0.722	1152.5	0.658	0.846	217.5
	0.50	1	0.669	0.720	1152.7	0.649	0.842	217.6
	0.60	1	0.662	0.715	1161.0	0.632	0.830	226.0

Table 4.2: Slope of a linear fit between PMOD and the reconstructions for cycles 21 and 22 alone, along with the correlation coefficient,  $r_c$ , and the  $\chi^2$  of the fit, for different  $B_f$  and  $B_{er}$  values. The **X** and  $\leftarrow$  in the last column mark the same sets of free parameters as in Table 4.1.

$B_f(\text{G}), B_{er}(\text{G})$	$X$ $t_x(\text{yrs})$		90 days smoothing			
			slope	$r_c$	$\chi^2$	
380, 700	0.45	1	1.030	0.926	175.7	
	0.50	1	1.017	0.924	178.7	
	0.60	1	0.990	0.914	194.0	
380, 800	0.45	1	1.045	0.928	176.0	<b>X</b>
	0.50	1	1.033	0.927	175.4	
	0.60	1	1.010	0.922	181.3	
380, 900	0.45	1	1.056	0.928	179.0	
	0.50	1	1.046	0.928	176.2	
	0.60	1	1.025	0.926	176.3	
380, 1000	0.45	1	1.065	0.928	183.1	<b>X</b>
	0.50	1	1.056	0.928	179.0	
	0.60	1	1.038	0.928	175.4	
400, 800	0.45	1	0.947	0.923	155.7	
	0.50	1	0.936	0.921	156.6	
	0.60	1	0.913	0.914	165.5	
400, 900	0.45	1	0.960	0.924	157.2	
	0.50	1	0.949	0.924	155.7	
	0.60	1	0.928	0.928	158.5	
400, 1000	0.45	1	0.968	0.924	160.1	$\leftarrow$
	0.50	1	0.960	0.924	157.2	
	0.60	1	0.941	0.922	155.9	

#### 4.4.3 TSI reconstruction since 1878

In the previous section we fixed the free parameters of our model by comparing the TSI reconstructions with the observations. However, we found that there is more than one combination of values of the free parameters that produces a TSI time series that lies very close to the PMOD composite. We therefore reconstruct TSI back to 1878 for 3 different sets of free parameters. Two of them were discussed in the previous section. A third one (indicated with an arrow in Table 4.1 and Table 4.2) is chosen with a different  $B_f$  value to test how sensitive are the longer term reconstructions to the free parameters. The three set of free parameters are:

1.  $B_f = 380 \text{ G}, B_{er} = 800 \text{ G}, X = 0.5, t_x = 1 \text{ yr}$
2.  $B_f = 380 \text{ G}, B_{er} = 1000 \text{ G}, X = 0.6, t_x = 1 \text{ yr}$
3.  $B_f = 400 \text{ G}, B_{er} = 1000 \text{ G}, X = 0.45, t_x = 1 \text{ yr}.$

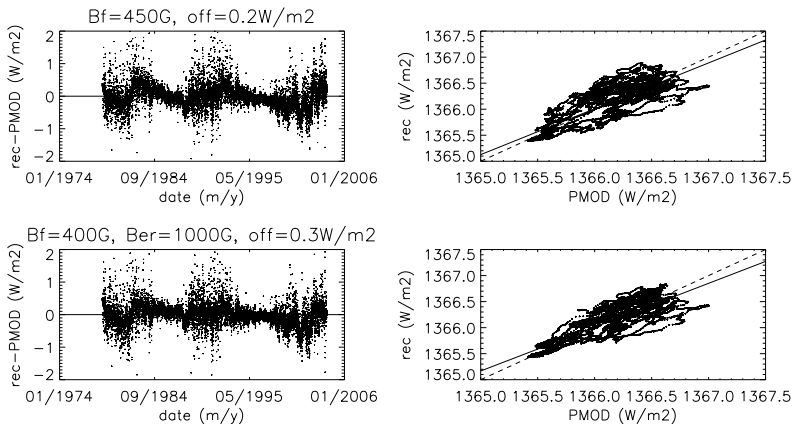


Figure 4.4: Left panels show the differences between our TSI reconstruction and the PMOD composite and the right panels show our reconstructed TSI versus the PMOD composite, before (top) and after (bottom) including the flux from ephemeral regions.

Figure 4.5 plots the reconstructions of TSI since 1878 for the three different sets of parameters together with the PMOD composite of observations where all of the data sets have been smoothed over 1 year. The three reconstructions have been shifted to match the average value of the PMOD composite. Note that although the sunspot area and position data set goes back to 1874, we reconstruct from 1878 onwards. Before cycle 12 we have no information, a priori, on the strength of the sunspot cycles, so that we cannot model the strength of the ephemeral region cycles. For this reason we start in the year 1878, with the onset of cycle 12, even if the sunspot area and position data set starts in 1874. From the comparison between the three reconstructions we can see that the two reconstructions with  $B_f = 380$  G (cases 1 and 2, and blue and green curves, respectively) show very similar results during all of the time period. The reconstructions for cases 1 and 2 are different by  $\Delta B_f = 200$  G in their saturation values of ephemeral regions and by  $\Delta X = 0.1$  in the amplitude scaling factor for the ephemeral region cycles. Case 2 has both a higher  $B_{er}$  and  $X$ , so that the increase in ephemeral region flux via  $X$  is compensated by a higher saturation value of the ephemeral region flux (see Eq. 4.7). Thus, it is the combination of both parameters which is important for the amplitude modulation of the ephemeral region flux in the total irradiance. The cycle amplitudes in the reconstruction with a  $B_f = 400$  G (case 3 and red curve) are smaller than those in the reconstructions with a  $B_f = 380$  G. The amplitude difference is more evident in the earlier cycles, i.e. cycles 12–16. The difference between cases 2 and 3, which share the same saturation value for ephemeral regions, is of  $\Delta B_f = 20$  G and  $\Delta X = -0.15$ . The amplitude difference could thus be due to the weaker ephemeral region flux in case 3, to the stronger saturation value for faculae, or a combination of both. A higher saturation value for faculae diminishes the effect of faculae and a lower amplitude in the ephemeral region cycles produces less ephemeral region flux on the photosphere, so that in total there is less contribution to brightening.

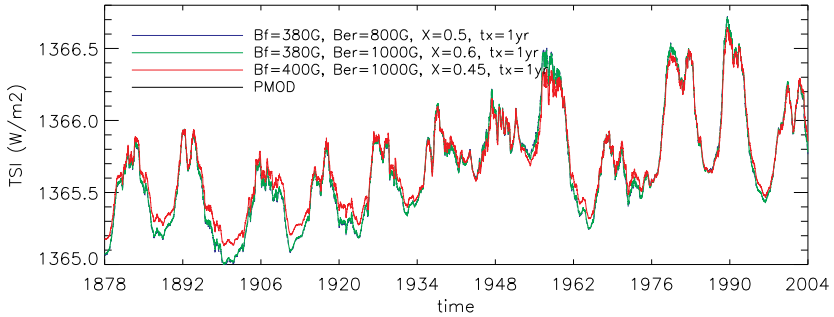


Figure 4.5: TSI reconstructions since 1878 smoothed over 1 year for the three different set of free parameters described in the text along with the 1-year smoothed PMOD composite of observations.

We also compared our TSI reconstruction to those from Krivova et al. (2007) and Wang et al. (2005). Krivova et al. (2007), hereon denoted as K07, reconstructed TSI since the Maunder minimum with a SATIRE-T model (see Sect. 1.3.3). The magnetic flux from faculae and network, sunspots, and ephemeral regions are determined using the model of Solanki et al. (2002a) from the sunspot group number,  $R_g$ , and the Zurich sunspot number,  $R_z$ . The 1-year smoothed reconstructions from K07 are plotted in Fig. 4.6 (dashed and dotted-dashed curves) along with our reconstructions for cases 2 and 3, and the PMOD composite. We did not include the TSI reconstruction for case 1 since it is almost identical to the reconstruction for case 2. Both our reconstructions and those by K07 agree well with the measurements for cycles 21 and 22 but underestimate the TSI of cycle 23 as compared to the PMOD composite. In the comparison we included the TSI reconstructions of K07 both from the sunspot group number,  $R_g$  (dashed), and the Zurich sunspot number,  $R_z$  (dotted-dashed) since the latter presents smaller amplitude variations. The differences between them are basically due to the differences in the sunspot number records. When going back in time, our reconstructions generally show a larger range of variation, both in cycle amplitude and within a cycle. Our reconstructions were expected to be noisier than those by K07 since ours include TSI variations dependent on the position on the solar disc, and are, thus, are more realistic. The cycle amplitudes of our TSI reconstructions are larger than in K07, the only exceptions are cycles 16 and 17 in the K07 reconstruction based on the  $R_z$ .

Quite evident is also the drop during the minimum between cycles 19 and 20 and the relatively weak cycle 19 in our reconstruction, in both the 1-year (Fig. 4.6) and the 11-year (Fig. 4.7) smoothed data. It is striking that the amplitude from the preceding minimum to the maximum of cycle 19 in Fig. 4.6 is roughly the same as for cycles 12 and 13, although these cycles are very different in their activity levels as seen in the sunspot areas (see Fig. 1.4) and sunspot number. The dip after cycle 19 is related to the weak cycle-averaged tilt angle of the sunspot groups of cycle 19. Cycle 19 presents the smallest cycle-averaged

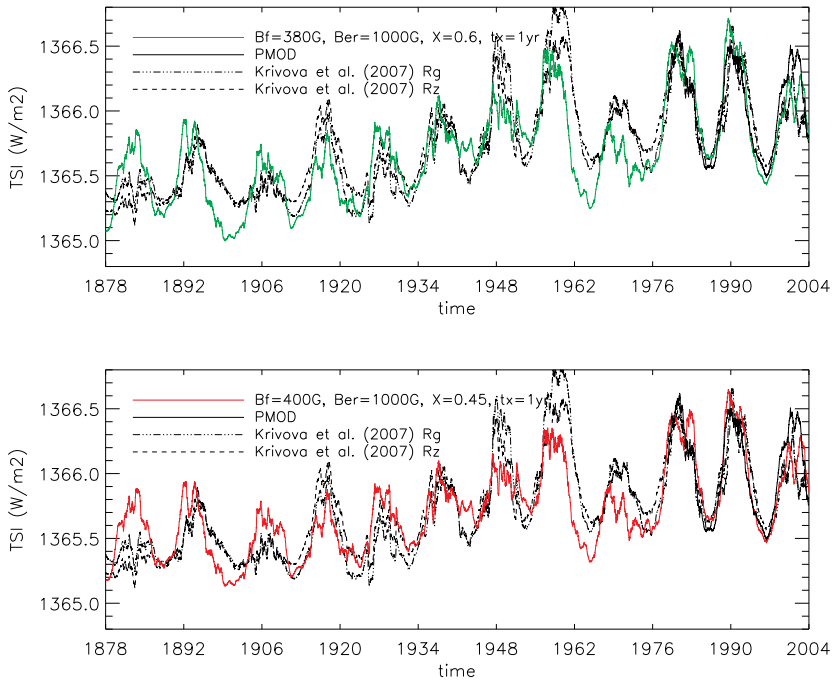


Figure 4.6: TSI reconstructions since 1878 smoothed over 1 year for the set of free parameters 2 (top) and 3 (bottom) described in the text along with the 1-year smoothed TSI reconstructions from Krivova et al. (2007) and the PMOD composite of observations.

tilt angle of cycles 15–21 (see Ch. 2). According to the surface flux transport model, small tilt angles would cause weak polar fields during the minima, since there would be more flux cancellation between the opposite polarity patches of the sunspot groups before the field from these reaches the poles. Low polar fields would be reflected in low total surface flux density and thus in low irradiance values. For the earlier cycles we don't know yet what could be the cause of the differences seen between our reconstructions and those from K07.

The fact that we use a different sunspot to facular area ratio than that employed by K07 could also play a role during the maxima of the TSI cycles. K07 employed a linear relationship, while the surface flux transport model uses a quadratic function as empirically determined by Chapman et al. (1997) (see Sect. 3.2.2). The linear relationship implies that the area coverage by faculae grows linearly with sunspot area. However, a quadratic function tells us that the facular area grows fast with sunspot area until a certain sunspot size from which the facular area increases slowly with increasing sunspot area. The dif-

ference between the functions would be thus more noticeable during periods of maxima, when the largest sunspots are seen. The linear relationship would overestimate the facular component compared to the quadratic function for large sunspots. On the other hand, for cycles with fewer sunspots the effect would be the opposite. The linear relationship would underestimate the facular areas in comparison to the quadratic function. If one looks at the minimum to maximum variations of the TSI cycles in Fig. 4.6, only cycles 15, 18, 19, and 20 have higher amplitudes in the reconstructions from K07 than in our reconstructions. Whether the difference in the ratios used can be reflected in the TSI of weak and strong cycles is not straight forward, since not necessarily the strongest cycles have the biggest sunspots. The strength of a cycle is the total area covered by all sunspots in one cycle so that the result is a combination of sunspot area and sunspot number. Although the size distribution of sunspots is independent of the cycle strength (Bogdan et al. 1988), it has been observed that strong cycles have a tendency to have somewhat larger spots (Solanki and Unruh 2004). A further analysis should be done to understand where the differences come from, taking into account also how other parameters in the surface flux transport model affect the TSI reconstructions like, e.g. meridional flow, tilt angles of sunspot groups and diffusivity.

To study long term trends in the irradiance reconstructions, we did an 11-year smoothing of the data. Figure 4.7 shows our two reconstructions for cases 2 and 3 along with the reconstructions from K07 and the PMOD composite of observations, where all data sets have been smoothed over 11 years and the reconstructions have been shifted to the average level of the PMOD composite. After an 11-year smoothing we still see that the drop in TSI between cycles 19 and 20 (between the years 1962 and 1976) is deeper and starts earlier for our reconstructions. One interesting point to note is that whereas in the reconstruction of K07 the maximum is reached during cycle 19, i.e. around 1960, in our reconstruction it is reached during cycle 22, i.e. around 1990 (see Fig. 4.7). During the observed period, our reconstructed TSI is higher than that from K07 and the PMOD composite, where the reconstruction with  $B_f = 380$  G and  $X = 0.6$  (green curve) gives the highest values. In the period between around 1900 and 1960, the increase in TSI shown by our reconstructions is much smoother, due to the fact that the amplitudes in our cycles are more similar to each other than in the case of K07, so that they are smoothed out after doing the 11-year running means. In spite of these differences, the secular change since 1878 is similar for all reconstructions. From the 11-year smoothed reconstructions, we estimated the increase in TSI as the difference in the average of the first and last 30 years covered by our data sets. This gives a  $\Delta\text{TSI} \approx 0.45 - 0.55$  for our reconstructions and  $\Delta\text{TSI}_{\text{K07}} \approx 0.60 - 0.65$  for those by K07, since 1878, i.e. for this period of time our reconstructions display a roughly 20 % smaller increase in TSI over the last 126 years.

We cannot compare our results with those of Wang et al. (2005) (hereafter W05) as quantitatively as done with those of K07, since at the present moment we don't have the data of their TSI reconstructions. Hence, we describe here in a qualitative manner their method and results as compared to ours. W05 employed a surface flux transport model to obtain the Sun's total and open flux since 1713. From the total flux W05 reconstructed the TSI using an irradiance model based on the one by Lean (2000). Our approach to reconstruct TSI is thus very similar to that from W05 in the sense that we also use a surface flux transport model to compute the photospheric flux from which we extract the facular component of the TSI. Like in our case, they included the flux from ephemeral

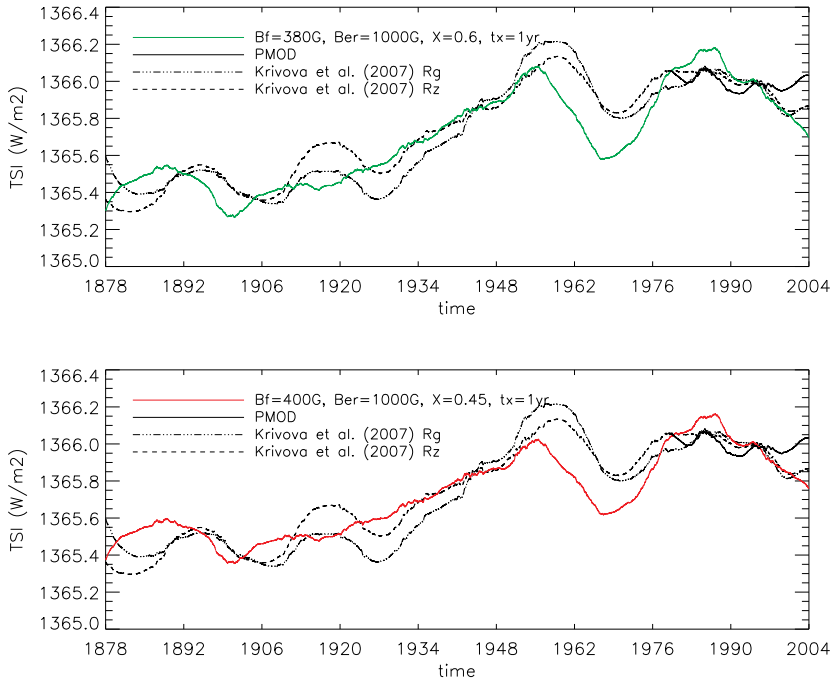


Figure 4.7: TSI reconstructions since 1878 smoothed over 11 years for the set of free parameters 2 (top) and 3 (bottom) described in the text along with the 11-year smoothed TSI reconstructions from Krivova et al. (2007) and the PMOD composite of observations.

regions separately due to the fact that the typical size of the ephemeral regions is below the spatial resolution of their surface flux transport model. Although W05 scale the rate of flux emergence in the ephemeral regions to the total sunspot group number in a cycle, they do not take into account the extension and overlap of the ephemeral region cycles, essential for a larger secular trend in the total magnetic flux (c.f. Solanki et al. 2002b).

Both the irradiance and the surface flux transport model of W05, differ from ours in some aspects. One of the main differences in the surface flux transport model of W05 to the one used here is the source term. Their source term models the active regions of a cycle based on the group sunspot number relative to the properties of solar cycle 21. They simulate the magnetic flux on the solar surface either with a fixed number of active regions of cycle-to-cycle varying strengths or with a cycle-to-cycle varying number of active regions of the same magnetic field strength. In our case, the source term in the surface flux transport model of Cameron et al. (2010) uses the information on the position and area of the sunspot groups from a daily sunspot record. Therefore, the latter approach

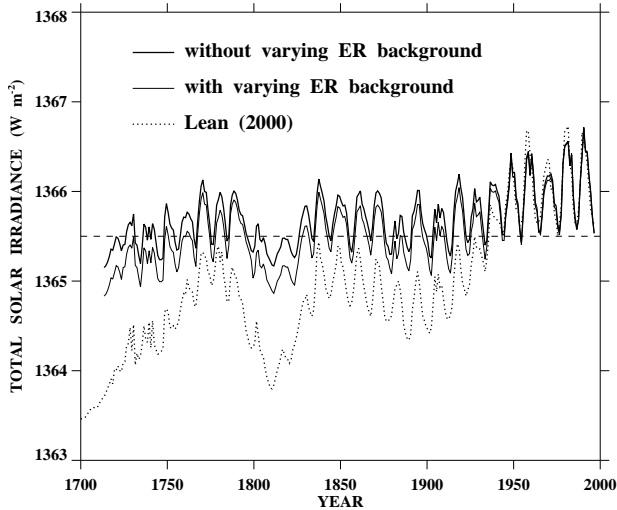


Figure 4.8: Yearly total solar irradiance from Wang et al. (2005) since 1713 with (thin solid curve) and without (thick solid curve) a varying ephemeral region background, and from Lean (2000). The figure corresponds to Fig. 15 from Wang et al. (2005).

is more realistic as it doesn't require assumptions on the varying strengths or the number of active regions in the different solar cycles. Another important difference is the fact that W05 assume a cycle-to-cycle variable meridional flow to maintain the polar field reversals. This is solved by Cameron et al. (2010) by introducing in the source term the observed cycle-to-cycle variation of the sunspot group tilt angles (Dasi-Espuig et al. 2010).

W05 reconstruct the TSI since 1713 to derive a secular trend since the Maunder minimum. The darkening due to sunspots for the period after 1882 is derived from a semi-empirical brightness ratio between sunspots and the quiet Sun. Before 1882, the sunspot darkening is based on a linear regression with the sunspot group numbers. To obtain both the facular component within a cycle and a longer term variation of the facular brightness, their irradiance model makes use of linear regressions between the TSI and the total flux, as obtained from their surface flux transport model. In the SATIRE-S model there is no need to use linear regressions since the irradiance of sunspots, and faculae and network is accounted for via the corresponding model atmospheres. Fig 4.8 (Fig. 15 in W05) shows W05's TSI reconstructions with and without a varying ephemeral region flux. In the figure they also plotted the reconstruction from Lean (2000) as a comparison, although the secular change in her model was taken from the study of Baliunas and Jastrow (1990) using stellar data, whose results were later found to be unreliable (Hall and Lockwood 2004). If we compare the TSI reconstruction of W05 that includes a varying ephemeral region background with ours from Fig. 4.5, we can see that the TSI increase since 1878

predicted by W05 is very similar to that from K07 (around  $0.6 \text{ W m}^{-2}$ ) and 20% higher than ours. However, the prediction of the TSI increase since the Maunder minimum is slightly lower ( $0.3 \text{ W m}^{-2}$  lower) for W05 than for K07. This difference is mainly due to the fact that the total photospheric magnetic flux is higher in the model of Solanki et al. (2002b) used by K07 as a product of the overlapping ephemeral region cycles. If we look at the amplitude of the cycles from the reconstruction of W05, we can see that these are more similar to those of the TSI cycles of K07 than ours, for the earlier cycles. Thus, cycles 12, 14, and 16 present the weakest amplitudes since 1878 both in W05 and K07, while in our case the amplitudes of these cycles are very similar to each other. This could be a consequence of using the sunspot group number to compute the total photospheric flux in both W05 and K07. In contrast, our surface flux transport model uses a record of observed areas and positions of the sunspot groups on the solar surface. Thus, the differences seen in the TSI reconstructions are due, not only to the different TSI models, but already arise from the differences in the magnetic fluxes computed with different surface flux transport models. This, however, needs to be checked by direct comparison between our computed magnetic flux and that from W05 and K07.

Another interesting point is that in W05's reconstruction the maximum amplitude in TSI is reached during cycle 22 like in our reconstruction, and not cycle 19 like in that from K07. This could be also a product of the surface flux transport model, since in our and W05's case the magnetic flux is obtained from the magnetohydrodynamic induction equation, in contrast to K07's case, who use the simple model of Solanki et al. (2002b) based on a set of ordinary differential equations. This is reflected as well in the open flux. The model of Solanki et al. (2002b) underestimates both the total and the open flux during cycle 22 (around the year 1990) as compared to the measurements (Schrijver and Harvey 1994) and the reconstruction from Lockwood et al. (1999), respectively. More interestingly, the reconstructed open flux from Lockwood et al. (1999) is higher during cycle 22 (around year 1990) than cycle 19 (between year 1950 and 1960), opposite to what K07 and Solanki et al. (2002b) obtain. The surface flux transport model used here is compared to the more recent reconstruction of the open flux from Lockwood (2003) in Fig. 4.9. Although the measurements show very similar amplitudes for cycles 19 and 22 (Lockwood 2003, Lockwood et al. 2009a,b), the simulated open flux peaks around 1990, so that cycle 19 is weaker in the surface flux transport model used here. In the case of W05, their open flux does not peak during cycle 22, but rather cycle 19 or 21 depending on whether they vary the number of bipolar regions or their magnetic field strength, respectively. Both TSI reconstructions in Fig. 4.8 (with and without ephemeral region flux) are obtained from the average magnetic flux computed in the two different ways, i.e. varying the number or the strength of the bipolar regions. Hence, the fact that the TSI reconstruction with ephemeral region flux in W05 peaks at cycle 22, but it doesn't peak at cycle 22 in the open flux, in contrast to our results, could be due to differences in the irradiance models.

#### 4.4.4 Relations with total and open flux

The total magnetic flux consists of closed and open fields of which the open field comprises a small fraction. The closed fields consist of all magnetic structures in the form of closed loops. The open field is the part of the total magnetic field that is dragged

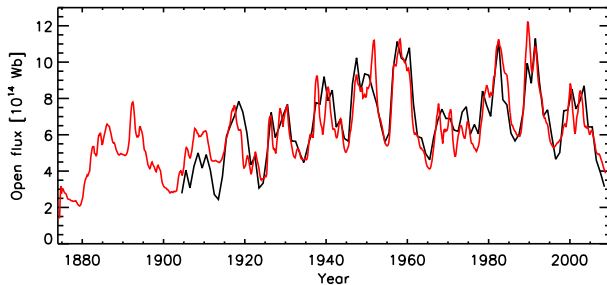


Figure 4.9: Open flux inferred from the aa-index (Lockwood 2003) in black and the simulated open flux from the surface flux transport model used here, in red.

outward by the coronal gases and extends far into the heliosphere. Since the variations of the total irradiance are driven almost entirely by the changing distribution of the magnetic elements on the solar photosphere (dark sunspots and bright faculae and network), we expect it to be strongly associated with the total magnetic flux and the open flux. We therefore searched for relations between the TSI and the total and the open magnetic flux, as previously done by Balmaceda (2007). She used the TSI irradiance reconstructions of K07 and found linear and positive correlations between the TSI and the total magnetic flux density and the open flux. Here we test these relations in our model.

The open flux is obtained as the fraction of the total solar magnetic flux that extends beyond 10 solar radii and is obtained by extrapolating outwards the surface field from the surface flux transport model (Zhao and Hoeksema 1995, Jiang et al. 2011a). The total magnetic flux density is calculated from the sum of the simulated flux density obtained from the surface flux transport model and the modelled ephemeral region flux density. Section 4.4.1 dealt with the different combinations of the total magnetic and the ephemeral region flux densities, where Fig. 4.3 shows three particular cases used in the reconstruction of the TSI. We looked at annual and cycle means of the TSI versus the total flux density and the open flux, to study the relationships both within the solar cycle and from one cycle to another. Figure 4.10 shows these relationships for the reconstructed TSI with the set of free parameters in case 3:  $B_f = 400$  G,  $B_{er} = 1000$  G,  $X = 0.45$ , and  $t_x = 1$  yr. The correlation coefficients for the three cases of reconstructed TSI are listed in Table 4.3. Overall, the correlation coefficients that we obtain are in the range of those found by Balmaceda (2007) from her comparison of the modelled and observed values of total and open flux. From Table 4.3 we can see that the relationships of the TSI reconstructions with both the total magnetic flux density and the open flux, show positive correlations above  $r = 0.87$ . For cycle means, the correlations are  $r \geq 0.94$ . The correlation coefficients for the cycle means are slightly higher between TSI and the open flux. For the annual means, the correlation coefficients show almost no difference whether we look at the total or open flux.

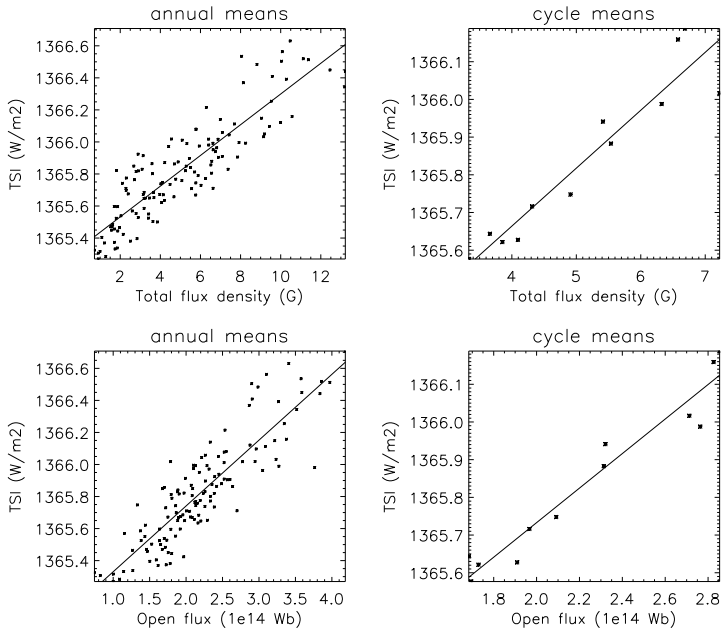


Figure 4.10: Annual and cycle means of TSI versus total magnetic flux density on the solar surface (top panels) and the same versus open flux (bottom panels). The solid lines correspond to a linear fit to the data.

## 4.5 Conclusions

Including the flux from ephemeral regions in the SATIRE-S model have greatly improved the results presented in the previous chapter, where we reconstructed TSI only from the magnetic flux given by the surface flux transport model. The surface flux transport model does not take into account the flux from ephemeral regions due the lack of a continuous and reliable ephemeral region flux record. To include the ephemeral re-

Table 4.3: Correlation coefficients for the annual and cycle means of reconstructed TSI for the three different sets of free parameters and the total magnetic flux density and the open flux.

		case 1	case 2	case 3
TSI vs. Total flux	annual	0.87	0.87	0.89
	cycle	0.96	0.96	0.94
TSI vs. Open flux	annual	0.87	0.87	0.88
	cycle	0.98	0.98	0.97

gion flux we have modelled ephemeral region cycles based on a simplified version of the scheme followed by Solanki et al. (2002b) and Vieira and Solanki (2010). The cyclic variation of the ephemeral regions is dependent on the length and amplitude of the corresponding sunspot cycle, so that we are assuming that the ephemeral regions are produced by the global dynamo as in the case of the sunspots. The fact that the length of the ephemeral region cycles is extended with respect to the sunspot cycle, these being present already 2–3 years before sunspot minima, causes an overlap of the ephemeral region cycles. The overlap introduces a varying magnetic flux background that changes the level of the quiet Sun, leading to a secular change in the total solar magnetic flux and thus, the irradiance. As a consequence to the secular trend in the solar irradiance, the solar forcing on the Earth’s atmosphere will change with time. The larger the magnitude of this change, the more relevant the solar forcing variations are likely to be for climate change studies.

Including the flux from ephemeral regions introduces 3 more free parameters in our model. Two of these,  $X$  and  $t_x$ , are related to the properties of the ephemeral region cycle, where  $t_x$  is the extension of the ephemeral region cycle with respect to the corresponding sunspot cycle, and  $X$  is an amplitude scaling factor. The third additional parameter is a disc integrated saturation value,  $B_{er}$ , for ephemeral regions. The free parameters  $X$  and  $t_x$  are estimated by fitting the observed total photospheric magnetic flux density of cycles 21–23, where  $t_x$  is kept in the range between 1–2 years, i.e. the ephemeral region cycle starts 2–4 years before sunspot minima as suggested by observations (Harvey and Martin 1973, Harvey 1992, Hagenaar 2001). The saturation values for faculae and ephemeral regions are obtained from the best match to the PMOD composite of TSI measurements in the years 1978–2004. We don’t consider the irradiance from the year 2004 onwards since we don’t model the ephemeral region cycle 24 as its parameters (length, time of maximum and amplitude) are unknown. Figure 4.4 shows that the differences between the PMOD composite and the reconstructed TSI are improved after including the flux from ephemeral regions, in particular during the descending phases and times of minima. Table 4.1 and Table 4.2 list the slope, correlation coefficient  $r_c$ , and the  $\chi^2$  of the fit between the PMOD composite and the reconstructed TSI for different values of the free parameters  $B_f$ ,  $B_{er}$  and  $X$  for cycles 21–23 and only 21–22, respectively. We chose to reconstruct the TSI using three different values of  $X$  since there is no unique value to fit the total photospheric magnetic flux density. Tables 4.1 and 4.2 mark with an **X** the two chosen reconstructions that best fit the observations according to our criteria. These are selected so that, in both tables, the slope is between 0.9 and 1.05 while keeping the  $\chi^2$  below 176.

With the free parameters of our model fixed at the values obtained by fitting the PMOD composite, we have reconstructed the TSI back to 1878. We employed the set of parameters that correspond to the two best fits of the TSI and included an additional one with a different  $B_f$  value to test the sensitivity of our model to the free parameters, when reconstructing back in time. Cases 1 and 2, with free parameters  $B_f = 380$  G,  $B_{er} = 800$  G,  $X = 0.5$ ,  $t_x = 1$  yr and  $B_f = 380$  G,  $B_{er} = 1000$  G,  $X = 0.6$ ,  $t_x = 1$  yr respectively, produce almost identical TSI reconstructions. Case 3, with free parameters  $B_f = 400$  G,  $B_{er} = 1000$  G,  $X = 0.45$ ,  $t_x = 1$  yr, shows less amplitude variation in the TSI cycles than the other two cases (see Fig. 4.5). This is due to the higher saturation value for faculae and/or to the lower amplitude scaling factor of the ephemeral region flux, so that  $X$  and  $B_{er}$  are not completely independent. The brightening due to faculae is diminished with increasing saturation value for faculae and the brightening due to ephemeral regions is

less when the amplitude of the ephemeral region cycle is lowered since the amount of ephemeral region flux available is less.

We further compared our reconstructions since 1878 with those from Krivova et al. (2007) (K07) and, qualitatively to those from Wang et al. (2005) (W05). K07 reconstructed TSI since 1610 from the sunspot group number and from the Zurich sunspot number using the SATIRE-T model. The comparison is shown in Fig. 4.6 for our reconstructions in cases 2 and 3. From the comparison we can point out three striking features: (1) our reconstructions differ from those by K07 before cycle 21, although they both predict a similar total solar irradiance increase since 1878 (within roughly 20% of each other), as seen in Fig. 4.7. (2) Our reconstructions show larger amplitude variation in the TSI cycles, (3) our reconstructions show a prominent drop at the time of the minimum between cycles 19 and 20, and (4) cycle 19 is not the strongest in terms of TSI in our reconstructions, where cycle 22 displays higher TSI values. The fact that K07 use a linear relation between the facular and sunspot areas in contrast to the quadratic function used in our surface flux transport model could be reflected during the maxima and partly explain the bigger amplitude variation in our reconstructed TSI. The prominent drop after cycle 19 can be explained by the low cycle averaged tilt angle of sunspot groups, since a low tilt angle causes low polar fields at minima and thus low total surface flux and irradiance. However, more tests should be done to investigate how sensitive our reconstructions are to the parameters in the surface flux transport model like meridional flow, tilt angle, and diffusivity.

Our approach is similar to that from W05 since we also make use of a surface flux transport model to compute the photospheric magnetic flux from which we reconstruct the TSI. However, both the surface flux transport model and the irradiance model used here are different in some aspects. The main differences in the surface flux transport models are, (1) that the one used here uses the information on the sunspot areas and positions to derive the source term in the induction equation, while the one from W05 models the sunspot cycles based on the sunspot group number and the properties of solar cycle 21. (2) That the surface flux transport model from W05 assumes a variable meridional flow while the one we employ includes the observed cycle-to-cycle variation of the sunspot group tilt angles. The latter is therefore more realistic. The TSI reconstruction from W05 also includes the flux from ephemeral regions, but they do not model the overlap of their cycles and thus obtain a smaller secular increase in the total photospheric flux than Solanki et al. (2002b) and K07. The differences seen in the TSI between our reconstructions, those from K07, and those from W05 are due to a combination of the differences in the computed photospheric magnetic flux and the irradiance models. The irradiance model from W05 is based on the one by Lean (2000), where the darkening and brightening due to sunspots and faculae are retrieved from linear regressions with the sunspot group number and the total flux, respectively. In our case the brightness contrast of each component is given by a corresponding model atmospheres dependent on the position to the disc center, and hence, do not rely on linear regressions.

From the comparison between the TSI reconstructions of W05, K07, and ours, we point out that (1) the early weak cycles in K07 (12, 14, and 16) are also weak in W05, but not in our, where the cycle amplitudes are more similar to each other. This difference could be due to the fact that K07 and W05 make use of the sunspot group number to calculate the total photospheric flux, while the surface flux transport model we employ

is based on the record of sunspot positions and areas. (2) The maximum amplitude in TSI occurs during cycle 22 in the reconstruction of W05 and ours, but during cycle 19 in the reconstruction of K07. This is also reflected in the open flux. The open flux computed with the surface flux transport model used here peaks during cycle 22, while that computed by K07 peaks during cycle 19. The open flux in W05 peaks at cycle 19 or 22 depending on whether the authors vary the strength or the number of the bipolar regions in their surface flux transport model. Thus, the differences in the TSI could also be due to the different TSI models. (3) The secular change since 1878 is similar for both K07 and W05, and around 20% higher than in our case.

Lastly, we tested the relationships between the TSI and the total surface magnetic field as well as between the TSI and the open flux. The correlation coefficients are summarized in Table 4.3 and Fig. 4.10. We find strong positive correlations between the annual means and cycle means of the TSI versus total surface and open magnetic flux, close to those found by Balmaceda (2007). This finding supports the validity of such global relations as found by Balmaceda et al. (2007) and Vieira et al. (2011) in the simpler model of K07, which underlies the reconstruction of TSI over the whole Holocene.



## 5 Conclusions and outlook

In this dissertation we have studied two challenging aspects related to the Sun-Earth connection: a new proxy for the prediction of future solar activity and an improved and more realistic method for the modelling of past solar irradiance variations.

Concerning future solar activity, we focused on the prediction of the strength and amplitude of the sunspot cycles, which can give a quantitative measure of the amount of fast processes like flares and coronal mass ejections, that occur during sunspot maxima. These fast processes release energetic particles that can reach the Earth's atmosphere and affect our natural environment, e.g. space weather. Our approach in predicting the amplitude and strength of the sunspot cycles is based on the Babcock-Leighton idea for the dynamo operating in the solar interior. Thus, our work also concerns the physics behind the solar dynamo and helps to constrain it. We analysed sunspot data from the Mount Wilson and the Kodaikanal observatories, which cover approximately 70 years of observations and which include the measurements of the tilt angles of sunspot groups. We studied the cycle-to-cycle relationship between the tilt angles and three solar cycle parameters, namely, the strength, the amplitude and the length. The main findings of the analysis show that the mean tilt angle of all sunspot groups in a cycle, normalized by the mean latitude, i.e. Joy's law, varies from one cycle to the next. We also found that the cycle averaged and normalized tilt angle is strongly anti-correlated with the strength of the same cycle. Since the strength of a cycle can be inferred from the sunspot number, this relationship can be useful to estimate the average tilt angle of sunspot cycles back to times when there are no measurements of the sunspot group positions and areas.

More interestingly, a tilt angle expression based on the Babcock-Leighton dynamo mechanism was found to be positively correlated with the amplitude of the next cycle. This enables us to forecast the amplitude of a cycle from the tilt angles, positions, and areas of the sunspot groups of the previous cycle, with a reasonable accuracy (correlation coefficients  $r = 0.79$  and  $r = 0.78$  based on the Mount Wilson and the Kodaikanal data respectively). Their accuracy is comparable to methods based on precursors. Our prediction has the advantage that it can be made around 10 years before sunspot maxima, much earlier than with other methods. Unfortunately, the data sets from Mount Wilson and Kodaikanal observatories go until the end of cycle 21, so that we cannot predict the amplitude of the sunspot cycle 24 unless we use a different data set. We plan to extend the analysis to cycles 22 and 23 by using the sunspot data set from the Debrecen Photoheliographic Data. Figure 5.1 shows the preliminary tilt angle measurements from the Heliophysical Observatory in Debrecen, Hungary, kindly provided by Tunde Baranyi<sup>1</sup>. The tilt angle measurements from the Heliophysical Observatory were carefully done following the def-

---

<sup>1</sup>The data can be downloaded at <http://fenyi.sci.klte.hu/DPD/index.html>

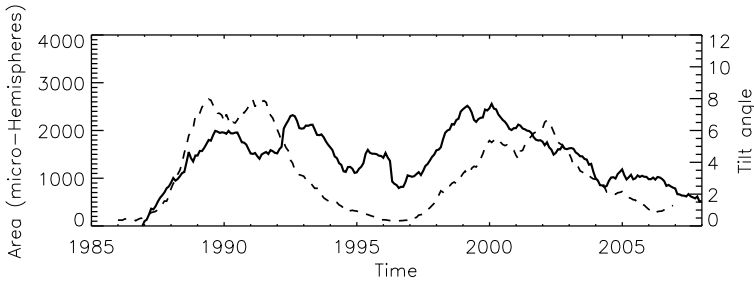


Figure 5.1: Dashed line and left-hand Y-axis shows the monthly means of sunspot area from Balmaceda et al. (2009) vs. time, smoothed over 12 months. Solid line and right-hand Y-axis shows monthly area-weighted means of sunspot tilt angle smoothed over 48 months.

Table 5.1: Area-weighted mean tilt angles in degrees for each cycle for the Mount Wilson (MW), the Kodaikanal (KK), and the Debrecen Photoheliographic (DEB) records.

Cycle	MW $\pm 1\sigma$	KK $\pm 1\sigma$	DEB $\pm 1\sigma$
15	$5.69 \pm 0.57$	$5.00 \pm 0.50$	-
16	$5.08 \pm 0.46$	$5.91 \pm 0.43$	-
17	$5.83 \pm 0.42$	$6.41 \pm 0.41$	-
18	$5.69 \pm 0.35$	$4.97 \pm 0.38$	-
19	$3.84 \pm 0.33$	$4.59 \pm 0.38$	-
20	$4.63 \pm 0.38$	$5.73 \pm 0.36$	-
21	$5.30 \pm 0.40$	$5.37 \pm 0.42$	-
22	-	-	$6.07 \pm 0.21$
23	-	-	$5.50 \pm 0.22$

initiation and method from Howard et al. (1984), Howard (1991). Both Y-axes have been scaled to those from Fig. 2.2(a) to show that the values of the sunspot group tilt angles are within the range of those from the Mount Wilson and Kodaikanal data sets. The large tilt angles observed at the end of cycle 22, between the years 1994 and 1997, are however not consistent with the combination of the butterfly diagram and Joy's law. According to these combination, one would expect the tilt angles to be larger at the start of a cycle, when the sunspot groups are found at higher latitudes, and smaller at the end of the cycles when the groups are found close to the equator. The data for the years 1990 – 1992 are still preliminary and incomplete, so that the value of the tilt angles during this period could change. The overlap of the Debrecen Photoheliographic data and the Kodaikanal data set during the year 1986 made possible the identification of the same sunspot groups in both data sets by Tunde Baranyi (private communication). The Debrecen Photoheliographic data for the year 1986 is final and complete. Fig. 5.2 plots the comparison between the tilt angle measurements of each observatory for the same sunspot groups. Only the points

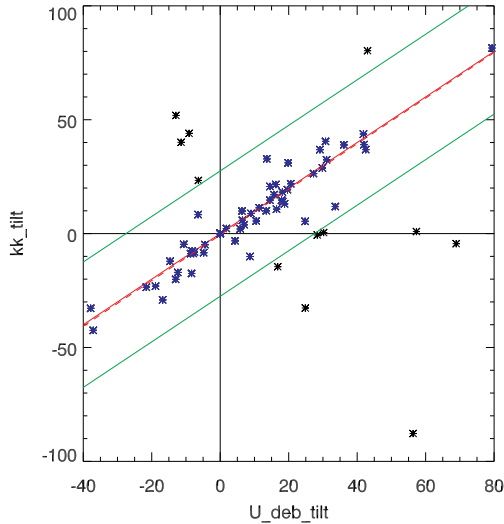


Figure 5.2: Tilt angle based on Kodaikanal (KK) data versus the tilt angle of the same sunspot group based on Debrecen (Deb) data. The red solid line is a line with slope equal to 1 passing through the origin and the green lines correspond to  $(y - \sigma) = x$  and  $(y + \sigma) = x$ , where  $\sigma$  is the standard deviation of the KK tilt angles. The red dashed line is a fit to the points within one sigma of the  $y = x$  line (blue).

within  $1\sigma$  of the  $y = x$  line (blue points within the green lines) were considered when calculating a linear fit. The fit is  $y = (1.00 \pm 0.03)x - (0.61 \pm 0.56)$  (red dashed line) with a correlation coefficient of  $r = 0.95$ . We have included these preliminary measurements in the analysis done in Ch. 2 for the Kodaikanal data. Table 5.1 is equivalent to Table 2.1 where we have added the average area-weighted tilt angles from the Debrecen Photoheliographic data. We can see that the average area-weighted tilt angle for cycle 22 is among the highest together with cycles 16 and 17 from the Kodaikanal data set. For cycle 23, the average area-weighted tilt angle lies in the middle of the whole range of values.

We proceeded to include the sunspot data of cycles 22 and 23 in the relationships concerning the average tilt angle and the strength of the cycles for the Kodaikanal data. Figure 5.3(a) shows the linear relationship between the cycle averaged tilt angle normalized by the mean latitude (or Joy's law) and the strength of the same cycle, where the values for cycles 22 and 23 have been added in red. The correlation coefficient after adding the last two cycles has lowered from  $r = -0.93$  to  $r = -0.85$ . Although the error bars for the data points for cycles 22 and 23 are not within the linear fit, the points follow the observed negative trend. Figure 5.3(b) plots the strength of a cycle multiplied by the area-weighted and normalized tilt angle versus the strength of the next cycle, where cycle

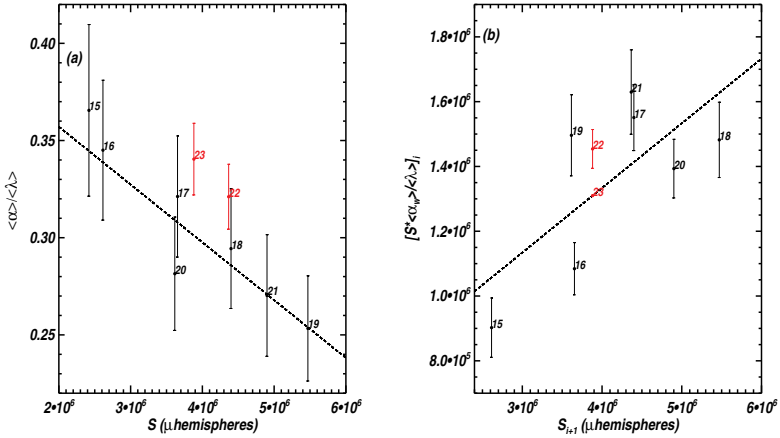


Figure 5.3: (a) Cycle averaged tilt angle normalised by the mean latitude ( $\langle \alpha \rangle / \langle \lambda \rangle$ ) vs. the strength ( $S$ ) of the same cycle and (b) strength of cycle multiplied by mean normalised area-weighted tilt angle ( $[S^i \langle \alpha_i \rangle / \langle \lambda_i \rangle]$ ) vs. the strength of the next cycle ( $S_{i+1}$ ), for the Kodaikanal data (black) and the Debrecen data (red). The cycle number is indicated next to each data point, the error bars are  $1\sigma$  standard error and the dashed line is a linear fit to the points.

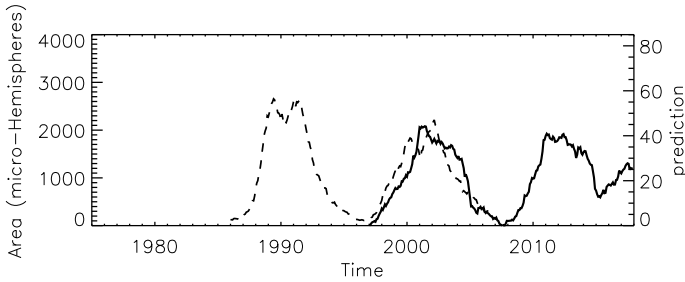


Figure 5.4: Monthly means of sunspot area smoothed over 12 months from Balmaceda et al. (2009) (dashed line) and predicted monthly means of sunspot area smoothed over 48 months from the Debrecen data (solid line).

22 has been included in red. With the parameters of the linear fit (dashed line) and the preliminary sunspot data from cycle 23, we predict that the strength of solar cycle 24 is very close to that of cycle 23. A similar result is found when looking at the running means of the tilt angle expression based on the Babcock-Leighton idea. Figure 5.4 is equivalent to Fig. 2.6 in Ch.2, but for cycles 22 and 23 only. The Y-axes have been scaled as for

Fig. 2.6 for reference so that, with the same scale, the amplitude (maximum of monthly means of sunspot area) of cycle 23 is reproduced very well by our prediction (solid curve). Extending the prediction to cycle 24 gives an amplitude of around  $40 \mu\text{Hemispheres}$ , very similar to cycle 23. It is important to point out that we are not predicting the timing of the solar maxima nor minima and thus the maximum of cycle 24 around the years 2011–2012 should not be considered.

W. D. Pesnell collated a list of predictions for the maximum sunspot number,  $R_z$ , of cycle 24 along with the sources and the method used by each author<sup>2</sup>. The whole range of predictions is very broad, with  $R_z = 40 - 180$ . The extreme values are comparable to the weakest cycle since the Maunder minimum, cycle 6, and to the strongest, cycle 19. If we focus on the predictions done with flux transport dynamo models based on the Babcock-Leighton mechanism we find two very different values. The scheme developed by Dikpati and Gilman (2006) forecasts a maximum sunspot number of 80, i.e. close to that for cycle 16, while Choudhuri et al. (2007) predicts it in a range from 155 – 180, i.e. close to that for cycle 19. In our case we are not predicting maximum sunspot number but maximum sunspot area or the total area covered by all sunspots in one cycle. Our prediction places the strength of cycle 24 to similar values as that of cycle 23 and thus would fall between the two dynamo-based predictions. However, note that this study is done with preliminary data that still needs completion and revision in some of the years, so that the results could change.

The observed cycle-to-cycle variation of Joy’s law found in our study has been incorporated by Cameron et al. (2010) in a surface flux transport model developed by Baumann (2005) based on sunspot positions and areas, to model the evolution of the magnetic fields on the solar surface. Taking into account the variation of the tilt angles turned out to solve the problem of needing a global diffusive term to reproduce correctly the open flux and the polar field reversal times. Here we employed the model from Cameron et al. (2010) to simulate the magnetic field in the photosphere since 1874. The only difference to their work is that, instead of the measured tilt angles, here we use the observed linear fit between cycle strength and cycle averaged and normalized tilt angle to compute the cycle mean tilt angle. This gives a better match to the open flux, mainly during the minimum between solar cycles 19 and 20.

In this thesis we used the daily simulated surface field, i.e. simulated magnetograms, to reconstruct total solar irradiance with the SATIRE-S model. One of the advantages of using the simulated magnetograms is that we are able to reconstruct solar irradiance back to times when there are no magnetogram measurements to account for the facular component. Reconstructing irradiance with the SATIRE-S model should be more accurate than with the SATIRE-T model since SATIRE-S uses the spatial information of the magnetic features. Also, the surface flux transport model is a more physics-based approach to obtain the photospheric magnetic flux for times when only sunspot positions, areas, or number is available. Our total solar irradiance reconstructions for the period of observations show that we can only obtain a good match with the PMOD composite of observations if we include the flux from ephemeral regions. The surface flux transport model includes the magnetic flux of sunspots, and faculae and network, but not of the

<sup>2</sup><http://www.swpc.noaa.gov/SolarCycle/SC24/index.html>

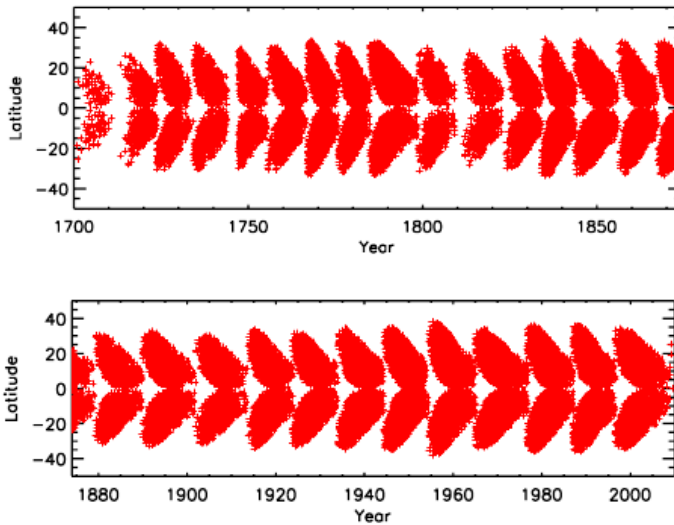


Figure 5.5: Reconstructed butterfly diagrams for the years 1700–1874 (top) and 1874–2010 (bottom) from Jiang et al. (2011b), using the group sunspot number.

small bipolar regions because of insufficient spatial resolution in the model and because there are no continuous records of ephemeral regions available covering a considerable amount of time. Therefore, we modelled the ephemeral region cycles based on the properties derived in the extensive study of Harvey and Martin (1973), Harvey (1992) and the scheme followed by Solanki et al. (2002b), Vieira and Solanki (2010). This scheme assumes that the ephemeral region flux is a product of the global dynamo, like in the case of sunspots, and faculae and network, so that if there is any small scale field produced by a local dynamo on the solar surface we are not taking it into account. Ephemeral regions present cycles like those of sunspots and have been observed to appear 2 to 3 years before sunspot minimum, hence the effect of including their flux in the total solar irradiance reconstructions is mostly seen during the minima and ascending phases of the irradiance cycles. The disadvantage with respect to the SATIRE-S model in which the flux from ephemeral regions is included directly from its presence in magnetograms (but which is missing in the surface flux transport computations, since these only include flux from active regions, containing sunspots) is that we have 4 free parameters instead of 1. One additional free parameter concerns the saturation value and the other two the modelling of the ephemeral regions. To remove the two free parameters that define the time extension and amplitude of the ephemeral region cycles more continuous observational studies must be done for periods of time longer than one solar cycle.

The clear improvement of the total solar irradiance reconstructions after including the flux from ephemeral regions led us to reconstruct it back to 1878. Since the selection of

the set of free parameters that better match the PMOD composite of observations proved not to be unique, we built three reconstructions with three different sets of free parameters. The reconstructions deviate mostly from each other during the earlier cycles, i.e. 12–15. It is difficult to say exactly which of these reconstructions is superior to the others, since, for the period covered by the PMOD, cycles 21 and 22 were very similar in their maximum sunspot numbers, sunspot areas, and irradiance values, and cycle 23 is reconstructed only until the year 2004. We reconstruct only until the year 2004 since we lack the parameters of solar cycle 24 necessary to model the corresponding ephemeral region flux to include it in the SATIRE-S model. A comparison with the total solar irradiance reconstructions from Krivova et al. (2007) and from Wang et al. (2005) shows that the secular change since 1878 is around 20% lower in our case. A closer inspection shows that the amplitudes of our irradiance cycles are in general larger and more similar to each other. This is mainly seen in cycles 12, 14, and 16 (Fig. 4.6 and Fig. 4.8). In the reconstructions from Krivova et al. (2007) and Wang et al. (2005) these appear among the weakest cycles since 1878, which is consistent with the low maximum sunspot numbers. This is, however, not that obviously reflected in the sunspot areas. Both the fact that the reconstructions of total and open flux from Krivova et al. (2007) and Wang et al. (2005) are based on the sunspot number, and that Krivova et al. (2007) use a different sunspot to facular area relationship than in the surface flux transport model we use, could be playing a role. Thus, the differences seen between the three total solar irradiance reconstructions could be due to a combined effect of the differences in the computation of the photospheric magnetic flux and the different irradiance models. To investigate where the differences come from, we would like to further do a cycle-to-cycle analysis of the reconstructed total solar irradiance and its relationship with the sunspot number, the sunspot area, and total magnetic flux. The analysis could also relate the differences in the irradiance cycles with other properties of the solar cycles.

Our total solar irradiance reconstructions go back to 1878, so that as a next step we are interested in extending them back to the Maunder minimum to estimate the solar forcing, given its importance for climate studies. Jiang et al. (2011b) reconstructed the butterfly diagram since 1700 from a statistical study of the sunspot cycle properties and the sunspot number (see Fig. 5.5). The reconstructed butterfly diagram was used by Jiang et al. (2011a) together with the surface flux transport model from Cameron et al. (2010) to study the long term evolution of the Sun's magnetic field. Therefore, the reconstruction of total solar irradiance since 1700 would be an obvious and direct step. Yet another obvious step would be to reconstruct the spectral solar irradiance, since its variation in the UV part of the spectrum, between 100 nm and 400 nm, can be more than 50% and several mechanisms are currently under study through which the solar UV radiation could play a major role in the chemistry of the Earth's atmosphere (e.g. Haigh 2007).



# A Determining the cycle-to-cycle variations in the presence of a large intrinsic scatter

As has been mentioned, the tilt angles of individual active regions are largely random, with Joy's law being a relatively small bias. The purpose of this appendix is to discuss the calculation of cycle-to-cycle changes in Joy's law from the data. For this purpose we will assume that Joy's law applies for each cycle and that the scatter in the data is random and unbiased. More explicitly we assume

1. the tilt angle,  $\alpha_i$ , for each spot,  $i$ , obeys Joy's law

$$\alpha_i = a_n \lambda_i + \epsilon_i \quad (\text{A.1})$$

where  $a_n$  is the (possibly cycle-to-cycle dependent) constant of proportionality for cycle  $n$  and  $\epsilon_i$  represents the random deviation from Joy's law of individual sunspot groups.

2. The  $\epsilon_i$  are independent realisations of a random process with a mean of zero.

We calculate our estimate,  $b_n$ , of  $a_n$  for each cycle according to

$$b_n = \frac{\sum_i \alpha_i}{\sum_i \lambda_i} \quad (\text{A.2})$$

where the sum is again over spots in cycle  $n$ . The error of the approximation is

$$b_n - a_n = e_n = \frac{\sum_i \epsilon_i}{\sum_i \lambda_i}. \quad (\text{A.3})$$

We also consider  $\bar{a}$ , the value of  $a$  based on the whole data set, ignoring cycle-to-cycle changes in  $a$ . The equivalent estimate,  $\bar{b}$  of  $\bar{a}$  has the summation extended to all cycles. Note that we could have also considered the cycle-to-cycle deviation of Joy's law,  $d_n$ , from the estimate obtained over all cycles  $\bar{b}$ . This however has exactly the same error as does  $a_n$  as can easily be seen:

$$d_n = \frac{\sum_i \alpha_i - \bar{b} \lambda_i}{\sum_i \lambda_i} \quad (\text{A.4})$$

$$d_n = \frac{\sum_i a \lambda_i + \epsilon_i - \bar{b} \lambda_i}{\sum_i \lambda_i} \quad (\text{A.5})$$

$$d_n = a - \bar{b} + \frac{\sum_i \epsilon_i}{\sum_i \lambda_i} \quad (\text{A.6})$$

$$d_n = a_n - \bar{b} + e_n \quad (\text{A.7})$$

## A Determining the cycle-to-cycle variations in the presence of a large intrinsic scatter

This result indicates that calculating the cycle-to-cycle deviations from a reference Joy's law is identical to calculating Joy's law for each cycle and then subtracting a fixed constant. A similar result can be shown if  $\epsilon_i$  is assumed to be dependent on the area, as was considered in the main text.

# Bibliography

- Antia, H. M., 2003, Does the Sun Shrink with Increasing Magnetic Activity?, *ApJ*, 590, 567–572
- Arge, C. N., Hildner, E., Pizzo, V. J., Harvey, J. W., 2002, Two solar cycles of nonincreasing magnetic flux, *J. Geophys. Res.*, 107, 1319
- Babcock, H. W., 1961, The Topology of the Sun's Magnetic Field and the 22-YEAR Cycle., *ApJ*, 133, 572
- Baldner, C. S., Basu, S., 2008, Solar Cycle Related Changes at the Base of the Convection Zone, *ApJ*, 686, 1349–1361
- Baliunas, S., Jastrow, R., 1990, Evidence for long-term brightness changes of solar-type stars, *Nature*, 348, 520–523
- Ball, W. T., Unruh, Y. C., Krivova, N. A., Solanki, S., Harder, J. W., 2011, Solar irradiance variability: a six-year comparison between SORCE observations and the SATIRE model, *A&A*, 530, A71
- Balmaceda, L., Krivova, N. A., Solanki, S. K., 2007, Reconstruction of solar irradiance using the Group sunspot number, *Adv. Sp. Res.*, 40, 986–989
- Balmaceda, L. A., 2007, Solar Variability and solar irradiance reconstructions on time scales of decades to centuries, Ph.D. thesis, International Max-Planck Research School on Physical Processes in the Solar System and Beyond, Technische Universität Carolo-Wilhelmina zu Braunschweig
- Balmaceda, L. A., Solanki, S. K., Krivova, N. A., Foster, S., 2009, A homogeneous database of sunspot areas covering more than 130 years, *J. Geophys. Res.*, 114, A07 104
- Basu, S., Antia, H. M., 2003, Changes in Solar Dynamics from 1995 to 2002, *ApJ*, 585, 553–565
- Baumann, I., 2005, Magnetic Flux Transport on the Sun, Ph.D. thesis, International Max-Planck Research School on Physical Processes in the Solar System and Beyond, Universität Göttingen
- Baumann, I., Schmitt, D., Schüssler, M., Solanki, S. K., 2004, Evolution of the large-scale magnetic field on the solar surface: A parameter study, *A&A*, 426, 1075–1091

- Baumann, I., Schmitt, D., Schüssler, M., 2006, A necessary extension of the surface flux transport model, *A&A*, 446, 307–314
- Beer, J., 2000, Long-term indirect indices of solar variability, *Space Sci. Rev.*, 94, 53–66
- Beer, J., Blinov, A., Bonani, G., Hofmann, H. J., Finkel, R. C., 1990, Use of Be-10 in polar ice to trace the 11-year cycle of solar activity, *Nature*, 347, 164–166
- Bogdan, T. J., Gilman, P. A., Lerche, I., Howard, R., 1988, Distribution of sunspot umbral areas - 1917-1982, *ApJ*, 327, 451–456
- Brajša, R., Wöhl, H., Hanslmeier, A., Verbanac, G., Ruždjak, D., Cliver, E., Svalgaard, L., Roth, M., 2009, On solar cycle predictions and reconstructions, *A&A*, 496, 855–861
- Brandt, P. N., Schmidt, W., Steinegger, M., 1990, On the umbra-penumbra area ratio of sunspots, *Sol. Phys.*, 129, 191–194
- Brown, G. M., 1976, What determines sunspot maximum, *MNRAS*, 174, 185–189
- Caligari, P., Moreno-Insertis, F., Schüssler, M., 1995, Emerging flux tubes in the solar convection zone. 1: Asymmetry, tilt, and emergence latitude, *ApJ*, 441, 886–902
- Cameron, R., Schüssler, M., 2007, Solar Cycle Prediction Using Precursors and Flux Transport Models, *ApJ*, 659, 801–811
- Cameron, R. H., Jiang, J., Schmitt, D., Schüssler, M., 2010, Surface Flux Transport Modeling for Solar Cycles 15-21: Effects of Cycle-Dependent Tilt Angles of Sunspot Groups, *ApJ*, 719, 264–270
- Chapman, G. A., Cookson, A. M., Dobias, J. J., 1997, Solar Variability and the Relation of Facular to Sunspot Areas during Solar Cycle 22, *ApJ*, 482, 541–545
- Charbonneau, P., 2005, Dynamo Models of the Solar Cycle, *Living Rev. Sol. Phys.*, 2, 2
- Charbonneau, P., 2007, Babcock Leighton models of the solar cycle: Questions and issues, *Adv. Sp. Res.*, 39, 1661–1669
- Charbonneau, P., 2010, Dynamo Models of the Solar Cycle, *Living Rev. Sol. Phys.*, 7, 3
- Charbonneau, P., Dikpati, M., 2000, Stochastic Fluctuations in a Babcock-Leighton Model of the Solar Cycle, *ApJ*, 543, 1027–1043
- Chatterjee, P., Nandy, D., Choudhuri, A. R., 2004, Full-sphere simulations of a circulation-dominated solar dynamo: Exploring the parity issue, *A&A*, 427, 1019–1030
- Choudhuri, A. R., Schüssler, M., Dikpati, M., 1995, The solar dynamo with meridional circulation., *A&A*, 303, L29
- Choudhuri, A. R., Chatterjee, P., Jiang, J., 2007, Predicting Solar Cycle 24 With a Solar Dynamo Model, *Phys. Rev. Lett.*, 98, 131–103

- Crouch, A. D., Charbonneau, P., Beaubien, G., Paquin-Ricard, D., 2008, A Model for the Total Solar Irradiance Based on Active Region Decay, *ApJ*, 677, 723–741
- Danilovic, S., Schüssler, M., Solanki, S. K., 2010, Probing quiet Sun magnetism using MURaM simulations and Hinode/SP results: support for a local dynamo, *A&A*, 513, A1
- Dasi-Espuig, M., Solanki, S. K., Krivova, N. A., Cameron, R., Peñuela, T., 2010, Sunspot group tilt angles and the strength of the solar cycle, *A&A*, 518, A7
- Dewitte, S., Crommelynck, D., Mekaoui, S., Joukoff, A., 2004, Measurement and Uncertainty of the Long-Term Total Solar Irradiance Trend, *Sol. Phys.*, 224, 209–216
- Dickinson, R. E., 1975, Solar variability and the lower atmosphere., *Bull. Am. Meteorol. Soc.*, 56, 1240–1248
- Dikpati, M., Gilman, P. A., 2006, Simulating and Predicting Solar Cycles Using a Flux-Transport Dynamo, *ApJ*, 649, 498–514
- Dikpati, M., Gilman, P. A., 2008, Global solar dynamo models: Simulations and predictions, *JApA*, 29, 29–39
- Dikpati, M., Gilman, P. A., 2009, Flux-Transport Solar Dynamos, *Space Sci. Rev.*, 144, 67–75
- Dikpati, M., de Toma, G., Gilman, P. A., 2006, Predicting the strength of solar cycle 24 using a flux-transport dynamo-based tool, *Geophys. Res. Lett.*, 33, L05 102
- Dikpati, M., de Toma, G., Gilman, P. A., 2008, Polar Flux, Cross-equatorial Flux, and Dynamo-generated Tachocline Toroidal Flux as Predictors of Solar Cycles, *ApJ*, 675, 920–930
- Domingo, V., Ermolli, I., Fox, P., Fröhlich, C., Haberreiter, M., Krivova, N., Kopp, G., Schmutz, W., Solanki, S. K., Spruit, H. C., Unruh, Y., Vögler, A., 2009, Solar Surface Magnetism and Irradiance on Time Scales from Days to the 11-Year Cycle, *Space Sci. Rev.*, 145, 337–380
- Donnelly, R. F., Heath, D. F., Lean, J. L., Rottman, G. J., 1983, Differences in the temporal variations of solar UV flux, 10.7-cm solar radio flux, sunspot number, and Ca-K plage data caused by solar rotation and active region evolution, *J. Geophys. Res.*, 88, 9883–9888
- D’Silva, S., Choudhuri, A. R., 1993, A theoretical model for tilts of bipolar magnetic regions, *A&A*, 272, 621
- D’Silva, S., Howard, R. F., 1993, Limits on the magnetic field strength at the base of the solar convection zone, *Sol. Phys.*, 148, 1–9
- Eddy, J. A., 1976, The Maunder Minimum, *Science*, 192, 1189–1202

- Ermolli, I., Criscuoli, S., Uitenbroek, H., Giorgi, F., Rast, M. P., Solanki, S. K., 2010, Radiative emission of solar features in the Ca II K line: comparison of measurements and models, *A&A*, 523, A55
- Fan, Y., Fisher, G. H., McClymont, A. N., 1994, Dynamics of emerging active region flux loops, *ApJ*, 436, 907–928
- Feynman, J., 1982, Geomagnetic and solar wind cycles, 1900-1975, *J. Geophys. Res.*, 87, 6153–6162
- Feynman, J., Fougere, P. F., 1984, Eighty-eight year periodicity in solar-terrestrial phenomena confirmed, *J. Geophys. Res.*, 89, 3023–3027
- Fligge, M., Solanki, S. K., Unruh, Y. C., 2000, Modelling irradiance variations from the surface distribution of the solar magnetic field, *A&A*, 353, 380–388
- Fontenla, J., Harder, G., 2005, Physical modeling of spectral irradiance variations, *Mem. Soc. Astron. Italiana*, 76, 826
- Fontenla, J., White, O. R., Fox, P. A., Avrett, E. H., Kurucz, R. L., 1999, Calculation of Solar Irradiances. I. Synthesis of the Solar Spectrum, *ApJ*, 518, 480–499
- Fontenla, J. M., Avrett, E. H., Loeser, R., 1993, Energy balance in the solar transition region. III - Helium emission in hydrostatic, constant-abundance models with diffusion, *ApJ*, 406, 319–345
- Foster, S. S., 2004, Reconstruction of solar irradiance variations, for use in studies of global climate change: Application of recent SoHO observations with historic data from the Greenwich observations, Ph.D. thesis, Ph.D dissertation, 2004. England: University of Southampton (United Kingdom); 2004. Publication Number: AAT C820450. DAI-C 66/02, p. 430, Summer 2005
- Foukal, P., Fowler, L., 1984, A photometric study of heat flow at the solar photosphere, *ApJ*, 281, 442–454
- Foukal, P., Lean, J., 1988, Magnetic modulation of solar luminosity by photospheric activity, *ApJ*, 328, 347–357
- Fröhlich, C., 2000, Observations of Irradiance Variations, *Space Sci. Rev.*, 94, 15–24
- Fröhlich, C., 2003, Solar irradiance variations, in *Solar Variability as an Input to the Earth's Environment*, (Ed.) A. Wilson, vol. 535 of ESA Special Publication, pp. 183–193
- Fröhlich, C., 2006, Solar Irradiance Variability Since 1978. Revision of the PMOD Composite during Solar Cycle 21, *Space Sci. Rev.*, 125, 53–65
- Fröhlich, C., 2009a, Evidence of a long-term trend in total solar irradiance, *A&A*, 501, L27–L30

- Fröhlich, C., 2009b, Total solar irradiance variability: What have we learned about its variability from the record of the last three solar cycles?, in *Climate and Weather of the Sun-Earth System (CAWSES): Selected Papers from the 2007 Kyoto Symposium*, October 23-27, 2007, (Ed.) T. Tsuda, R.Fujii, K.Shibata, M.Geller, Terra Publishing, Tokio, pp. 217–230
- Gilman, P., 1986, The solar dynamo: Observations and theories of solar convection, global circulation, and magnetic fields, in *Physics of the Sun*, Vol. 1: The Solar Interior, (Eds.) P. Sturrock, T. Holzer, D. Mihalas, R. Ulrich, vol. 1, pp. 95–160, D. Reidel, Dordrecht, Netherlands; Boston, U.S.A.
- Gilman, P. A., 2002, Observational constraints on the solar dynamo, in *From Solar Min to Max: Half a Solar Cycle with SOHO*, (Ed.) A. Wilson, vol. 508 of ESA Special Publication, pp. 25–32
- Gizon, L., Rempel, M., 2008, Observation and Modeling of the Solar-Cycle Variation of the Meridional Flow, *Sol. Phys.*, 251, 241–250
- Gleissberg, W., 1939, A long-periodic fluctuation of the sun-spot numbers, *The Observatory*, 62, 158–159
- Gnevyshev, M., Ohl, A., 1948, On the 22-year cycle of solar activity, *Astron. Zh.*, 25, 18–20
- Hagenaar, H. J., 2001, Ephemeral Regions on a Sequence of Full-Disk Michelson Doppler Imager Magnetograms, *ApJ*, 555, 448–461
- Hagenaar, H. J., Schrijver, C. J., Title, A. M., 2003, The Properties of Small Magnetic Regions on the Solar Surface and the Implications for the Solar Dynamo(s), *ApJ*, 584, 1107–1119
- Haigh, J. D., 1994, The role of stratospheric ozone in modulating the solar radiative forcing of climate, *Nature*, 370, 544–546
- Haigh, J. D., 2004, *The Earth's Climate and Its Response to Solar Variability*, in *The Sun, Solar Analogs and the Climate*, (Ed.) Springer, Saas-Fee Advanced Course 34, pp. 1–109
- Haigh, J. D., 2007, *The Sun and the Earth's Climate*, *Living Rev. Sol. Phys.*, 4, 2
- Hale, G. E., Nicholson, S. B., 1925, The Law of Sun-Spot Polarity, *ApJ*, 62, 270
- Hale, G. E., Ellerman, F., Nicholson, S. B., Joy, A. H., 1919, The Magnetic Polarity of Sun-Spots, *ApJ*, 49, 153
- Hall, J. C., Lockwood, G. W., 2004, The Chromospheric Activity and Variability of Cycling and Flat Activity Solar-Analog Stars, *ApJ*, 614, 942–946
- Harvey, K. L., 1992, The Cyclic Behavior of Solar Activity, in *The Solar Cycle*, (Ed.) K. L. Harvey, vol. 27 of ASP Conference Series, p. 335

- Harvey, K. L., 2001, Solar Active Regions: Ephemeral, in *Encyclopedia of Astronomy and Astrophysics*, Nature Publishing Group
- Harvey, K. L., Martin, S. F., 1973, Ephemeral Active Regions, *Sol. Phys.*, 32, 389–402
- Hathaway, D. H., 2009, Solar Cycle Forecasting, *Space Sci. Rev.*, 144, 401–412
- Hathaway, D. H., 2010, The Solar Cycle, *Living Rev. Sol. Phys.*, 7, 1
- Hathaway, D. H., Rightmire, L., 2010, Variations in the Sun's Meridional Flow over a Solar Cycle, *Science*, 327, 1350
- Hathaway, D. H., Wilson, R. M., Reichmann, E. J., 1994, The shape of the sunspot cycle, *Sol. Phys.*, 151, 177–190
- Hathaway, D. H., Wilson, R. M., Reichmann, E. J., 1999, A Synthesis of Solar Cycle Prediction Techniques, *J. Geophys. Res.*, 104, 22 375
- Herschel, W., 1801, Observations Tending to Investigate the Nature of the Sun, in Order to Find the Causes or Symptoms of Its Variable Emission of Light and Heat; With Remarks on the Use That May Possibly be Drawn from Solar Observations, *Royal Society of London Philosophical Transactions Series I*, 91, 265–318
- Hiremath, K., 2008, Prediction of solar cycle 24 and beyond, *Astrophys. Space Sci.*, 314, 45–49
- Howard, R., Labonte, B. J., 1980, The sun is observed to be a torsional oscillator with a period of 11 years, *ApJ*, 239, L33–L36
- Howard, R. F., 1991, Axial tilt angles of sunspot groups, *Sol. Phys.*, 136, 251–262
- Howard, R. F., 1993, Axial tilt angles of active regions and their polarity separations, *Sol. Phys.*, 145, 105–109
- Howard, R. F., 1996, Axial Tilt Angles of Active Regions, *Sol. Phys.*, 169, 293–301
- Howard, R. F., Gilman, P. I., Gilman, P. A., 1984, Rotation of the sun measured from Mount Wilson white-light images, *ApJ*, 283, 373–384
- Hoyt, D. V., Schatten, K. H., 1993, A discussion of plausible solar irradiance variations, 1700-1992, *J. Geophys. Res.*, 98, 18 895
- Hoyt, D. V., Schatten, K. H., 1998, Group Sunspot Numbers: A New Solar Activity Reconstruction, *Sol. Phys.*, 181, 491–512
- IPCC, 2007, *Climate Change 2007: The Physical Science Basis. Contribution of Working Group I to the Fourth Assessment Report of the Intergovernmental Panel on Climate Change*, Cambridge University Press, Cambridge, U.K.; New York, U.S.A.
- Jiang, J., Chatterjee, P., Choudhuri, A. R., 2007, Solar activity forecast with a dynamo model, *MNRAS*, 381, 1527–1542

- Jiang, J., Cameron, R., Schmitt, D., Schüssler, M., 2010a, Modeling the Sun's Open Magnetic Flux and the Heliospheric Current Sheet, *ApJ*, 709, 301–307
- Jiang, J., İşik, E., Cameron, R. H., Schmitt, D., Schüssler, M., 2010b, The Effect of Activity-related Meridional Flow Modulation on the Strength of the Solar Polar Magnetic Field, *ApJ*, 717, 597–602
- Jiang, J., Cameron, R. H., Schmitt, D., Schüssler, M., 2011a, The solar magnetic field since 1700. II. Physical reconstruction of total, polar and open flux, *A&A*, 528, A83
- Jiang, J., Cameron, R. H., Schmitt, D., Schüssler, M., 2011b, The solar magnetic field since 1700. I. Characteristics of sunspot group emergence and reconstruction of the butterfly diagram, *A&A*, 528, A82
- Jungclaus, J., Zanchettin, D., Lorenz, S., 2010a, Solar influence on climate in ensemble simulations of the last millennium, in 38th COSPAR Scientific Assembly, vol. 38 of COSPAR, Plenary Meeting, p. 20
- Jungclaus, J. H., Lorenz, S. J., Timmreck, C., Reick, C. H., Brovkin, V., Six, K., Segsneider, J., Giorgetta, M. A., Crowley, T. J., Pongratz, J., Krivova, N. A., Vieira, L. E., Solanki, S. K., Klocke, D., Botzet, M., Esch, M., Gayler, V., Haak, H., Raddatz, T. J., Roeckner, E., Schnur, R., Widmann, H., Claussen, M., Stevens, B., Marotzke, J., 2010b, Climate and carbon-cycle variability over the last millennium, *Climate of the Past Discussions*, 6, 1009–1044
- Keppens, R., 2000, Sunspot Pores in *Encyclopedia of Astronomy and Astrophysics*, Inst. of Physics Publishing, London
- Keppens, R., Martinez Pillet, V., 1996, The magnetic structure of pores and sunspots derived from Advanced Stokes Polarimeter data., *A&A*, 316, 229–242
- Knölker, M., Schüssler, M., 1988, Model calculations of magnetic flux tubes. IV - Convective energy transport and the nature of intermediate size flux concentrations, *A&A*, 202, 275–283
- Komm, R. W., Howard, R. F., Harvey, J. W., 1993, Meridional Flow of Small Photospheric Magnetic Features, *Sol. Phys.*, 147, 207–223
- Krivova, N. A., Solanki, S. K., 2004, Effect of spatial resolution on estimating the Sun's magnetic flux, *A&A*, 417, 1125–1132
- Krivova, N. A., Solanki, S. K., 2008, Models of solar irradiance variations: Current status, *J. Astrophys. Astron.*, 29, 151–158
- Krivova, N. A., Solanki, S. K., Fligge, M., Unruh, Y. C., 2003, Reconstruction of solar irradiance variations in cycle 23: Is solar surface magnetism the cause?, *A&A*, 399, L1–L4
- Krivova, N. A., Balmaceda, L., Solanki, S. K., 2007, Reconstruction of solar total irradiance since 1700 from the surface magnetic flux, *A&A*, 467, 335–346

- Krivova, N. A., Solanki, S. K., Wenzler, T., 2009, ACRIM-gap and total solar irradiance revisited: Is there a secular trend between 1986 and 1996?, *Geophys. Res. Lett.*, 36, L20101
- Krivova, N. A., Vieira, L. E. A., Solanki, S. K., 2010, Reconstruction of solar spectral irradiance since the Maunder minimum, *J. Geophys. Res.*, 115, A12112
- Krivova, N. A., Solanki, S. K., Schmutz, W., 2011a, Solar total irradiance in cycle 23, *A&A*, 529, A81
- Krivova, N. A., Solanki, S. K., Unruh, Y. C., 2011b, Towards a long-term record of solar total and spectral irradiance, *J. Atmos. Solar-Terr. Phys.*, 73, 223–234
- Kurucz, R. L., 1991, New Opacity Calculations, in NATO ASIC Proc. 341: Stellar Atmospheres - Beyond Classical Models, p. 441
- Kurucz, R. L., 1992, Remaining Line Opacity Problems for the Solar Spectrum, *Rev. Mexicana Astron. Astrofis.*, 23, 187
- Lagg, A., Solanki, S. K., Riethmüller, T. L., Martínez Pillet, V., Schüssler, M., Hirzberger, J., Feller, A., Borrero, J. M., Schmidt, W., del Toro Iniesta, J. C., Bonet, J. A., Barthol, P., Berkefeld, T., Domingo, V., Gandorfer, A., Knölker, M., Title, A. M., 2010, Fully Resolved Quiet-Sun Magnetic flux Tube Observed with the SUNRISE/IMAX Instrument, *ApJ*, 723, L164–L168
- Lean, J., 2000, Evolution of the Sun's spectral irradiance since the Maunder Minimum, *Geophys. Res. Lett.*, 27, 2425–2428
- Lean, J., Beer, J., Bradley, R., 1995, Reconstruction of solar irradiance since 1610: Implications for climate change, *Geophys. Res. Lett.*, 22, 3195–3198
- Lean, J. L., Cook, J., Marquette, W., Johannesson, A., 1998, Magnetic Sources of the Solar Irradiance Cycle, *ApJ*, 492, 390
- Leighton, R. B., 1969, A Magneto-Kinematic Model of the Solar Cycle, *ApJ*, 156, 1
- Livingston, W., Harvey, J., 1971, The Kitt Peak Magnetograph. Iv: 40-CHANNEL Probe and the Detection of Weak Photospheric Fields, in *Solar Magnetic Fields*, (Ed.) R. Howard, vol. 43 of IAU Symposium, p. 51
- Livingston, W. C., Harvey, J., 1975, A New Component of Solar Magnetism - The Inner Network Fields, in *BAAS*, vol. 7, p. 346
- Lockwood, M., 2003, Twenty-three cycles of changing open solar magnetic flux, *J. Geophys. Res.*, 108, 1128
- Lockwood, M., Stamper, R., Wild, M. N., 1999, A doubling of the Sun's coronal magnetic field during the past 100 years, *Nature*, 399, 437–439
- Lockwood, M., Owens, M., Rouillard, A. P., 2009a, Excess open solar magnetic flux from satellite data: 1. Analysis of the third perihelion Ulysses pass, *J. Geophys. Res.*, 114, A11103

- Lockwood, M., Owens, M., Rouillard, A. P., 2009b, Excess open solar magnetic flux from satellite data: 2. A survey of kinematic effects, *J. Geophys. Res.*, 114, A11 104
- Makarov, V. I., Makarova, V. V., Sivaraman, K. R., 1989, Do polar faculae on the sun predict a sunspot cycle?, *Sol. Phys.*, 119, 45–54
- Marsh, N. D., Svensmark, H., 2000, Low Cloud Properties Influenced by Cosmic Rays, *Phys. Rev. Lett.*, 85, 5004–5007
- Martinez Pillet, V., Lites, B. W., Skumanich, A., 1997, Active Region Magnetic Fields. I. Plage Fields, *ApJ*, 474, 810
- Ohl, A., 1966, Forecast of sunspot maximum number of cycle 20, *Soln. Dannya*, p. 84
- Ortiz, A., Solanki, S. K., Domingo, V., Fligge, M., Sanahuja, B., 2002, On the intensity contrast of solar photospheric faculae and network elements, *A&A*, 388, 1036–1047
- Parker, E. N., 1979, Sunspots and the physics of magnetic flux tubes. I - The general nature of the sunspot. II - Aerodynamic drag, *ApJ*, 230, 905–923
- Peristykh, A. N., Damon, P. E., 2003, Persistence of the Gleissberg 88-year solar cycle over the last ~12,000years: Evidence from cosmogenic isotopes, *J. Geophys. Res.*, 108, 1003
- Petrovay, K., 2010, Solar Cycle Prediction, *Living Rev. Sol. Phys.*, 7, 6
- Randel, W. J., Wu, F., 2007, A stratospheric ozone profile data set for 1979-2005: Variability, trends, and comparisons with column ozone data, *J. Geophys. Res.*, 112, D06313
- Rempel, M., 2006, Flux-Transport Dynamos with Lorentz Force Feedback on Differential Rotation and Meridional Flow: Saturation Mechanism and Torsional Oscillations, *ApJ*, 647, 662–675
- Rempel, M., 2008, Solar and stellar activity cycles, *J. Phys. Conf. Ser.*, 118, 012032
- Rempel, M., Schüssler, M., 2001, Intensification of Magnetic Fields by Conversion of Potential Energy, *ApJ*, 552, L171–L174
- Schatten, K. H., Scherrer, P. H., Svalgaard, L., Wilcox, J. M., 1978, Using dynamo theory to predict the sunspot number during solar cycle 21, *Geophys. Res. Lett.*, 5, 411–414
- Schrijver, C. J., Harvey, K. L., 1994, The photospheric magnetic flux budget, *Sol. Phys.*, 150, 1–18
- Schrijver, C. J., Title, A. M., Harvey, K. L., Sheeley, N. R., Wang, Y., van den Oord, G. H. J., Shine, R. A., Tarbell, T. D., Hurlburt, N. E., 1998, Large-scale coronal heating by the small-scale magnetic field of the Sun, *Nature*, 394, 152–154
- Schrijver, C. J., DeRosa, M. L., Title, A. M., 2002, What Is Missing from Our Understanding of Long-Term Solar and Heliospheric Activity?, *ApJ*, 577, 1006–1012

- Schrijver, C. J., Livingston, W. C., Woods, T. N., Mewaldt, R. A., 2011, The minimal solar activity in 2008-2009 and its implications for long-term climate modeling, *Geophys. Res. Lett.*, 38, L06701
- Schüssler, M., Baumann, I., 2006, Modeling the Sun's open magnetic flux, *A&A*, 459, 945–953
- Schüssler, M., Caligari, P., Ferriz-Mas, A., Moreno-Insertis, F., 1994, Instability and eruption of magnetic flux tubes in the solar convection zone, *A&A*, 281, L69–L72
- Shapiro, A. I., Schmutz, W., Rozanov, E., Schoell, M., Haberreiter, M., Shapiro, A. V., Nyeki, S., 2011, A new approach to the long-term reconstruction of the solar irradiance leads to large historical solar forcing, *A&A*, 529, A67
- Simon, G. W., Title, A. M., Topka, K. P., Tarbell, T. D., Shine, R. A., Ferguson, S. H., Zirin, H., SOUP Team, 1988, On the relation between photospheric flow fields and the magnetic field distribution on the solar surface, *ApJ*, 327, 964–967
- Sivaraman, K. R., Gupta, S. S., Howard, R. F., 1993, Measurement of Kodaikanal white-light images. I - A comparison of 35 years of Kodaikanal and Mount Wilson sunspot data, *Sol. Phys.*, 146, 27–47
- Sivaraman, K. R., Gupta, S. S., Howard, R. F., 1999, Measurement of Kodaikanal white-light images - IV. Axial Tilt Angles of Sunspot Groups, *Sol. Phys.*, 189, 69–83
- Sivaraman, K. R., Gokhale, M. H., Sivaraman, H., Gupta, S. S., Howard, R. F., 2007, Measurement of Kodaikanal White-Light Images: Relaxation of Tilts of Spot Groups as Indicator of Subsurface Dynamics of Parent Flux Loops, *ApJ*, 657, 592–599
- Sofia, S., Li, L. H., 2004, Solar Variability Caused by Structural Changes of the Convection Zone, in *Solar Variability and its Effects on Climate*. Geophysical Monograph 141, (Ed.) J. M. Pap, P. Fox, C. Frohlich, H. S. Hudson, J. Kuhn, J. McCormack, G. North, W. Sprigg, & S. T. Wu, vol. 141 of Washington DC American Geophysical Union Geophysical Monograph Series, p. 15
- Solanki, S., Krivova, N., 2009, Faculae and Plague, in *Landolt-Börnstein - Group VI Astronomy and Astrophysics Numerical Data and Functional Relationships in Science and Technology Volume 4B: Solar System*. Edited by J.E. Trümper, 2009, 4.1.2.4., p. 4124
- Solanki, S. K., 1993, Smallscale Solar Magnetic Fields - an Overview, *Space Sci. Rev.*, 63, 1–188
- Solanki, S. K., 1997, Empirical Modelling and Thermal Structure of Sunspots, in *1st Advances in Solar Physics Euroconference*. *Advances in Physics of Sunspots*, (Ed.) B. Schmieder, J. C. del Toro Iniesta, & M. Vazquez, vol. 118 of ASP Conference Series, p. 178

- Solanki, S. K., 1998, Solar Magnetic Fields: an Introduction, in *Space Solar Physics: Theoretical and Observational Issues in the Context of the SOHO Mission*, (Ed.) J. C. Vial, K. Bocchialini, & P. Boumier, vol. 507 of *Lecture Notes in Physics*, Berlin Springer Verlag, p. 41
- Solanki, S. K., Krivova, N. A., 2003, Can solar variability explain global warming since 1970?, *J. Geophys. Res.*, 108, 1200
- Solanki, S. K., Krivova, N. A., 2004, Solar Irradiance Variations: From Current Measurements to Long-Term Estimates, *Sol. Phys.*, 224, 197–208
- Solanki, S. K., Schmidt, H. U., 1993, Are sunspot penumbrae deep or shallow?, *A&A*, 267, 287–291
- Solanki, S. K., Stenflo, J. O., 1984, Properties of solar magnetic fluxtubes as revealed by Fe I lines, *A&A*, 140, 185–198
- Solanki, S. K., Unruh, Y. C., 2004, Spot sizes on Sun-like stars, *MNRAS*, 348, 307–315
- Solanki, S. K., Schüssler, M., Fligge, M., 2000, Evolution of the Sun's large-scale magnetic field since the Maunder minimum, *Nature*, 408, 445–447
- Solanki, S. K., Krivova, N. A., Schüssler, M., Fligge, M., 2002a, Search for a relationship between solar cycle amplitude and length, *A&A*, 396, 1029–1035
- Solanki, S. K., Schüssler, M., Fligge, M., 2002b, Secular variation of the Sun's magnetic flux, *A&A*, 383, 706–712
- Solanki, S. K., Seleznyov, A. D., Krivova, N. A., 2003, Solar irradiance fluctuations on short timescales, in *Solar Variability as an Input to the Earth's Environment*, (Ed.) A. Wilson, vol. 535 of *ESA Special Publication*, pp. 285–288
- Solanki, S. K., Usoskin, I. G., Kromer, B., Schüssler, M., Beer, J., 2004, Unusual activity of the Sun during recent decades compared to the previous 11,000 years, *Nature*, 431, 1084–1087
- Solanki, S. K., Inhester, B., Schüssler, M., 2006, The solar magnetic field, *Reports on Progress in Physics*, 69, 563–668
- Solanki, S. K., Wenzler, T., Schmitt, D., 2008, Moments of the latitudinal dependence of the sunspot cycle: a new diagnostic of dynamo models, *A&A*, 483, 623–632
- Solanki, S. K., Barthol, P., Danilovic, S., Feller, A., Gandorfer, A., Hirzberger, J., Riethmüller, T. L., Schüssler, M., Bonet, J. A., Martínez Pillet, V., del Toro Iniesta, J. C., Domingo, V., Palacios, J., Knölker, M., Bello González, N., Berkefeld, T., Franz, M., Schmidt, W., Title, A. M., 2010, SUNRISE: Instrument, Mission, Data, and First Results, *ApJ*, 723, L127–L133
- Spruit, H. C., 1976, Pressure equilibrium and energy balance of small photospheric flux-tubes, *Sol. Phys.*, 50, 269–295

- Spruit, H. C., 2003, Origin of the torsional oscillation pattern of solar rotation, *Sol. Phys.*, 213, 1–21
- Spruit, H. C., Roberts, B., 1983, Magnetic flux tubes on the sun, *Nature*, 304, 401–406
- Steiner, O., 2004, Understanding facular granules and lanes, in *Multi-Wavelength Investigations of Solar Activity*, (Ed.) A. V. Stepanov, E. E. Benevolenskaya, & A. G. Kosovichev, vol. 223 of IAU Symposium, pp. 299–300, Cambridge University Press, Cambridge, UK
- Steiner, O., Stenflo, J. O., 1990, Model Calculations of the Photospheric Layers of Solar Magnetic Fluxtubes, in *Solar Photosphere: Structure, Convection, and Magnetic Fields*, (Ed.) J. O. Stenflo, vol. 138 of IAU Symposium, p. 181
- Steinhilber, F., Beer, J., Fröhlich, C., 2009, Total solar irradiance during the Holocene, *Geophys. Res. Lett.*, 36, L19704
- Stuiver, M., Braziunas, T. F., 1989, Atmospheric C-14 and century-scale solar oscillations, *Nature*, 338, 405–408
- Svalgaard, L., Duvall, Jr., T. L., Scherrer, P. H., 1978, The strength of the sun's polar fields, *Sol. Phys.*, 58, 225–239
- Tapping, K. F., Boteler, D., Charbonneau, P., Crouch, A., Manson, A., Paquette, H., 2007, Solar Magnetic Activity and Total Irradiance Since the Maunder Minimum, *Sol. Phys.*, 246, 309–326
- Thomas, J. H., Weiss, N. O., 2008, *Sunspots and Starspots*, Cambridge University Press, New York
- Title, A. M., Tarbell, T. D., Topka, K. P., 1987, On the relation between magnetic field structures and granulation, *ApJ*, 317, 892–899
- Tlatov, A. G., Vasil'eva, V. V., Pevtsov, A. A., 2010, Distribution of Magnetic Bipoles on the Sun over Three Solar Cycles, *ApJ*, 717, 357–362
- Unruh, Y. C., Solanki, S. K., Fligge, M., 1999, The spectral dependence of facular contrast and solar irradiance variations, *A&A*, 345, 635–642
- Usoskin, I. G., 2008, A History of Solar Activity over Millennia, *Living Rev. Sol. Phys.*, 5, 3
- Usoskin, I. G., Solanki, S. K., Kovaltsov, G. A., 2007, Grand minima and maxima of solar activity: new observational constraints, *A&A*, 471, 301–309
- Usoskin, I. G., Horiuchi, K., Solanki, S., Kovaltsov, G. A., Bard, E., 2009, On the common solar signal in different cosmogenic isotope data sets, *J. Geophys. Res.*, 114, A03112
- Vieira, L. E. A., Solanki, S. K., 2010, Evolution of the solar magnetic flux on time scales of years to millenia, *A&A*, 509, A100

- Vieira, L. E. A., Solanki, S. K., Krivova, N. A., Usoskin, I., 2011, Evolution of the solar irradiance during the Holocene, *A&A*, 531, A6
- Viereck, R. A., Floyd, L. E., Crane, P. C., Woods, T. N., Knapp, B. G., Rottman, G., Weber, M., Puga, L. C., DeLand, M. T., 2004, A composite Mg II index spanning from 1978 to 2003, *Space Weather*, 2, S10005
- Vögler, A., Schüssler, M., 2007, A solar surface dynamo, *A&A*, 465, L43–L46
- Wagner, G., Beer, J., Masarik, J., Muscheler, R., Kubik, P. W., Mende, W., Laj, C., Raisbeck, G. M., Yiou, F., 2001, Presence of the solar de Vries cycle (~205 years) during the last ice age, *Geophys. Res. Lett.*, 28, 303–306
- Wang, Y., Lean, J. L., Sheeley, Jr., N. R., 2005, Modeling the Sun's Magnetic Field and Irradiance since 1713, *ApJ*, 625, 522–538
- Wang, Y., Robbrecht, E., Sheeley, N. R., 2009, On the Weakening of the Polar Magnetic Fields during Solar Cycle 23, *ApJ*, 707, 1372–1386
- Wang, Y.-M., Sheeley, Jr., N. R., 1989, Average properties of bipolar magnetic regions during sunspot cycle 21, *Sol. Phys.*, 124, 81–100
- Wang, Y.-M., Sheeley, Jr., N. R., 1991, Magnetic flux transport and the sun's dipole moment - New twists to the Babcock-Leighton model, *ApJ*, 375, 761–770
- Wang, Y.-M., Lean, J., Sheeley, Jr., N. R., 2002, Role of a Variable Meridional Flow in the Secular Evolution of the Sun's Polar Fields and Open Flux, *ApJ*, 577, L53–L57
- Wenzler, T., Solanki, S. K., Krivova, N. A., Fluri, D. M., 2004, Comparison between KPVT/SPM and SoHO/MDI magnetograms with an application to solar irradiance reconstructions, *A&A*, 427, 1031–1043
- Wenzler, T., Solanki, S. K., Krivova, N. A., 2005, Can surface magnetic fields reproduce solar irradiance variations in cycles 22 and 23?, *A&A*, 432, 1057–1061
- Wenzler, T., Solanki, S. K., Krivova, N. A., Fröhlich, C., 2006, Reconstruction of solar irradiance variations in cycles 21–23 based on surface magnetic fields, *A&A*, 460, 583–595
- Wenzler, T., Solanki, S. K., Krivova, N. A., 2009, Reconstructed and measured total solar irradiance: Is there a secular trend between 1978 and 2003?, *Geophys. Res. Lett.*, 36, L11102
- Willson, R. C., 1997, Total solar irradiance trend during solar cycles 21 and 22., *Science*, 277, 1963–1965
- Willson, R. C., Hudson, H. S., 1991, The sun's luminosity over a complete solar cycle, *Nature*, 351, 42–44
- Wolf, R., 1861, Abstract of his latest Results, *MNRAS*, 21, 77

- Zhang, J., Lin, G., Wang, J., Wang, H., Zirin, H., 1998, The evolution of intranetwork magnetic elements, *A&A*, 338, 322–328
- Zhang, Q., Soon, W. H., Baliunas, S. L., Lockwood, G. W., Skiff, B. A., Radick, R. R., 1994, A method of determining possible brightness variations of the Sun in past centuries from observations of solar-type stars, *ApJ*, 427, L111–L114
- Zhao, J., Kosovichev, A. G., 2004, Torsional Oscillation, Meridional Flows, and Vorticity Inferred in the Upper Convection Zone of the Sun by Time-Distance Helioseismology, *ApJ*, 603, 776–784
- Zhao, X., Hoeksema, J. T., 1995, Predicting the heliospheric magnetic field using the current sheet-source surface model, *Adv. Sp. Res.*, 16, 181
- Zwaan, C., 1985, The emergence of magnetic flux, *Sol. Phys.*, 100, 397–414

# Publications

## Refereed contributions:

- **Dasi-Espuig, M.**, Solanki, S.K., Krivova, N., Cameron, R., 2010, Sunspot group tilt angle and the strength of the solar cycle. *A&A*, 518, A7, 10pp
- Barrena, R., Girardi, M., Boschin, W., **Dasi, M.**, 2009, Internal dynamics of Abell 1240: a galaxy cluster with symmetric double radio relics, *A&A*, 530, 357–37

## Conference and meeting contributions:

- **Dasi-Espuig, M.**, Stahn, T., Solanki, S.K., Gizon, L., Krivova, N., Rotation and variability of F stars in the CoRoT initial run, in: *1st Symposium International*, Paris, France, 2-5 February 2009, (poster)
- **Dasi-Espuig, M.**, Solanki, S.K., Krivova, N., Cameron, R., Penuela, T., Sunspot tilt angles and the strength of the solar cycle, in: *Space Climate Symposium 3*, Saariselka, Finland, 18-22 March 2009, (poster)
- **Dasi-Espuig, M.**, Jiang, J., Krivova, N.A., Solanki, S.K., Modelling total solar irradiance with the use of a flux transport model, in: *Eddy Cross-Disciplinary Symposium on Sun-Climate Research*, Aspen, Co., USA, 22-24 October 2010, (poster)
- **Dasi-Espuig, M.**, Jiang, J., Krivova, N.A., Solanki, S.K., Reconstructions of total solar irradiance since 1878, in: *III Spanish Solar and Heliophysics meeting*, Granada, Spain, 7-9 June 2011, (oral contribution)
- **Dasi-Espuig, M.**, Krivova, A.N., Solanki, S.K., Jiang, J., Models of solar irradiance variations, in: *CAWSES final meeting*, Bonn, Germany, 7-9 September 2011, (oral contribution)



# Acknowledgements

I finally made it!! And so am I, really writing the final lines of this long script, none of which could have been written without the support and help of many others.

I would firstly like to express my gratitude towards the Max Planck Institute for Solar System Research and the International Max Planck Research School on Physical Processes in the Solar System and Beyond. In particular to Dieter Schmitt, for giving me the opportunity to develop the research work presented in this dissertation and for the guidance during the first days when everything was so new. Although it was my wish to do the PhD abroad, I never thought I would find such an international environment. At times it felt like living in different countries all at the same time! And it was this diversity that made my stay here so rich and enjoyable.

My most sincere thanks go to my supervisors, Prof. Dr. Sami K. Solanki and Dr. Natalie A. Krivova, because their efforts also lie between the lines of my thesis. Thanks Sami, for being always reachable in spite of your busy schedule and for all the things I learnt from you. Thanks to Natasha, for your constructive criticism of my work that made me think deeper and try harder. A huge thanks also goes to Dr. Robert Cameron, because you made me feel for the first time that my work was special to the outside world! That gave me motivation and enthusiasm to continue. And of course, thank you for all of the infinite questions you've answered me, helping me understand the secrets behind the solar dynamo. I am also very grateful to Dr. Jie Jiang, for providing the simulations from the surface flux transport model and for always being available to answer my questions. I would also like to thank Dr. Tunde Baranyi from the Heliophysical Observatory in Debrecen, Hungary, for the carefully measured data she provided to continue with part of the work done in this thesis.

Un GRACIAS como el infinito y mas alla va para mi familia. A Mama porque siempre siempre siempre has estado ahi y porque sin tu amor y apoyo yo no seria quien soy y no estaria donde estoy. Y estoy orgullosa! A Blanca porque, aunque ahora ya somos mayores para jugar a hermanas, sigue siendo igual de divertido. Y porque espero que repitamos mas roadtrips en caravana (que esta vez no podemos quedar de primerizas sin linternas ni jabon en un camping), aumentando nuestra banda sonora mas alla de KunFu Fighting, California Girls, Jazon Mraz, Michael Jackson, nuestro amigo Phil Collins y mas que seguro ahora mismo no recuerdo. Gracias a Juani y a Pepita, porque sois mi segunda madre y mi segunda abuela! A Papa, porque es Papa y el lo dice. Porque eres el mejor Papa jugando al golf, corredor de rallies y esquiador (me regalas un ukulele? Jejeje). Ahora en serio, gracias por la seguridad y la independencia que me has dado siempre pues lo valoro muchisimo. Y por supuesto, gracias Ines, Susana y Ma Angeles! Que grandes momentos

hemos compartido escuchando High School Musical, Hannah Montana, el waka waka... Ahora que os estais haciendo mayores que excusa voy a dar cuando alguien me pregunte por que me conzco tan bien todas estas canciones?? Finalmente, gracias abuelo, te dedico la tesis a ti. Porque sin ti, quien sabe si hubiera descubierto la Astrofisica y lo guay que es aprender? Un besito muy grande a todos <3

Por supuesto no pueden faltar amigos que siempre han estado ahí: Marta y Moni (por los tiempos del pack de tres indivisible, las mutadas y los bailes al no-ritmo), Cocs, Marta N. e Ivan (que nos hacemos mayores...). Un beso super grande para Gupichu, por los bailoteos y por ser un gran amigo. A Carlos porque despues de estar Lost supimos encontrar un millon de sentidos mas a nuestra amistad. A Cris, ay como me Riu! Y a Jorge porque molas un monton, entre otras cosas.

A huge thanks goes to my beloved GalileoMobile team members, because we all live under the same sky. Working with you during my PhD time was a million times worth it and gave me inspiration. I love the project, I love to work with all of you and I hope that we will do many more things together.

Furthermore, I want to say Danke to those who have been with me in Germany during this 3 years and a half: Denniiiiiii, through thick and thin, thank you for all the stories, lyrics, and music we shared, because "you make me wanna shout!". Thank you and come again!; Protopapa without h and Jeanito and our crazy nights playing Guitar Hero, were it all started; Lippi, meine Pippin! An appletini to you and our Funky nights!; Kok Leng, without your bombastic bull sh\*\* how could've I written these words? Plus many other things; Maria (the Greek) because your Greek dances are awesome and your Ouzo even more!; Fatima I am so excited we will have a cat all together! Sharing bed with you in Granada was not enough for me; Juanjo, acho, thank you for your sense of humor; Julian I am not so sure whether to thank you for introducing me into Jaegermeister, even if you don't quite remember that night... But thank you for coming back home every Christmas; Anne, what would've been Unicante without your translations? Thank you for sharing it with me for the past 2 years!; David because I know you will be my first fan when I start my ukulele carrier and because you make me smile; Pauline thanks for being so fresh and enthusiastic!; Iulia thank you for being so impartial and for always being ready to do things together; Vali because I hope that by acknowledging you I will get rid of making you any more cakes; Sonja I loved to share the Gleekiness with you plus all the endless fun we've had together that would be impossible to summarise here!; Sabine thank you for your warmth and affection and all the salsa nights; Oh, by the way... I forgot! Raul David (better known as Gordon) and Diego Armando (a.k.a Domenico), I hope that we will smoke pipe together at least one more time, preferably in the West Coast.

# Curriculum Vitae

## Persönliche Daten

Name: Maria Dasi Espuig  
Geburtstag: 21.12.1984  
Geburtsort: Valencia, Spanien

Eltern: M<sup>a</sup> Jose Espuig Verdejo  
Vicente Dasi Martinez de Vallejo

Staatsbürgerschaft: Spanisch

## Schulausbildung

09/1988 – 06/2002: American School of Valencia, Valencia, Spanien

## Studium

09/2003 – 01/2008: Diplom in Physik,  
Universidad de La Laguna,  
Teneriffa, Spanien

## Promotion

02/2008 – 08/2011: Doktorarbeit am Max-Planck-Institut für  
Sonnensystemforschung, Katlenburg-Lindau,  
Deutschland